ABSTRACT

Title of Dissertation: CHARACTERIZATION OF PROPERTY -
STRUCTURE DEPENDENCIES FOR MULTI-
SCALE POLYMER COMPOSITES USING
EXTRUSION PROCESSES

Jason Robert Nixon

Directed by: Associate Professor David I. Bigio
Department of Mechanical Engineering

Multiscale reinforcement, using carbon microfibers and multi-walled carbon nanotubes, of polymer matrix composites manufactured by twin-screw extrusion is investigated for enhanced mechanical and thermal properties with an emphasis on the use of a diverging flow in the die for fluid mechanical fiber manipulation. Using fillers at different length scales (microscale and nanoscale), synergistic combinations have been identified to produce distinct mechanical and thermal behavior. Fiber manipulation has been demonstrated experimentally and computationally, and has been shown to enhance thermal conductivity significantly. Finally, a new physics driven predictive model for thermal conductivity has been developed based on fiber orientation during flow, which is shown to successfully capture composite thermal conductivity.

CHARACTERIZATION OF PROPERTY STRUCTURE DEPENDENCIES FOR MULTI-SCALE POLYMER COMPOSITES USING EXTRUSION PROCESSES

by

Jason Robert Nixon

Dissertation submitted to the Faculty of the Graduate School of the
University of Maryland, College Park in partial fulfillment
of the requirements for the degree of
Doctor of Philosophy
2016

Advisory Committee:
Professor David I. Bigio, Chair/Adviser
Professor Hugh Bruck
Professor Avram Bar-Cohen
Professor Amir Riaz
Professor Isabel Lloyd

Contents

List of Figures

List of Tables

Abbreviations

AlN	**Al**uminum **N**itride
BN	**B**oron **N**itride
ASTM	**A**merican **S**ociety for **T**esting and **M**aterials **D**esign
CMF	**C**arbon **M**icro**F**iber
CNF	**C**arbon **N**ano**F**iber
CNT	**C**arbon **N**ano**T**ube
CoTSE	**Co**-rotating **T**win-**S**crew **E**xtruder
GF	Short **G**lass **F**iber
LDPE	**L**ow **D**ensily **P**oly**e**thylene
HDPE	**H**igh **D**ensily **P**oly**e**thylene
MWNT	**M**ulti **W**alled Carbon **N**ano**T**ube
PBT	**P**oly (**B**utylene **T**erephthalate)
PC	**P**oly (**C**arbonate)
PEEK	**P**oly (**E**ther **E**ther **K**etone)
PS	**P**oly (**S**tyrene)
PMC	**P**olymer **M**atrix **C**omposite
PMMA	**P**oly (**M**ethyl **M**eth**a**crylate)
PES	**P**oly (**E**ther **S**ulfone)
PET	**P**oly (**E**thylene **T**erephthalate)
SiC	**Si**licon **C**arbide **D**ie
SWNT	**S**ingle **W**alled Carbon **N**ano**T**ube
TSE	**T**win **S**crew **E**xtruder
VGCF	**V**apor **G**rown **C**arbon **F**iber
vol.%	Percent by **V**olume
wt.%	Percent by **W**eight

Symbols

A_r	Lewis-Nielsen Einstein coefficient.
A_r	Aspect ratio.
C	Integration constant.
d_f	Fiber diameter.
E	Tensile modulus.
h_{inlet}	Die inlet height.
h_{outlet}	die outlet height.
K	Thermal conductivity.
K_e	Effective thermal conductivity.
K_f	CMF thermal conductivity.
K_m	Polymer matrix thermal conductivity.
K_r	Ratio of CMF to matrix thermal conductivity.
L	Die length.
l_f	Fiber length
N	Screw speed.
Q	Volumetric flow rate.
V_f	Volumetric CMF concentration.
V_{max}	Maximum volumetric CMF concentration.
W	Die width.
$\dot{\alpha}$	Extensional rate.
β	Fiber path angle.
β_0	Critical fiber path angle.
$\dot{\gamma}$	Shear rate.
θ	Die divergence angle.
μ	Kinematic viscosity.
ν	Dynamic viscosity.
ξ	Fiber orientation w.r.t. die plane.
ξ	Mean fiber orientation w.r.t. die plane.
ρ	Density.
σ_u	Ultimate tensile strength.

σ_y	Yeild strength.
τ	Time to fiber out.
ϕ	Fiber orientation w.r.t. fiber path.
ϕ_0	Initial fiber orientation w.r.t. fiber path.

Chapter 1

Introduction

Polymers have become ubiquitous in manufacturing due to their cost, availability, performance, and weight. In comparison to metals and ceramics, polymers are lighter, cheaper, easier to manufacture and machine, but do not match mechanical, thermal, or electrical performance. Depending on composition, polymers can be brittle, ductile, crystalline, semi-crystalline, or amorphous. This range of morphologies lends polymers many uses.

In order to reduce the performance gap, polymer matrix composites (PMCs) are formed by reinforcing polymer matrices are with ceramic and/or metallic fillers whose properties are typically orders of magnitudes greater than that of the polymer matrix. Yet greater property improvements can be gained by using synergistic combinations of fillers at different length scales to reinforce the polymer matrix through alternative mechanisms. Therefore, there is an impetus to explore multiscale PMCs for a range of applications. This body of work is

concerned exclusively with carbon microfibers (CMFs) and multi-walled carbon nanotubes (MWNTs) compounded in a polybutylene terephthalate (PBT) polymer matrix.

Unlike powdered fillers, which have no orientation, the fiber orientation within the matrix is meaningful to PMC properties. Anecdotally, fibers act as load bearing highways, carrying loading down their axis. However, fibers only fractionally enhance performance when the load is applied at an oblique angle to the fiber axis. This enhancement can be minimal to non-existent when the load is applied diametrically, or orthogonally to the fiber axis. Therefore, manipulating the fibers into preferential orientations during the manufacture of PMCs is highly desired based on the end product.

Twin screw extrusion is a continuous compounding and forming manufacturing method that is used to form semi-infinite shapes with respect to the extrusion orientation. Typically in twin screw extrusion, or more generally in any pumping process process, fibers orient to nearly parallel with the extrusion orientation (in the semi-infinite orientation of the shape) over time. For certain applications, such as polymer heat exchangers, we desire fibers to be oriented obliquely or transversely to the extrusion orientation, i.e. in the direction of the thickness, such that fibers are contributing both to the extrusion orientation (longitudinally) and through-thickness (transverse) thermal conductivity. However, by the highway analogy, fibers oriented in an oblique orientation are now not contributing to the longitudinal strength. Therefore, some partial reorientation is best to achieve

the maximum transverse thermal conductivity while minimizing loss in strength and stiffness in the longitudinal orientation.

In this dissertation, the central research focus is to characterize the improved longitudinal tensile and through-thickness thermal properties for PBT/CMF/MWNT composites manufactured using twin screw extrusion and the manipulation of fiber orientation through fluid mechanical means, i.e. by use of a diverging die, during the extrusion process.

1.1   Polymer Composites

Fillers are used to enhance the properties of a neat polymer. The continuous phase, in this case a polymer matrix, is mixed with other materials, known as fillers, that act as a discrete entities within the continuous polymer phase. Fillers are selected to enhance one or more properties of the neat polymer matrix. Fillers are categorically described by their dominant length scale; i.e. nano-scale, micro-scale, etc, their dimensional approximation; zero-dimensional (particulates), one-dimensional (fibers), and two-dimensional (sheets and weaves); and their composition. In this dissertation, a combination of nanoscale and microscale carbon one-dimensional fillers are the exclusive focus.

CMFs are composed of layered graphene cones, cups, and plates. They are typically several micrometers in diameter, but can range from 50 μm to many meters in length. However, these exceedingly high fiber lengths are limited to

other forms of composites manufacturing and are not considered in this dissertation. CMFs possess significantly greater mechanical and thermal properties than that of neat polymers and are ideal for applications demanding increased structural and thermal performances.
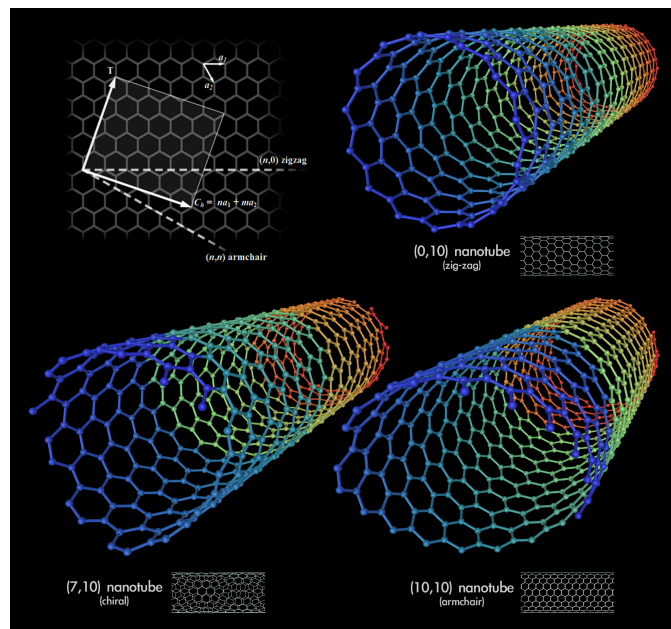
FIGURE 1.1: Single-walled carbon nanotube diagram.

Carbon nanotubes (CNTs), or more specifically single-walled CNTs (SWNTs), have diameters in the range of several to tens of nanometers and are formed from a single layer of graphene rolled into a cylinder and can take several forms depending on the carbon atom organization (see Figure 1.1). SWNT structure has been shown to greatly affect its measurable properties. By forming a cylinder of concentrically organized SWNTs, MWNTs are formed. Both SWNTs and MWNTs possess highly desirable properties including high electrical conductivity, high thermal conductivity, high mechanical strength, and low chemical reactivity. CNTs have been properties have been shown to theoretically and experimentally shown to exceed even CMF properties [1, 2, 3]. However, for

reasons discussed later, SWNTs and MWNTs remain expensive and difficult to utilize in composites.

1.2 Mixing

For this dissertation, PMC manufacturing is performed using twin screw extrusion, a continuous compounding process that mixers fillers into a molten polymer matrix, and then pumps that material through a die into the desired final form. Inside the extruder, specially designed modular screws act to mix the matrix and fillers together. Mixing is described by two mechanisms; dispersive mixing and distributive mixing. The difference between these mechanisms is illustrated in Figure 1.2.
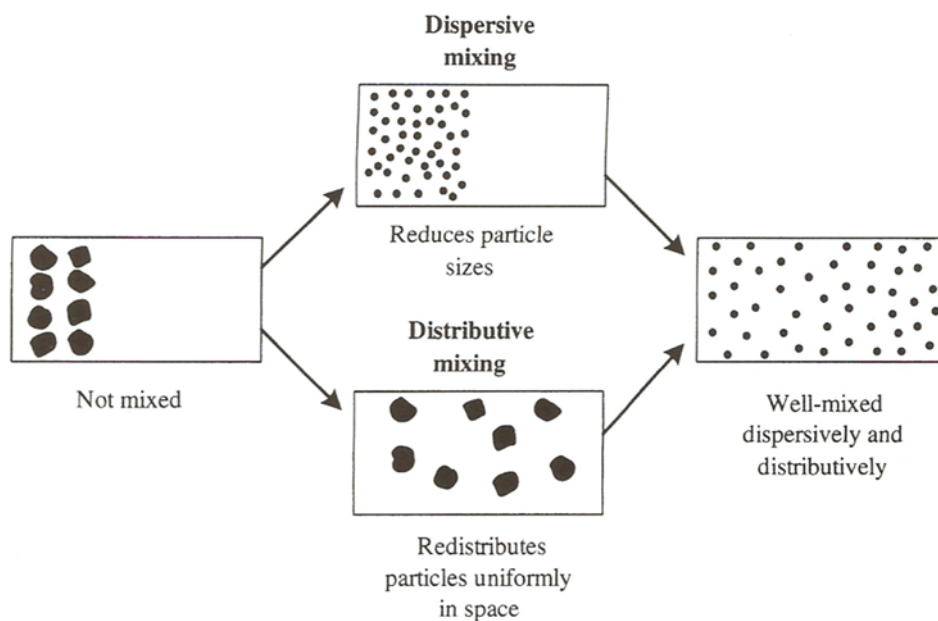
FIGURE 1.2: Distributive and dispersive mixing [4].

Good distributive mixing leads to the ideal arrangement of fillers in space, which in a simplistic sense is nearly equally spaced throughout the composite. Good dispersive mixing leads to a reduction in the size of the filler, which could be a bundles of fibers (e.g. the breakup of the bundle) or the erosion or rupture of an agglomerated particle, much like the crumbling of dried mud. By changing characteristics of the extrusion process like screw design and operating parameters, different degrees of mixing can be achieved. In order to maximize property improvements, both good dispersion and good distribution of the fillers is necessary. However, care must also be taken to not subject the fillers and matrix to excessive mixing, which can fracture fillers, thus leading to reductions in property enhancement.

1.3   Research Objectives

The objectives of this research are as follows:

- Study processing-property-microstructure relationships for multiscale PMCs using CMFs and MWNTs in a PBT matrix prepared by twin screw extrusion across a range of CMF concentrations, CMF lengths, MWNT concentrations, flow rates, and die angles and compare when possible.

  - Characterize tensile modulus, ultimate tensile strength, and thermal conductivity relationships with respect to input parameters using statistical analysis.

– Characterize property trade-offs when utilizing MWNTs.

• Develop procedure for fluid mechanical manipulation of fibers during pumping to induced fiber reorientation using a diverging die.

– Identify property relationships and trade offs for reoriented fibers.

• Develop a predictive model based on existing property prediction models and fluid mechanics to predict thermal conductivity. This model bridges the gap between empirically identified relationships and the physical mechanisms driving this evolution.

1.4   Dissertation Outline

In the following chapters, the methods used to address research objectives in §1.3 and the results obtained are be presented. Chapter 2 presents relevant polymer processing and composites literature. Chapter 3 details the experimental procedures used. Chapter 4 presents a theoretical introduction to fiber reorientation in a diverging flow as well as numerically simulated fiber orientation results in a pumping flow. Chapter 5 presents and discusses microstructural and material properties for laboratory compounded multiscale PMCs. Chapter 6 develops a new model for the prediction of PBT/CMF/MWNT composite properties extruded through a straight or diverging die. Chapter 7 summarizes new scientific contributions and future work related to these studies. Appendix A tabulates property values from Chapter 5.

Chapter 2

Literature Review

The following chapter presents a review of relevant scientific literature for multiscale PMC manufacturing and properties.

2.1 Property Enhancement

Reinforcement of polymer matrices using microscale and nanoscale fillers is the subject of many research studies. The intent of this dissertation is to examine the relationship between flow, microstructure, and resultant property enhancement as a function of processing parameters during compounding and fillers.

2.2 Adhesion and Dispersion

Fillers are compounded into polymer matrices in order to achieve superior properties compared to neat matrix [1, 5, 6, 7]. However, simply 'compounding' is not enough for property enhancement. Specifics of fiber dispersion, alignment, aspect ratio(the ratio of fiber length to diameter), and interfacial stress transfer all play a role in property enhancement [1, 8]. §2.6 addresses the effect of fiber alignment. This section, as well as others, address fiber length.

Property enhancement is dominated by the degree of filler-matrix adhesion and filler dispersion within the matrix under mechanical or thermal load [9, 10]. There must be considerable filler-matrix load transfer for property enhancement. Fillers behave as structural defects when interfacial adhesion is low. These defects produce local stress concentrations and ultimately lead to premature failure under mechanical load. These defects produce local stress concentrations and ultimately lead to premature failure [11, 12, 13]. Similarly, fillers act as thermal barriers rather than conductors due to low interfacial adhesion under thermal load.

Secondarily, local matrix morphology that is a distance from fibers also plays a role in property enhancement. Both Potschke et al. [14] and Ding et al. [15] observed this phenomenon in fiber pull-out experiments. After catastrophic failure, sheaths of matrix, tens of nm thick, extended from the fracture surface at void sites previously occupied by CNFs. This suggests that the local interfacial shear strength was much higher than otherwise expected. Assouline et al.

9

[16], Xie et al. [17], Sandler et al. [18] and Grady et al. [19] observed increased local crystalinity in the interfacial region. Interface contact resistance, produced from a decrease in interfacial thermal conductivity when thermal load is high, inhibits heat flow, even in the presence of good adhesion. Islam and Pramila [20] found that a microscopic interfacial contact resistance region reduced the effective thermal conductivity of the composite by up to 50% when the conductance of the contact resistance zone was one to two orders of magnitude less than the matrix. Nan et al. [21] demonstrated a correlation between interfacial resistance thickness and fiber aspect ratio indicating effective thermal conductivity depreciation. It is also important to keep in mind that local interfacial morphology deviates from bulk morphology in polymer specific ways.

Dispersion also plays a role in property enhancement. Poor dispersion can lead to both fiber re-agglomeration or lack of de-agglomeration. Under mechanical load, fiber agglomerates will fail before their constituents due to a phenomena known as fiber pull-out. Pull-out can occur under three possible conditions: failure of the polymer-fiber interface, excessive shear stress in the matrix immediately adjacent to the fiber, and failure at a fiber-fiber interface. The latter is more likely to occur in agglomerates [22, 23]. Dispersibility has been found to be related to the filler concentration of the composite. At high fiber concentrations there is greater potential for agglomeration by way of entanglement and reduced flow between closely packed fibers. In support, Machando et al. [24] found that tensile properties were enhanced when SWNT concentrations was less than 1 wt.%. At greater than W wt.% SWNT concentration, a decline in

enhancement was observed. Property depreciation is theorized to be a result of decreased dispersibility at higher concentrations.

During melt-compounding, there is a correlation between increasing mixing energy and therefore the dispersive power of the mixer between increasing dispersion and decreasing fiber length. While many speculate that fiber length maximization produces maximal tensile properties, reduced fiber length does not necessarily result in property loss. Andrews et al. [25] showed that increasing mixing energy reduced MWNT length by up to a factor of four ($A_r = 1000 \rightarrow A_r = 250$). Yet those shortened MWNTs produced increased tensile properties compared to longer MWNTs. From the other direction, Wang et al. [26] found that mechanically reducing SWNT length by up to a factor of seven ($A_r = 725 \rightarrow A_r = 100$) not only increased dispersibility, but also improved thermal conductance and electrical percolation onset concentration. Percolation is defined as the threshold at which extremely large fiber networks form, dramatically enhancing conductivity. Frusteri et al. [27] demonstrated similar results for thermal conductance using three CMFs aspect ratios, $A_r = 30, 500, 1000$, in a phase change material (PCM) matrix. These authors hypothesized that decreased length increased dispersibility, and therefore increased which resulted in better load transference. However, at the microscale, there is evidence that excessively shortened fibers result in mechanical property reduction [28]. It is unlikely that critical fiber length, derived using continuum mechanics, is directly applicable to nanoscale fibers.

Separate from process-induced dispersion and adhesion, significant work is currently focusing on the improvement of adhesion and dispersion from the perspective of the fiber [29, 30]. For nanoscale fibers, pre-treatment techniques are often required to promote adhesion and dispersion [31, 32]. Pretreatments, including functionalization and chemical treatment, are often used to improve the wettability, roughness, and quality of the fiber surface [33]. Tiwari and Bijwe [34] and Gong et al. [35] discuss the effectiveness of surface functionalization for adhesion enhancement. Surface functionalization is especially useful for nanoscale carbon-based fibers that are typically chemically inert. However, treatments could be used for any nanoscale filler. These treatments enhance surface wettability, remove weakly bonded surface structures and contaminants, allow for greater fiber-matrix entanglement, and increase fiber porosity, the number of chemically active sites, and the number of potential nucleation sites. Wang et al. [36] also found that mechanically shortened fibers has more chemically active sites, which provided more opportunity for matrix-CNT bonding. Secondary additives can also be included in the mixtures to enhance nanoscale adhesion [37, 38].

For microscale fibers, with characteristic major dimensions three to five orders of magnitude greater than nanoscale fibers, sufficient adhesion and dispersion is easier to achieve by any compounding procedure. Consequently, microscale fibers do not typically require secondary additives or modifications [39, 40].

2.3 Mechanical Properties

A body of authors have reported significant mechanical property enhancement in microscale and nanoscale reinforced PMCs. Cho and Paul [41] increased the concentration of organoclay in a nylon 6-organoclay nanocomposites and found increased ultimate tensile strength and tensile modulus and decreased ductility as concentration increased. Carneiro et al. [42] found that increased vapor grown carbon fibers (VGCF) concentration increased the tensile modulus and yield strength, but decreased the impact strength when VGCF concentration was varied from 0 wt.% to 20 wt.%. Bekyarova et al. [43] studied MWNT reinforcement of an epoxy resin. The multiscale PMC had enhanced out-of-plane mechanical and electrical properties over the neat resin. Sandler et al. [39] observed increased tensile modulus, bending modulus, yield strength, and ultimate tensile strength for CNF concentrations below 15 wt.%. Ductility was maintained until 10 wt.% CNFs in poly(ether ether ketone)(PEEK). Above 10 wt.% CNFs, the PMC became more brittle as the others had reported. Sandler et al. speculated that as the CNF size decreased, CNF dispersion homogeneity increased, leading to more matrix crystallization throughout the matrix.

Andrews et al. [23] found that high dispersion without fiber breakage was key for achieving better properties for CNF and MWNT PMCs. While increasing CNF concentration, at CNF concentrations below 15 vol.%, the tensile modulus increased while the ultimate tensile strength decreased. At higher CNF concentrations, both the tensile modulus and ultimate tensile strength increase.

Overall, the removal of defects increased properties, and surface treatment improved interfacial bonding. Poor adhesion led to fiber pull-out, which reduced the effective mechanical properties.

While many reported improved ultimate tensile strength and reduced ductility, there have also been cases where little improvement was observed. Lozano and Barrera [44] found that with the addition of CNFs, ultimate tensile strength did not improve significantly. However, increased brittleness was shown, which could be attributed to the inability of the matrix to further crystallize when subject to deformation because of the molecular restrictions related to dispersion. Lee et al. [45] claimed that a reduction of properties due to nanoscale fillers indicated poor adhesion and dispersion. They used electrophoretic deposition to deposit nanoscale reinforcements and found that good dispersion homogeneity was achieved which lead to improved properties. Lastly, there have been reports where fillers improved properties until a certain filler concentration, and then begin to hinder the composite. Broza et al. [46] found that the tensile modulus, ultimate tensile strength, and strain to failure increased when increasing CNT concentration in a PBT matrix from 0.01 wt.% to 0.1 wt.%. However, when CNT concentration was increased from 0.1 wt.% to 0.2 wt.%, the ultimate tensile strength strength and the strain to failure of the nanocomposites decreased slightly . Zeng et al. [47] added CNFs to poly(methyl methacrylate) (PMMA) and found that there was an optimum concentration of CNFs between 5 wt.% and 10 wt.% since beyond a 10 wt.% CNF concentration, the modulus began to decline. Zeng et al. recognized, however, that this optimum concentration would

be a function is a function of fiber dimension and the degree of dispersion homogeneity.

Yesil et al. [48] studied CMF reinforced high-density polyethylene (HDPE), polyethylene terephthalate (PET), and MWNT composites. They found that after an initial increase in tensile strength, the addition of microfibers and MWNTs decreased the performance since there was a lack of compatibility with the polymer phase beyond 30 wt.% concentration of PET.

In summary, the mechanical properties are altered with the addition of microscale and nanoscale fibers to a polymer matrix. Most groups have reported improved properties, but recognize that there are likely a minimum or maximum concentration that yield the greatest property enhancements. Furthermore, there are intrinsic processing limitations that limit performance capability of compounded PMCs. Above these limits, viscous forces and fiber interactions act to erode and fracture fibers, reducing their effectiveness for PMC reinforcement.

2.4   Thermal Properties

Heat conduction is defined as the transfer of energy from more energetic to less energetic particles through particle interactions [49]. Energy is related to the translational motion, internal rotation, and vibrational modes of the molecules. In solids, the transfer of energy is dominated by translation motion and lattice vibrations [49]. PMC effective thermal conductivity is related to the number and quality of matrix-filler interfaces, the quality of fibers, and the conductivity of

the matrix, for the the global exchange energy. Secondarily, the onset of thermal percolation would produce yet better effective thermal conductivity. In order to maximize thermal conductivity, fibers should ideal have a high aspect ratios and be well dispersed [50, 51]. Again, by the highway analogy, a single continuous highway is more effective than many short ones, presuming that the highway is going in the direction you wish to travel.

Thermal property enhancement in polymer composites with CMFs and CNTs has been predicted to be very high due to the thermal conductivity of the fillers [52, 53]. For example, Hone et al. [51] examined epoxy-SWNT and epoxy-VGCF thermal conductivity enhancement. They found an enhancement of 120% at 1 wt.% SWNT and, 40% at 1 wt.% VGCF, and 110% at 2 wt.% VGCF. A broad review of polymer and filler thermal conductivity values can be found in [54]. Broadly, the thermal conductivity of many neat polymers have been reported to be in the range of 0.1 W/mK to 1.0 W/mK.

Many authors have reported on the thermal conductivity of isolated CMFs. PAN-based CMFs have demonstrated thermal conductivity between 8 W/mK and 70 W/mK. Pitch-based CMFs have demonstrated thermal conductivity between 530 W/mK and 1100 W/mK. Metal fibers have been reported to be in the range of 200 W/mK to 500 W/mK.

The measurement of the isolated thermal conductivity of a CNT has proven to be a research domain of great interest. Using molecular dynamics simulations, Berber et al. [52] predicted longitudinal thermal conductivity to be 6600 W/mK at 25°C for a pristine (defect free) CNT. Experimental results by Hone et al.

[55], Kim et al. [56], Yu et al. [57] established a wider range of 2800 W/mK to 6600 W/mK at 25°C. While this value is unusually high, consideration of the carbon-carbon bond structure and nearly defect free atomic structure, the value is not surprising for an isolated CNTs [52]. Along the fiber axis, heat conduction is due to a phenomenon known as ballistic phonon transport. However, this mechanisms is only available along the fiber axis, and it is therefore unsurprisingly that the transverse heat flow of CNTs are reported as significantly lower. Sinha et al. [58] experimentally demonstrated an effective conductivity of 1.5 W/mK, three orders of magnitude less than axial conductivity.

From a structural perspective, Agarwal et al. [59] found that the effective conductivity of highly aligned CNFs was greater than that of randomly aligned CNFs. Hone et al. [51, 55], found that uniaxially aligned nanofiber structures possessed a thermal conductivity of 250 W/mK, planar randomly aligned nanofiber structures possessed thermal conductivity in the range of 30 W/mK to 70 W/mK, and three-dimensional random nanofiber structures demonstrated even lower thermal conductance. [60] showed similar results using molecular dynamics simulations.

Wang et al. [26] explored the effect of CNT length on thermal conductivity and found that mechanical shortening combined with surface treatment of the CNTs enhanced thermal conductivity. Wang et al. hypothesized that shorter CNTs had a richer surface chemistry and possessed improved dispersability, which is supported by the work of Wang et al. [36]. Zimmer et al. [61] also explored

the thermal property enhancement using long MWNTs and short MWNTs. Results showed that, contrary to intuition but in support of previously discussed works, the thermal conductivity long MWNTs was not improved over that of short MWNTs, and that the long MWNTs acted more like insulators due to phonon transport interference.

Frusteri et al. [27] examined CMFs of different lengths and loading's mixed with inorganic phase change materials. Results showed thermal conductivity enhancement increased linearly with loading, and that CMF length effected thermal conductivity. Shorter CMFs produced higher thermal conductivity. The authors speculated that this was because of the degree of homogeneity achieved in the samples, where CMFs (6 μm diameter) of 200 μm length were better dispersed than the 3 mm and 6 mm mm CMFs. They also found that at a 7 wt.% loading, the thermal conductivity quadrupled. Similar results were for shortened fibers have already been discussed in §2.2.

Because effectiveness thermal conductivity has been found to be a function of dispersion and adhesion, the reader is referenced back to §2.2 for a discussion of interfacial thermal resistance, surface functionalization, etc.

Zhou et al. [62] examined thermal conductivity enhancement using surface treatment of micro-SiC/DGEBA/EMI-2,4 and nano-SiC/DGEBA/EMI-2,4. Results showed that surface treatment of the nano-SiC increased thermal conductivity.

Interestingly, Sun et al. [63] and Shenogin et al. [64] identified a competitive relationship when functionalizing CNTs. While functionalization increases the

potential for adhesion, functionalization also damages the CNT structure. This damage increases phonon transport interference, thus reducing the effective thermal conductivity of the CNT.

While many have reported increased effective thermal conductivity, others have found little improvement. Gojny et al. [65] concluded that low interfacial area and weak interfacial adhesion promote thermal conductivity, which is in opposition to the requirements of improved mechanical properties. Gojny et al. theorized that poor adhesion acts to shield the fiber from the matrix, reducing phonon transport interference along the fiber length. Therefore, CNTs, which posses large interfacial areas and defect rich carbon structures, are not suitable for thermal conductivity enhancement. However, it is possible that that interfacial contact resistance, which was previously discussed in §2.2, was a dominant mechanism rather than phonon transport resistance.

2.5 Processing Conditions

Twin-screw extrusion was used to compounding PMCs in this dissertations. Twin-screw extrusion highly versatile method of melt-mixing capable of achieving a range of mixing qualities by changing configuration and operating parameters, which in turn effect the amount of shear stress and strain imparted to the material during compounding. However, the design of screws and choice of operating parameters remains somewhat of an art form and consequently the subject of many experimental studies.

The shear stress seen by the material in the extruder is strongly dependent on screw speed. Chen et al. [66] found that at higher shear rates, electrical conductivity at 1.5 wt.% CNT was comparable to conductivity at 2.5 wt.% CNT which had been processed at a lower shear rate. However, while the higher shear rates led to better dispersion and electrical conductivity, it also reduces the alignment of the CNTs, reducing other properties. Villmow et al. [67] found that in a PLA matrix, controlling for flow rate, a screw speed of 500 rpm yielded better MWNTs dispersion when compared to 200 rpm and 100 rpm.

Vera-Agullo et al. [68] performed an extensive study on the dispersion of CNTs and found that more aggressive screw designs increased dispersion, but also increased CNT fracture. While less aggressive screw designs were found to sufficiently disperse CNT agglomerates to form electrically conductive networks, mechanical enhancement was only found using the most aggressive screw designs. This relationship between dispersion and mixing intensity is fundamentally demonstrated stated by Scurati et al. [69]s, who proposed a model of agglomerate erosion and rupture based on the power input of the mixing process.

Gao et al. [70, 71] found that the degree of mixing is dependent on screw speed, volumetric flow rate, specific throughput (volumetric flow rate divided by screw speed). Pappas [72] and Fukuda [73] further explored this concept and characterized the stress seen by the ingredients in an extruder. Pappas and Fukuda found that specific throughput and screw speed effected the imparted stress on the filler, where higher operating inputs produced imparted higher stress on the

filler. By varying processing conditions, the final structure and properties of the PMC were altered significantly.

Acierno et al. [74] has shown that voids and gaseous inclusions have been shown to reduce reduce property performance . At higher CNT loadings, the extent of mechanical property improvement is limited by the high apparent viscosity of the melt, which acts to limit the removal of gaseous inclusions, and the resulting void defects [11]. Kuriger et al. [75] found that the number of voids increased with the filler concentration, which is resultant from the extremely high apparent viscosity near the filler in comparison to the bulk. Kota [3] found that by pulling a vacuum on the melt during compounding, the porosity of the polymer was significantly reduced and physical and electrical properties were greatly increased.

2.6   Microstructure

As stated in §2.2, fiber alignment within the matrix produces anisotropic properties [29, 76]. We are primarily concerned with the average fiber orientation of many fibers with respect to the applied load. Several bulk structure are commonly found in literature: unidirectionally aligned, in-plane randomly aligned, and fully three-dimensional randomly aligned. A two-dimensional illustration of these states is shown in Figure 2.1. Depending on the desired application, different structure and structure orientation may be preferred.
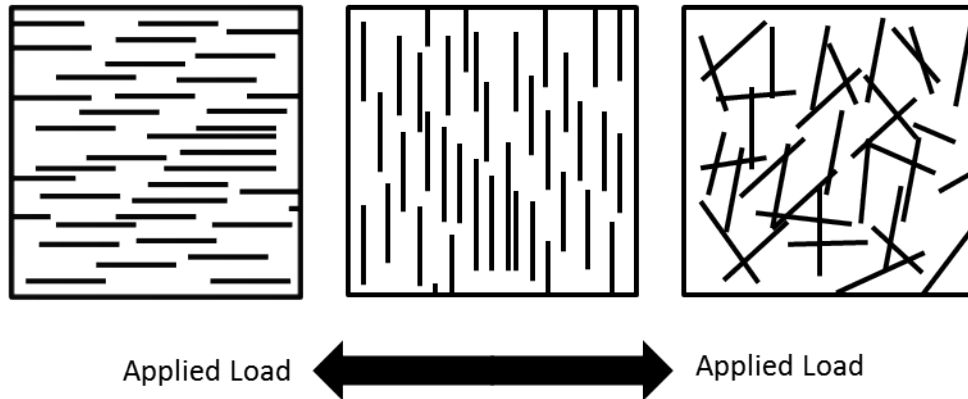
FIGURE 2.1: Discontinuous fiber reinforcement, left to right: unidirectionally aligned under longitudinal loading, unidirectionally aligned under transversely loading, planar-randomly aligned.

Agarwal et al. [59] found that CMFs uniaxially aligned parallel to the applied load greatly enhanced thermal conductivity. Agarwal et al. also found that in-plane enhancement was up to 600% greater than uniaxially out-of-plane or random structures, and that out-of-plane enhancement was little better than random. Thostenson and Chou [77] found that the extrusion process and post-extrusion drawing produced a uniaxial nanostructure in PS/CNT. These samples demonstrated increased strength and increased stiffness when compared to a randomly aligned PS/CNT samples, and demonstrated better load transfer capacity from the PS to the CNTs. Kuriger et al. [75] found that the fiber alignment improves with a longer time in the extruder, and that this had a significant effect on properties. By examining thermal conductivity, they found that highly aligned fiber structures improved thermal conductivity most in the longitudinal direction. Du et al. [78] performed an extensive study on the alignment and dispersion of PMMA-SWNT and related it to mechanical, thermal, and electrical properties. While all the formulations/structures showed improvement over PMMA, the electrical conductivity was greatly influenced by SWNT alignment, where

the aligned samples were 5 orders of magnitude lower in electrical conductivity when compared to unaligned samples. This was a result of low SWNT contact networking, which is necessary for electrical conductivity.

A number of authors have reported on process induced fiber orientation. Kuriger et al. [75] and Rangari et al. [79] reported success in aligning fibers during extrusion. Jin et al. [80] and Haggenmueller et al. [81] reported success in producing aligned structures using drawing. Highly aliened SWNT structures have also been produced using magnetic fields [82, 83, 84]. In all cases, authors reported significantly greater properties in-line with fibers then transversely.

While authors have reported on increased alignment uniformity using extrusion, not all authors have reported such occurrence. Zeng et al. [47] and Potschke et al. [85] found that nanoscale fibers were not necessarily aligned after extrusion. Sandler et al. [39] found that the alignment of CNFs further decreased during injection molding.

Several groups have explored methods for creating random or out-of-plane aligned filler structures. Vincent and Agassant [86] explored the use of diverging flow to produce out-of-plane aligned fiber alignment.

Halpin and Kardos [87] showed that tensile strength and stiffness of three-dimensional randomly oriented fibers could be approximated as isotropic.

The structure of fillers within the embedding polymer matrix greatly effects PMC property anisotropy. Highly aligned fibers produce significant enhancement in the orientation of the fillers, but little to no enhancement in other orientations. Alternatively, randomly aligned filler structures tend to produce nearly isotropic property enhancement, at the cost of reduced enhancement overall. Manipulation of the structure at a microscale and nanoscale can produce enhancements in certain loading directions and reductions in others depending on the preferred structural orientation.

2.7 Multi-Filler Composites

A number of studies have been conducted on PMCs compounded with two or more different filler materials (ceramics, metals, etc.), length scales (microscale and nanoscale), and/or dimensionalities (tubes, sheets, spheres, agglomerated bodies, etc.). The goal of these studies was to identify combinations of fillers that resulted synergistic PMC enhancement. PMCs containing multiple fillers are broadly referred to as hybrid PMCs, while PMCs containing fillers of different major length scales are referred to as multiscale PMCs.

Agarwal et al. [59] compounded CNFs and CMFs into PC and found that higher thermal conductivity in PC/CMF/CNF samples than PC/CMF samples. Agarwal et al. hypothesized that CNFs enhanced the interfacial adhesion between the PC

and CMF, leading to enhanced heat conduction through the fiber-matrix interface. Lederer [88] explored filler-processing-property relationships of PBT/CMF/MWNT PMCs compounded by twin-screw extrusion. Lederer [88] found that certain combinations of CMF and MWNT lead to enhancements in properties over PBT/CMF alone for both tensile and thermal properties. For these PMCs, CNT dispersion could become a significant issue, but was not directly measured. Property improvements were not in general always synergistic and certain ratios of CMFs and CNFs could result in property depreciation. Nie et al. [89] investigated interfacial shear strength, longitudinal elastic modulus, and transverse elastic modulus of epoxy/CMF/CNT PMCs a multiscale simulation. It was found that elastic modulus of the CNT/epoxy was significantly enhanced over neat epoxy, and that increasing CNT-epoxy adhesion also increased the effective matrix properties. CMF properties changed little in the presence of CNTs. This study rightly demonstrated that CNT adhesion is critical for property enhancement.

As a note, the direct compounding of multiple fillers is not the only multiscale PMC production method currently under considered. Another prominent technique is the synthesis of nanoscale features onto microscale fibers. By synthesizing CNTs using CVD onto the surface of CMFs, Thostenson et al. [90] found increased interfacial shear strength when compared to neat CMFs. This was hypothesized to result from the enhanced surface area available for matrix adhesion. Bekyarova et al. [43] studied SWNT and MWNT synthesis on CMFs by electrophoretic deposition and found that the presence of MWNTs enhanced

electrical properties, did not effect tensile properties, and improved interfacial shear stress when compared to neat CMFs. Similar work was also reported by Lee et al. [91] and Qian et al. [92].

Multidimensional and multimaterial PMCs have also been examined in the literature. Xu et al. [93] examined the thermal conductivity of AlN spheres, AlN whiskers, and SiC whiskers in epoxy, and found that the inclusion of spherical and fibrous fillers of the same material produced the highest increase in thermal conductivity. Furthermore, the inclusion of SiC whiskers could be used instead of AlN whiskers to augment mechanical properties while the AlN particulates enhanced the thermal properties

Lee et al. [94] studied the inclusion of a combination of Wollastonite and SiC fibers, and boron nitride (BN) particles in HDPE. They found that at low concentrations, the combination of fiber and spherical fillers increased thermal conductivity, but at higher filler concentrations the role of the fibrous material was minimal. Research into the synergy between CNTs and graphene has also been conducted by Zhang et al. [95], Zheng et al. [96], Li et al. [97]. However, CNT/-graphene PMCs posed additional issues related to the dispersion and adhesion to both the CNT and graphene fillers.

Chapter 3

Methods and Procedures

This chapter describes the equipment and procedures used in the experiments conducted in this dissertation.

3.1 Materials

Three types of ingredient were utilized in this investigation: (1) polymer matrix, (2) microscale filler, (3) nanoscale filler.

3.1.1 Polymer Matrix

Polybutylene terephthalate (PBT) was used as the polymer matrix throughout all experiments presented in this dissertation. The PBT was supplied by Poly-One Corporation and was sourced from Chang Chun Plastics Co. (Grade 1200 211D). Poly (butylene terephthalate) (PBT) is a semi-crystalline thermoplastic

which offers a good combination of thermal stability and mechanical properties when compared to other polymers. [98] PBT is often used as an insulator for electrical components in various industries and it is durable under harsh environments, making it ideal for some applications. For this application, its rapid crystallization made post-extrusion collection easier. The molecular weight of the PBT is 28000. Its melting temperature is approximately 225°C.

3.1.2   Microscale Fillers

Two lengths of CMF were used in this body of work: 6 mm (aspect ratio 800) and 100 μm (aspect ratio 16). Both lengths of CMFs has a diameter of 7 μm and were provided by Toho Tenax America, Inc. (Tenax-A HT C496 6mm respectively and Tenax-A HT M100 100mu). 6 mm CMFs were mechanically chopped and supplied as bundles. 100 μm CMFs were ball milled and supplied as a loose powder. Both CMFs were recommended for use with PBT because of surface adhesion compatibility. Although it would be ideal to use a wider range of CMF lengths in the range of 200 μm to 500 μm, these CMFs were not commercially available due to processability issues.

3.1.3   Nanoscale Fillers

PolyOne Corporation supplied a pre-compounded mixture containing 15 wt.% MWNT and 85 wt.% PBT. Receiving the PBT/MWNT batch ensured consistent

and proper MWNT adhesion, dispersion, and distribution. Supplied MWNTs were approximately 7 μm in length and 11 nm in diameter (aspect ratio 600).

3.1.4 Summary of Matrix and Filler Properties

Table 3.1 summarizes manufacturer specified material properties of the PBT and fillers.

TABLE 3.1: Manufacturer specified material properties.

Property	PBT	CMF	CMF	MWNT
Density	1.31 g/cm^3	1.82 g/cm^3	1.82 g/cm^3	1.50 g/cm^3
Length	-	100 μm	6 mm	7 μm
Diameter	-	7 μm	7 μm	11 nm
Ten. Mod.	2.7 GPa	226 GPa	226 GPa	-
Ult. Ten. Str.	42 MPa	4.41 GPa	4.41 GPa	-

3.2 Twin Screw Extrusion

PMC samples were compounded using a co-rotating fully intermeshing twin-screw extruder (CoTSE). Extrusion is a continuous melt-mixing process that is commonly used in polymer processing, pharmaceutical, and food industries, among many others. Continuous melt mixing produces consistent and well-mixed product, although the choice of processing conditions and extruder design remain somewhat of an art form.

The extruder used was a Coperion ZDSK 28 mm tri-lobal CoTSE, located in the Advanced Manufacturing Laboratory at the University of Maryland, shown in Figure 3.1. Each screw has an outer diameter of 28 mm and is 900 mm in long from feed port to die. The resulting non-dimensional length to diameter ratio is 32.
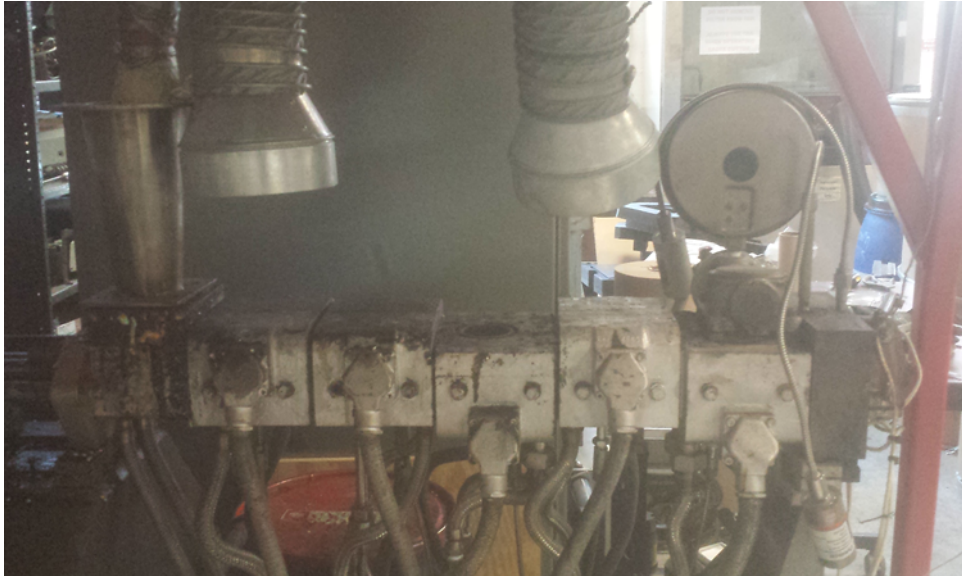
FIGURE 3.1: Twin screw extruder setup in the Advanced Manufacturing Lab.

The extruder is comprised of eight zones: the intake block, five electrically heated barrels, the connection block, and an electrically heated die zone. The intake port receives material pellets (or powder) from above-mounted feeders. Each barrel is individually electrically heat and can be water cooled if necessary. The majority of the screws are housed within the barrels. Fillers are fed into the extruder at the mixing port, located in the top of barrel three. A Welch R1402 vacuum pumped is attached at the vacuum port located at barrel five. Material was processed at a vacuum of 500 mmHG in order to remove volatiles and gaseous inclusions. The connection block and die block proceed barrel five.

The connection block hosts ports for instrumentation such as a optical probes or pressure transducers. For this dissertation, no additional instrumentation was used and empty probe housings were secured into instrumentation ports to prevent material from escaping.

3.2.1 Die Design

The die, mounted on the die block, forms the extrudate into the desired final shape during pumping. All straight and divergent dies were designed with a common die width W of 25.4 mm (1.0 in) and an inlet height h_{inlet} of 1.0 mm. Different divergence angles θ were created by varying the die length L from 25.4 mm to 50.8 mm (1 in to 2 in) and the outlet height h_{outlet} from 1.0 mm to 5.0 mm. Table 3.2 provides a summary of the die geometries used in this body of work.

TABLE 3.2: Die dimension list for all non-diverging and extruder diverging dies.

Letter	L	h_{inlet}	h_{outlet}	θ
A	25.4 mm	1.0 mm	1.0 mm	-
B	50.8 mm	1.0 mm	3.5 mm	1.41°
D	50.8 mm	1.0 mm	5.0 mm	2.26°
E	25.4 mm	1.0 mm	3.5 mm	2.82°
F	25.4 mm	1.0 mm	5.0 mm	4.52°

3.2.1.1 Die Residence Time

By control volume analysis, it is possible to calculate the mean residence time of polymer within a die using throughput, polymer properties, and die geometry.
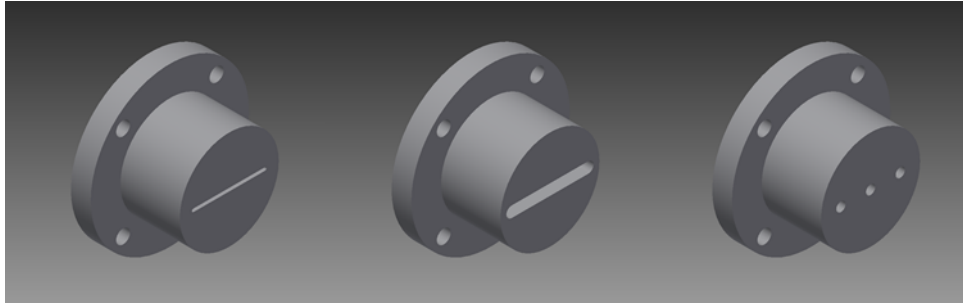
FIGURE 3.2: Extruder die front face (from left to right): straight compounding die (A), divergent compounding die (E), strand die.
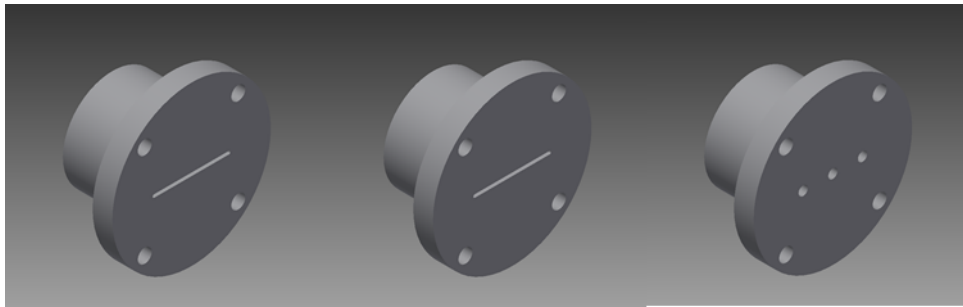
FIGURE 3.3: Extruder die rear face (from left to right): straight compounding die (A), divergent compounding die (E), strand die.

The mean velocity of a particle in the die is defined as Equation 3.1.

$$v_{die} = \frac{W \cdot (h_{inlet} + h_{outlet}) \cdot \rho}{2Q} \tag{3.1}$$

Alternatively, it is possible to define the mean die residence time, i.e. the amount of time the die volume of material spends in the die, as Equation 3.2.

$$t_{die} = v_{die} \cdot L \tag{3.2}$$

3.2.2 Screw Design

Inside the CoTSE, two intermeshing screws synchronously rotate to mix materials. These screws are composed of modular screw elements that are affixed to a central keyed shaft. These elements can be of the conveying and kneading variety. Forward conveying elements pump material down-channel. A special screw design, known as a pumping screw, is composed entirely of forward conveying elements. Conversely, reverse conveying elements pump material up-channel. For these elements, the upstream melt pressure must overcome the back-pressure generated by the reverse conveying element in order to pump material forward. Reverse conveying elements are frequently used as end caps to mixing sections in order keep material inside the mixing section for a longer time. Kneading blocks, which are composed of a series of offset paddles, produce mixing. Mixing section configuration, paddle thickness (wide, medium, and narrow), and paddle angle offset produce different amounts of mixing. Note that although not used in this research, reverse kneading elements can also be used. A variety of other types of screw elements are also available for specialist applications. Mixing section design is frequently varied in order to find the ideal arrangement to maximize mixing while minimizing property depreciation due to high stress. Screw element arrangement is critical for extrusion because of the potential to dramatically alter properties.

The screw geometry used in this dissertation is shown in Figure 3.4.

Color	Element Direction	Element Type	Axial Length (cm)	Axial Pitch (cm)
Orange	Forward	Conveying	1.0	1.0
Brown	Forward	Conveying	4.5	1.5
Green	Forward	Conveying	3.0	1.0
Yellow	Forward	Kneading Block	3.0	0.6
Light Blue	Reverse	Kneading Block	1.5	0.3
Grey	Forward	Kneading Block	1.5	0.3
Blue	Forward	Kneading Block	4.5	0.9
Red	Reverse	Conveying	3.0	1.0
White	Forward	Screw Tips	2.5	--
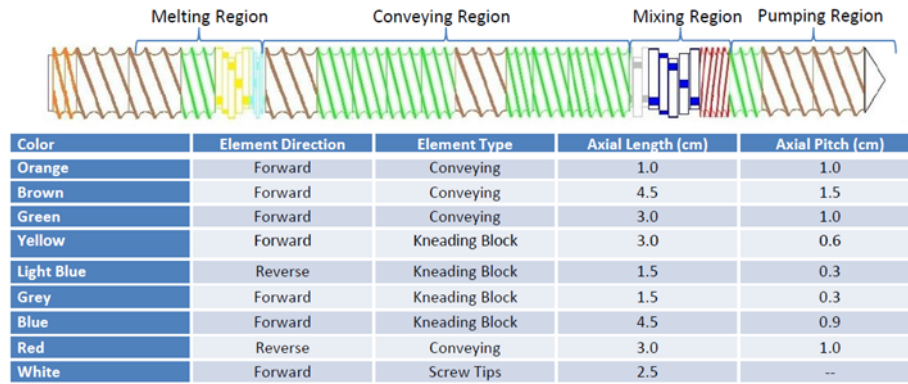
FIGURE 3.4: Modular screw design used in this dissertation.

The screw shown in Figure 3.4 is divided into four sections, in order from first to last: melting, conveying, mixing, and pumping. Material enter the melt section through the intake block, is melted, and then conveyed downstream by the conveying section where fillers are added through the feed port in barrel three. The mixing section then kneads the material and fillers, dispersing fillers in the matrix. After the mixing section, devolatilization in the pumping section removes any gaseous contaminants in the material. The compounded melt is then pumped to the screw tips, which are housed in the die zone. This pumping action then forces the melt through the die.

3.2.3 Extruder Control

The ZDSK-$28mm$ extruder is controlled by a FACTS MI 101 control system. The control system has both manual and digital controls. This control unit was used to set and monitor barrel and die temperatures, set screw speed, and monitor motor amperage. To prevent damage to the extruder, drive amperage was

not allowed to exceed 15 amps, although the control system imposed a 20 amp
hard limit before emergency stop. Rheological properties, filler concentration,
processing conditions, and screw geometry all affect the drive load. If an excess
of material was fed into either feed port, if the material was highly elastic, or if
the screw geometry was too aggressive (quantity and placement of the kneading
elements) the drive could not achieve the necessary torque required to turn the
screws.

The standard temperature profile and screw speed set points for PBT are listed
in Table 3.3. Water cooling was not necessary for compounding PBT.

TABLE 3.3: Extruder set points for PBT.

Parameter	Set Point
Flow rate	1.4 - 2.3 kg/hr
Screw Speed	200 rpm
Barrel 1	229°C
Barrel 2	246°C
Barrel 3	241°C
Barrel 4	249°C
Barrel 5	249°C
Die Zone	235°C

3.2.4 Material Feeders

To regulate material input to the extruder, two laboratory scale feeders were used, one for material pellets and one for microfiber. Both feeders were secured to a platform above the extruder extruder for access to the top-facing feed ports.

A K-Tron loss-in-weight twin-screw feeder was used to feed material pellets into the extruder through the intake block. This feeder was connected to the extruder feed port via a flexible tube and steel funnel. This feeder has a maximum limit of 22.7 kg/hr.

Filler were fed into the feed port by a K-Tron Micro Feeder MT12 loss-in-weight twin-screw feeder. Although this feeder is typically used for powders, it can also be used for CMF bundles. Extensive validation was completed to verify the feeder performance for fibers. This feeder has a maximum limit of 0.45 kg/hr.

3.2.5 Material Collection

Extrudate was collected in strips for property testing using the dies listed Table 3.2 (Pg. 31) or in strands for pelletization.

3.2.5.1 Die A

Straight die samples were collected using a chilled roller system, which put the strip under tension, rapidly cooled the sample, reduced surface non-uniformity, and eased collection. The speed of the rollers could be set using an analog motor

controller, and was adjusted to match the rate of pumping. By setting the roller speed greater than the pumping rate, the strip could be thinned.

3.2.5.2   Die B-F

Diverging die samples were collected using a metal conveyor belt in order minimize drawing prior to cooling, which could lead microstructural changes due to internal flows generated during drawing. The speed of the conveyor was set using an analog motor controller, and the speed was set to match the pumping rate from the die.

3.2.6   Pelletization

Batched pellets were formed using the strand die and a Kilion Extruders Inc. plastics pelletizer. During initial operation, strands were collected by hand and drawn through a water bath to ensure cooling prior to pelletization and fed into the pelletizer. Once fed, strands were automatically drawn into the pelletizer by a friction pinch roller system. A spinning block then cut the strands down into pellets of desired size which were ejected from the rear of the machine. The draw rate of the pinch roller was set to match the extrusion rate. The collected pellets were then dessicated as per neat PBT, and then used in the extruder to achieve loadings greater than 15 wt.%.

3.3 Property Testing

3.3.1 Tensile Testing

Tensile tests were conducted using a Tinius Olsen H25K-T bench top universal testing machine with a 5000 lb load cell, located in the Modern Engineering Materials Instructional Laboratory at the University of Maryland. An extension rate of 2 mm/min was used. Samples were secured into this testing device by two self tightening clamps which acted to pull the specimen apart. This platform recorded the applied load and displacement in time and exported this data as a tabulated data list. The native software also calculated the relevant tensile material properties automatically, although it was necessary in some cases to re-analyze the data to remove data artifacts like clamp slip. Using load/displacement data, stress/strain data could be extracted, which in turn allowed for tensile modulus, ultimate strength, and yield strength can be determined.

Tensile specimens manufactured and tested according to the ASTM D638-12 standard [99]. This standard specifies testing conditions and geometry in order to produce reliable and repeated measures for tensile properties. The geometry for a tensile specimen is shown in Figure 3.5.

3.3.2 Thermal Conductivity Testing

A C-Therm TC-30 modified transient plane source thermal measurement system was used to measure effective thermal conductivity. The TC-30 measures
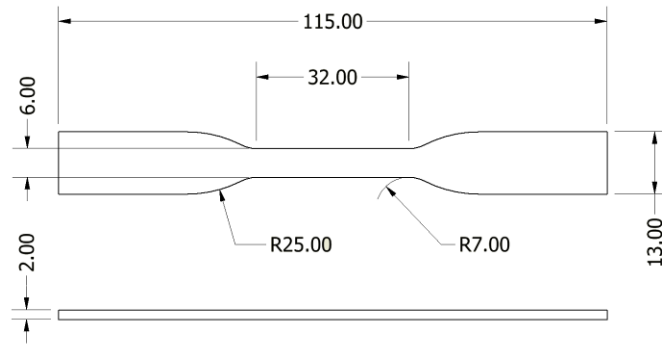
FIGURE 3.5: ASTM D638-10 type-IV tensile test specimen geometry.

thermal conductivity by applying a known current to the sensor's spiral heating element, which is is guarded to support one-dimensional heat transfer into the sample, providing a small amount of heat. The applied current results in a rise in temperature at the interface between the sensor and the sample, which induces a change in the voltage drop of the sensor element. The rate of increase in the sensor voltage is used to determine the thermal conductivity of the sample.

FIGURE 3.6: C-Therm TC-30 thermal conductivity measurement system.

Thermal conductivity is inversely proportional to the rate of increase in the temperature at the point of contact between the sensor and the sample. The voltage is used as a proxy for temperature. Voltage will rise more steeply when lower thermal conductivity materials (e.g. foam) are tested. Conversely, the voltage slope will be flatter for higher thermal conductivity materials (e.g. metal).

Thermal conductivity is calculated from the initial voltage V_0, rate of change m of the measured voltage in the testing window, and calibration coefficients C_2, C_3, and C_4 Equation 3.3. If the slope remains constant in the testing window, a single blotter test (§3.3.2.2) test was used. If the voltage was demonstrated non-linearity, a dual blotter test (§3.3.2.3, Pg. 42) procedure was used.

$$k = \frac{C_2}{\frac{m}{V_0} - C_4} + C_3 \qquad (3.3)$$

3.3.2.1 Calibration

Full calibration was performed at the beginning of testing. Typically five calibration standards, selected to span the expected conductivity range, were used to generate the regression equation coefficients C_2, C_3, and C_4. The standards are listed below in Table 3.4.

TABLE 3.4: TC-30 calibration standard thermal conductivity at $20°C$ in $W/m - K$.

Material	LAF20	Lexan	HDPE	Pyrex	Macor
Conductivity	0.085	0.254	0.577	1.150	1.600

Once full calibration is completed, an HDPE calibration standard was tested every ten samples to track calibration drift over time. Using this data, it was possible to identify bad tests or to correct for small drifts in calibration.

3.3.2.2 Single Blotter Testing
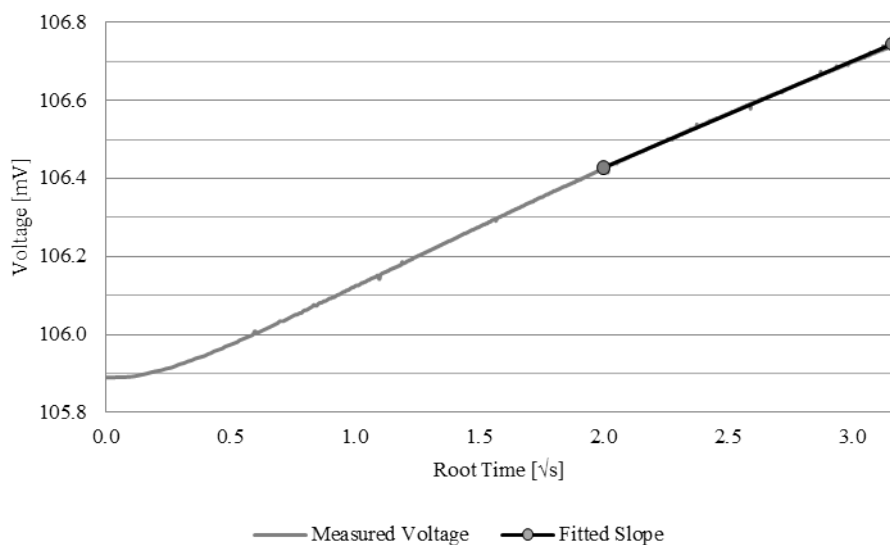
FIGURE 3.7: Measured voltage plotted against root time for a single blotter test. note the Initial non-linear behavior, followed by a constant rate of change starting at approximately $\sqrt{t} = 2$. This curve was generated for sample D30-4. Using the calibration constants $C_1 = 0.001776$, $C_2 = -0.13$, $C_4 = 0.0003332$, the conductivity of this sample was calculated to be 0.653 W/mK, a 262% increase over neat PBT.

For samples where the generated heat does not fully transverse the sample thickness during testing, a single blotter test was used. For this procedure, a single test was sufficient to calculate the thermal conductivity of the sample using the rate of change of the voltage m with respect to root time from inside the testing window, or from $t = 4$ ($\sqrt{t} = 2$) to $t = 10$ ($\sqrt{t} = 3.16$). An example of the voltage curve generated during testing is shown in Figure 3.7. This procedure is only valid when the voltage slope remains linear over the testing window. If

prior to $t = 10$, the voltage rate of change demonstrates time dependent behavior, heat has fully transversed the thickness of the sample and begun moving into the blotter. For these samples, a second test was performed in accordance with the dual blotter testing method discussed in §3.3.2.3.

3.3.2.3 Dual Blotter Testing
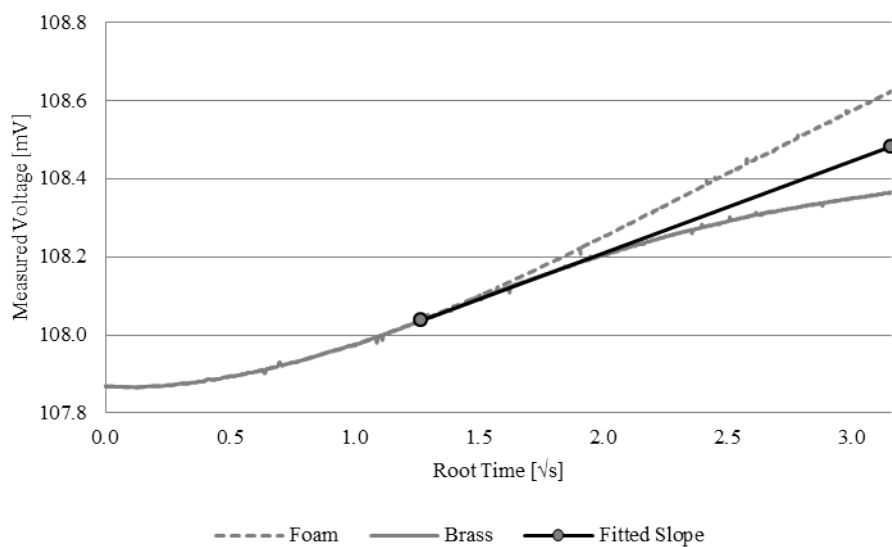
FIGURE 3.8: Measured voltage plotted against root time for a dual blotter test. Note the initial non-linear behavior, linear behavior, the divergence point, and continued non-linear behavior as the heat passes through the sample and into the blotter. A constant rate of change is extrapolated out from the divergence point. This curve was generated using a glass microscope slide. Using the calibration constants $C_1 = 0.001776$, $C_2 = -0.13$, $C_4 = 0.0003332$, the conductivity of this sample was calculated to be 0.797 W/mK.

For samples in which the conducted heat fully transverse the sample with the testing window, a dual blotter method was used. For this, two tests were performed, the first using a metal blotter and the second using a foam blotter. Because the thermal conductivity of the metal and foam bound the conductivity of the composite, the rate of change of voltage will decrease for metal or increase

for foam. By overlaying these two voltage curves as shown in Figure 3.8, a divergence point is identified and a constant rate of change at that point is assumed to represent the true conductivity of the composite. This rate of change is then used to calculate conductivity using Equation 3.3. A MATLAB code was created to perform this analysis semi-automatically.

3.3.3   Optical Microscopy

For optical microscopy, samples were mounted in transparent epoxy and polished for imaging. These micrographs were then analyzed to extract fiber orientation and distribution.

3.3.3.1   Mounting and Polishing

First, samples were mounted in $1.25\ in$ diameter two part mounting cups a transparent two part resin/hardener epoxy. Prior to curing, sample were placed in a vacuum of $30\ inHG$ for five minutes to remove air bubbles trapped in the epoxy. The vacuum was then reduced to $15\ inHG$ and the samples were allowed to fully cure, which took approximately two hours. Post cure, mounted samples were removed from mounting cups and polished using a MetPrep 4 semi-automatic polishing machine with neumatic powered head. Four polishing pads were used for various times and head force, which are listed in Table 3.5. The sample surface at the completion of each stage is shown in Figure 3.9.

Jason R. Nixon

TABLE 3.5: Mounted sample polishing pad grit, time, and head force. Pads were used in order of increasing grit during polishing.

Paper	[grit]	180	320	600	1200
Time	[m:s]	1:30	3:00	6:00	24:00
Force	[lbf]	8	8	8	14
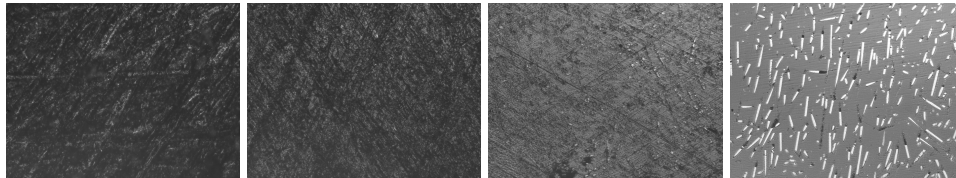
(a) 180 grit.   (b) 320 grit.   (c) 600 grit.   (d) 1200 grit.

FIGURE 3.9: Microscopy sample surface at 10X magnification after polishing using the pads, time, and head force listed in Table 3.5. Fibers are indicated as bright ellipses or circles (fiber cross section) in the image. Due to the thinness of obliquely aligned fibers at their leading edge, cylindrical voids frequently occur near the fiber edge due to fiber fracture

Samples were imaged using an Beuhler reflected light inverted microscope with attached Infinity 2 microscope camera located in the Modern Engineering and Materials Multi-Scale Measurements Laboratory at the University of Maryland. All micrographs were taken using 10X magnification. Other magnifications, 5X, 20X, 40X, were available and used, but these micrographs were not included in post-capture analysis. Micrograph images were captured using Infinity Capture software. Analysis using MATLAB was performed on these images to extract fiber orientation and distribution.

44

3.3.3.2 Fiber Orientation Analysis

Under the assumptions that fibers are approximately cylindrical along their axis and circular on their face, fiber orientation can be calculated with respect to the extrusion orientation (normal to the micrograph plan) using the major and minor axis of the ellipses identified in the micrographs. An illustration of the mapping of the measured ellipse onto the fiber is shown in Figure 3.10. The angle α is calculated using Equation 3.4.
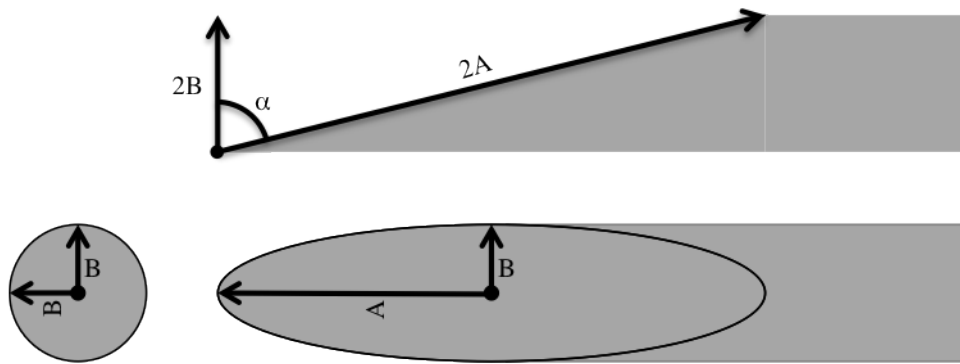
FIGURE 3.10: Illustration fiber orientation as a function of the ellipse formed by the intersection of the cylindrical fiber and the cut plane where A is the major axis, B is the minor axis which is equivalent to the fiber radius d_f, and ξ is the angle between the fiber axis and the cut plane. The fiber diameter is supplied by Toho Tenax of America as approximately 7 µm.

$$\alpha = \cos^{-1}\left(\frac{B}{A}\right) \tag{3.4}$$

Individual micrographs were collected into composite fiber orientation distributions for each condition. An example fiber orientation distribution, including the Figure 3.9(d), is shown in Figure 3.11. While this distribution is approximately

resembles a χ^2 distribution, this is coincidental and individual distributions tend

to less clearly form into a distinct form.
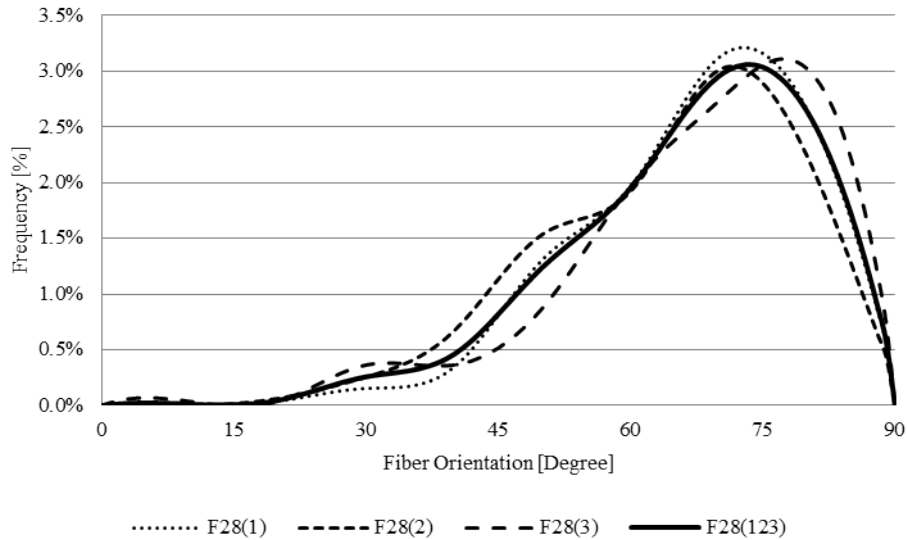
FIGURE 3.11: The distribution above presents the fiber orientation distribution the condition $Q = 1.81$ kg/hr, $V_\mu = 23.6$ vol.%, $V_n = 1.8$ vol.%, $\theta = 4.52°$. This include the micrograph shown in Figure 3.9(d). The majority of fibers are centered around approximately $70°$.

3.3.4 Statistical Analysis

In order to evaluate the effect of independent variables on measured properties, multiple linear regression analysis was performed using MATLAB.

In 5.3, regression analysis was performed using four independent variables, CMF concentration V_μ, MWNT concentration V_n, flow rate Q, and die angle θ. A build-down approach was used while constructing the regression model. Initially, all main effects, two-way interactions, three-way interactions, and four-way interactions were considered. We then consider the highest order interaction P-Values. We then remove the highest level effect with the greatest P-value

which is greater than 0.05. We then continue this process until only statistically significant and marginal effects remain.

For each fitted regression model, assumptions were checked and validated including linearity, normality, and scedasticity.

Chapter 4

Simulation

This chapter is divided into two sections: a theoretical examination of fiber reorientation supplemented by the work of Vincent and Agassant [86] and a computer simulation of CMF filled flow in a diverging channel during pumping. The intention of these studies was to examine the potential for fluid mechanical reorientation of CMFs during pumping as well as examine core characteristics of the process in an ideal environment. This simulation investigation was performed prior to experiments to qualitatively examine the interplay of divergence angle, die length, and die inlet/out ratio.

4.1   Theoretical Treatment

Vincent and Agassant [86] analyzed the experimentally examined the behavior of a single fiber in a diverging flow and developed a fluid mechanical description of the fiber behavior. In this section, the description of fiber motion will be examined and discussed as the basis for fiber orientation in a die during pumping from an extruder.

Dies are characterized by an inlet height of h_{in}, an outlet height of h_{out}, and a die length of L. From these, the die divergence angle θ can calculated using Equation 4.1. All dies considered are constructed to be straight ($\theta = 0°$) or diverging, i.e. $h_{out} \geq h_{in}$, or $\theta \geq 0°$. A list of die geometries (inlet height, outlet height, and length) can be found in Table 3.2 (Pg. 31).

$$\theta = \tan\left(\frac{h_{out} - h_{in}}{2L}\right) \tag{4.1}$$

Figure 4.1 illustrates the die and relevant angles within.

Fibers are considered to be passive with respect to the flow. They are also assumed to be ellipsoidal approximations of cylinders described by their by their major axis l_f (fiber length) and minor axis r_f (fiber radius). Fibers are assumed to have a circular cross section.

Vincent and Agassant provide a solution to the Stokes flow in a diverging channel. Using this solution, they calculated fiber angle ϕ with respect to fiber path based on the initial fiber angle ϕ_0 for a fiber traveling on the streamline defined
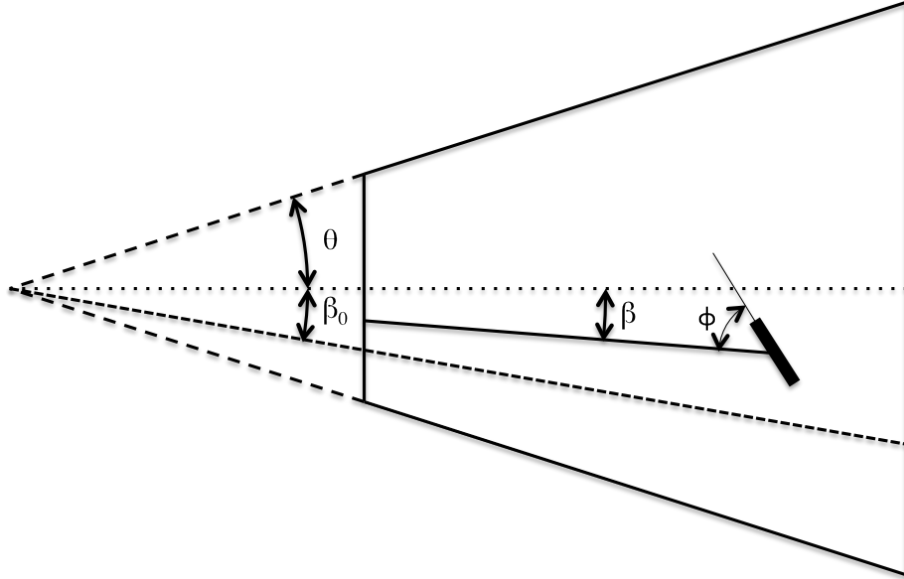
FIGURE 4.1: Illustration the die and relevant angles for the Vincent and Agassant die flow.

by the angle β. In this solution, the shear rate $\dot{\gamma}$ and extensional rate $\dot{\alpha}$ in an unperturbed diverging channel flow are defined as:

$$\dot{\gamma} = -\frac{A\left(\cos\left(2\beta\right) + \sin\left(2\theta\right)\right)}{\rho^2} \qquad (4.2)$$

$$\dot{\alpha} = -\frac{A\sin\left(2\beta\right)}{\rho^2} \qquad (4.3)$$

$$A = \frac{Q}{h\left(\sin\left(2\theta\right) - 2\theta\cos\left(2\theta\right)\right)} \qquad (4.4)$$

where Q is the inlet volumetric flow rate and h is the channel height at the fiber centroid. At large divergence angles β, both shear rate and extensional rate demonstrate non-linear behavior. However, in the range of die angles considered in this thesis, between $0°$ to $5°$, by the small angle approximation, the extensional rate is approximately linear over the channel arc. The normalized shear rates, across a sample die angle is shwon in Figure 4.2.
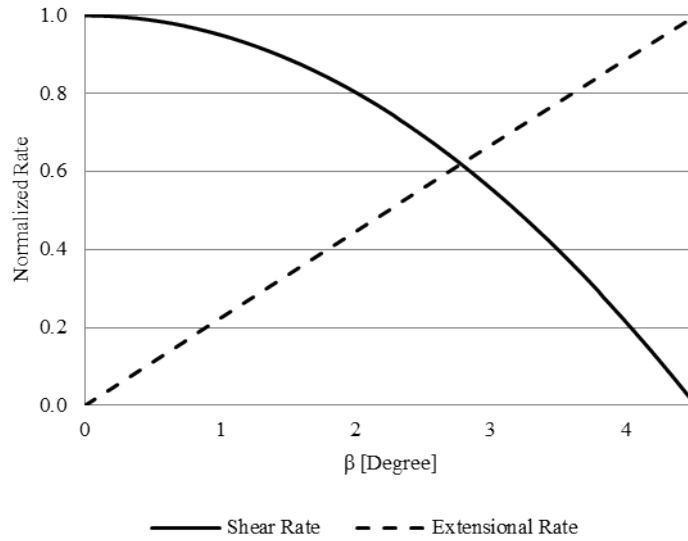
FIGURE 4.2: Normalized shear and extensional rates across the profile of a $\theta = 4.52°$ die operating at 4 lb/hr. Shear and extensional rates are respectively normalized by their absolute maximum values. This plot demonstrates the behavior of the rates across channel. Because of normalization, the intercept point is not not represented. The critical die angle for this channel is $2.02°$.

The time rate of change of the fiber angle is defined as:

$$\frac{d\phi}{dt} = r\left(\dot{\alpha}\sin\left(2\phi\right) + \dot{\gamma}\cos\left(2\phi\right)\right) + \dot{\gamma} \tag{4.5}$$

where the geometric factor r is defined as:

$$r = \frac{l_f^2 - r_f^2}{l_f^2 + r_f^2} \tag{4.6}$$

For the $100\,\mu\text{m}$ CMFs used in this dissertation, $r = 0.9902$. The behavior of a single fiber in the flow depends on the path angle β of the flow. When $\beta < \beta_0$, where β_0 is some critical angle, the fiber is observed to asymptotically converge to an equilibrium position that is approximately normal to the fiber

path orientation. When $\beta > \beta_0$, the fiber will behave as if in shear and converge asymptotically to an orientation nearly tangential to the fiber path. The critical angle β_0 in flow is defined as Equation 4.7.

$$\cos\left(2\beta_0\right) = r^2 \cos\left(2\theta\right) + \sqrt{\left(1 - r^2\right)\left(1 - r^2 \cos^2\left(2\theta\right)\right)} \tag{4.7}$$

This result implies that in the die pumping process, even with optimal fiber reorientation, near the edges of the sample, fibers will be mostly longitudinally aligned while fibers near the center of the sample will be more aligned in the through-thickness direction.

Three solutions to the diverging channel in the creeping flow regime are presented for various bounds of the fiber path angle: $\beta = 0$, $\beta < \beta_0$, and $\beta > \beta_0$.

$$\beta = 0: \qquad \phi = \tan^{-1}\left(C\rho^{-2r}\right) - \frac{\tau}{2} \tag{4.8}$$

$$\beta < \beta_0: \qquad \phi = \frac{X + Y + (X - Y)C\rho^{-2Y/\dot{\alpha}}}{\dot{\gamma}\left(1 + C\rho\rho^{-2Y/\dot{\alpha}}\right)} - \frac{\tau}{2} \tag{4.9}$$

$$\beta > \beta_0: \qquad \phi = \tan^{-1}\left(\frac{X}{\dot{\gamma}} - \frac{Y'}{\dot{\gamma}}\tan\left(\frac{Y'\log\left(\rho\right)}{\dot{\alpha}} + C\right)\right) - \frac{\tau}{2} \tag{4.10}$$

where τ, X, Y, and Y' are defined by:

$$\tau = \cos^{-1}\left(\frac{\dot{\alpha}}{\sqrt{\dot{\alpha}^2 + \dot{\gamma}^2}}\right) \qquad \text{or} \qquad \tau = \sin^{-1}\left(\frac{\dot{\gamma}}{\sqrt{\dot{\alpha}^2 + \dot{\gamma}^2}}\right) \tag{4.11}$$

$$X = r\sqrt{\dot{\alpha}^2 + \dot{\gamma}^2} \tag{4.12}$$

$$Y = \sqrt{\rho^2 \dot{\alpha}^2 + (r^2 - 1)\,\dot{\gamma}^2} \qquad (4.13)$$

$$Y' = \sqrt{(1 - r^2)\,\dot{\gamma}^2 - r^2 \dot{\alpha}} \qquad (4.14)$$

C is an integration constant based on the fiber orientation at the inlet of the die channel. Using the fiber path angle β, the fiber path orientation ϕ can be transformed into the fiber planar orientation by $\alpha = \phi + \beta$. Figure 4.3 demonstrates the idealized orientation (again, these equations assume a passive fiber which does not act upon the flow) across a vertical section at the die outlet, as one would observe when performing optical microscopy (§3.3.3). This demonstrates that there is indeed a core of highly aligned (with respect to the through thickness direction) fibers, while fibers more towards the walls of the die tend to be more aligned in the longitudinal direction. However, this is not necessarily an explicitly negative consequence as the outer shell of the sample may help the sample retain tensile properties while the core increases thermal conductivity.
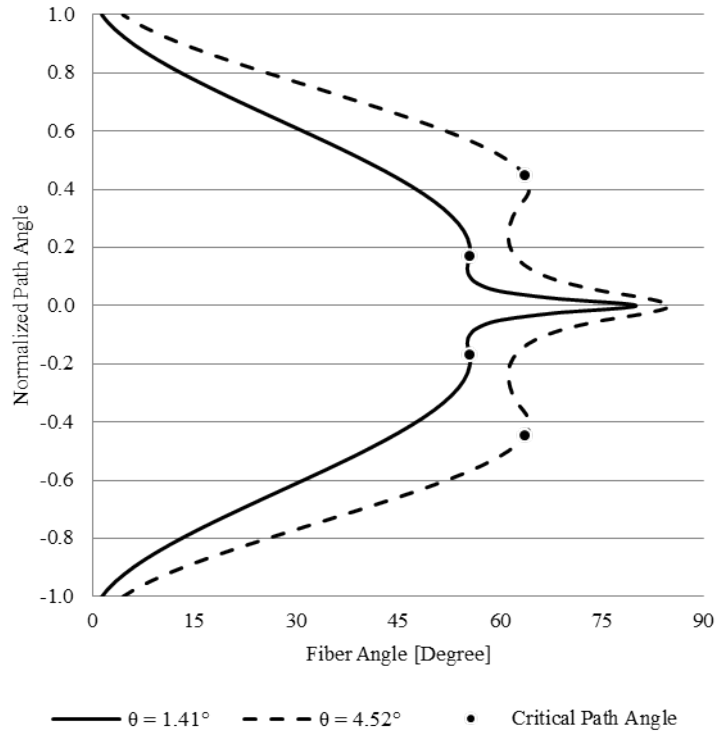
FIGURE 4.3: Fiber angle α plotted against normalized fiber path angle β/θ. The local fiber angle increase near the critical path angle is a geometric artifact arising from the examination of a vertical section of the channel rather than an arc. Fibers which are closer to the critical path experience a greater time in the die, and are thus are slightly more orientated to their infinity time orientation than fibers near $\beta_0/2$. The generating conditions for these profiles are listed in Table 4.1.

TABLE 4.1: Characteristic fiber orientation profile input parameters for profiles presented in Figure 4.3.

θ	1.41°	4.52°
h_{in}	1 mm	1 mm
h_{out}	5 mm	3.5 mm
L	25.4 mm	50.8 mm
l_f	100 μm	100 μm
d_f	7 μm	7 μm
β_0	0.24°	2.02°

The work of Vincent and Agassant [86] is a central framework that demonstrates the effectiveness of fiber reorientation during a pumping process. However, by these calculations, we see that zoned structure forms, where near the center of

54

the flow, fibers are oriented towards normal to the flow path, and near the die

walls, oriented closely to the flow path.

4.2   Simulation

Prior to experimental work fiber reorientation in convergent, straight, and diverging channels was simulated and qualitatively examined. The study of fiber orientation in the die of a pumping device is critical to the fluid mechanical manipulation of fiber orientation.

During pumping, as discussed in §4.1, a number of factors effect fiber orientation. These system inputs include flow rate, filler volume fraction filler geometry, the flow regime, i.e. shearing and extensional flows, the geometric specification of the flow geometry. Similar results using injection molding have been demonstrated by Gupta and Wang [100]. Furthermore, post pumping processes, such as drawing, have also been shown to have an effect on fiber orientation [101, 102].

Simulation of fiber orientation during pumping through a die was performed using Autodesk's Moldflow software, which uses the Fulgar-Tucker model to approximate the fiber orientation using a high order tensor approximation. The core of this simulation is the Fulgar-Tucker (FT) model, a tensor valued approximation of the fiber orientations probability backed by laboratory experiment [103, 104]. Results gathered from these simulations can then be used to make predictions about final fiber orientation.

4.2.1 Method and Procedure

Initially, three dies were studied: a convergent die, a straight die, and a divergent die. Two system parameter were varied: volumetric flow rate and volumetric filler concentration. Convergent dies are nearly ubiquitously used in Fused Deposition Modeling (FDM) printing processes, which is itself a small scale extrusion pumping process, as well in screw extrusion processes. Straight dies are also frequently used in extrusion processes. Through straight and diverging dies, fibers become oriented nearly parallel to the sheet plane, parallel to the extrusion orientation [105].

Three values of flow rate and three values of CMF concentration were tested, for a total of nine conditions per die, for a total of twenty-seven conditions. Three values of CMF concentration were chosen: 0 vol.%, 10 vol.%, and 20 vol.%. For flow rate, the volumetric rates corresponding to lbh3, lbh3, and lbh5 were used (using the material properties of PBT).

Material profiles (material and simulation parameters) in Moldflow are predefined in the Moldflow material library. Simulations in Moldflow rely on both experimentally determined material properties and simulation specific parameters Therefore, a different material profile was chosen for each CMF concentration. PBT material profiles were chosen at 0 vol.%, 10 vol.%, and 20 vol.%. The grade of PBT used was selected to most close reflect the measured and manufacturer specified properteis of the PBT used throughout the dissertation.

In each simulation, fiber orientation tensor value is tracked. The simulation solution provides the value at each mesh node [103, 104] After simulation, the fiber orientation tensor is interpolated between nodes and extracted as a graphic. Because this parameter is a tensor field, individual fibers and local fiber properties cannot be tracked. Additionally, complex fiber interaction phenomenon such as breakage or networking cannot be modeled using this technique.

4.2.2   Characteristic Convergent Die

Figure 4.4 shows a characteristic convergent die fiber orientation color plot at 20 vol.% and lbh5.

The qualitative results are coded such that: black indicates that a fiber is parallel to the fiber path while white indicates that the fiber is perpendicular to the fiber path As the grey scale color increase from black to white, fibers are orienting away from the fiber path. In the simulation, the orientation ranges from zero to one, where zero indicates that the fiber is perpendicular to its path, and one corresponds to a parallel fiber with respect to path.
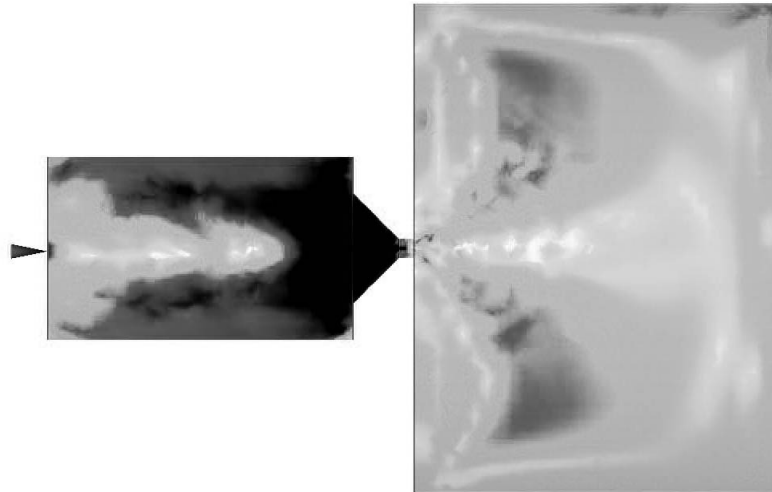
FIGURE 4.4: Characteristic converging die color map (at 20 vol.% and lbh5).

There are several ubiquitous features between all convergent die simulations. First, fibers tend to be highly aligned with respect to path prior to and in the die. This is resultant from 1) the shear flow through this channel and 2) from from the decreasing die height and subsequent increase in speed of the fiber during pumping. By the design of the simulation, fiber orientation results immediately after the die are meaningless.

FIGURE 4.5: Convergent die conditions. Columns from left to right: lbh3, lbh4, and lbh5. Rows from top to bottom: 10 vol.% and 20 vol.%.

With increasing CMF concentration, increasing fiber alignment is found with decreasing flow rate. As the flow rate increases, a core of decreased alignment forms in the center with higher relative alignment between the liquifer boundaries and the core of de-alignment. At flow rate increases, the region of lower alignment extends further towards the wall. This behavior is occurs at all CMF concentrations. Increasing CMF concentration leads to increased fiber alignment. This is becomes clear when comparing 10 vol.% and 20 vol.% at lbh5. At higher CMF concentration, the core de-aligned core increases in size over comparable flow rates.

4.2.3 Characteristic Straight Die

Figure 4.6 shows a characteristic straight die fiber orientation color plot at 20 vol.% and lbh5.
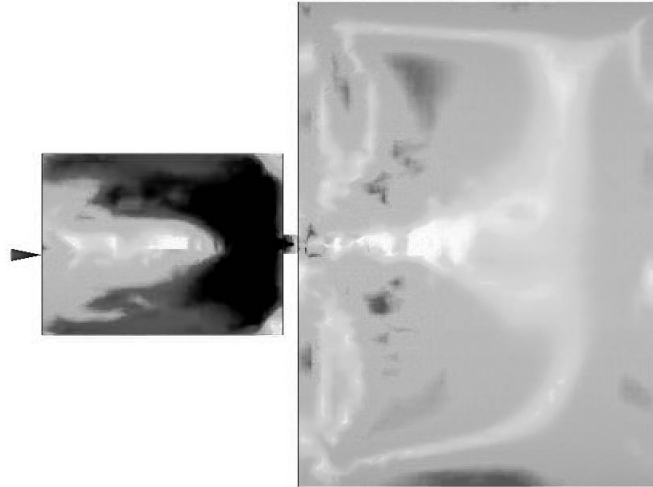
FIGURE 4.6: Characteristic straight die color map (at 20 vol.% and lbh5).

At the dies inlet, fibers are highly aligned. Once the die, fibers tend to de-align before the end of the die. At the die inlet, there is core of high fiber alignment. Near the wall, fiber alignment is low. This result is unexpected, given that a shear flow acts to align fibers with respect to path. However, this behavior is likely explained by the relatively short length of the straight channel. Given a higher channel length, it is expected that fibers would again align with path, resulting in the characteristically aligned pattern that is see in literature and experiments within this dissertation.
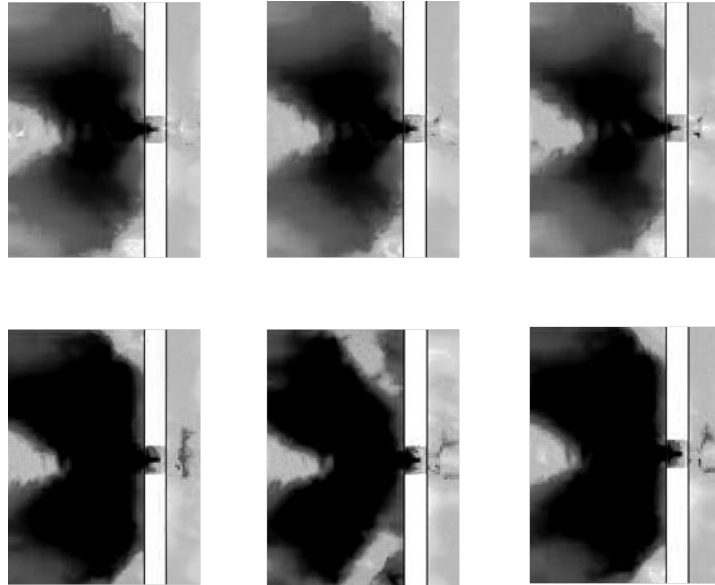
FIGURE 4.7: Straight die conditions. Columns from left to right: lbh3, lbh4, and lbh5. Rows from top to bottom: 10 vol.% and 20 vol.%.

Controlling for flow rate, increasing CMF concentration correlates with increased fiber alignment pre-die and further penetration of a high alignment core in the die. CMF concentration also correlates to increasing fiber alignment pre-die and in-die. There is little noticeable effect of flow rate at 10 vol.%. At 20 vol.%, increasing flow rate leads to higher fiber alignment prior to, but little noticeable change in the actual straight zone of, the die. Comparison between 10 vol.% and 20 vol.% shows that the global fiber orientation pre-die is much greater in the 20 vol.% than 10 vol.%. Additionally, at 20 vol.%, the vorticies present in the corner as a result of the right angle produces much higher fiber alignment at 20 vol.% than 10 vol.%. It is also likely that the instantaneous transition from large die height to the channel height leads to adverse conditions shortly after fibers enter the die.

4.2.4 Characteristic Diverging Die

Figure 4.8 shows a characteristic diverging die fiber orientation color plot at 20 vol.% and lbh5.
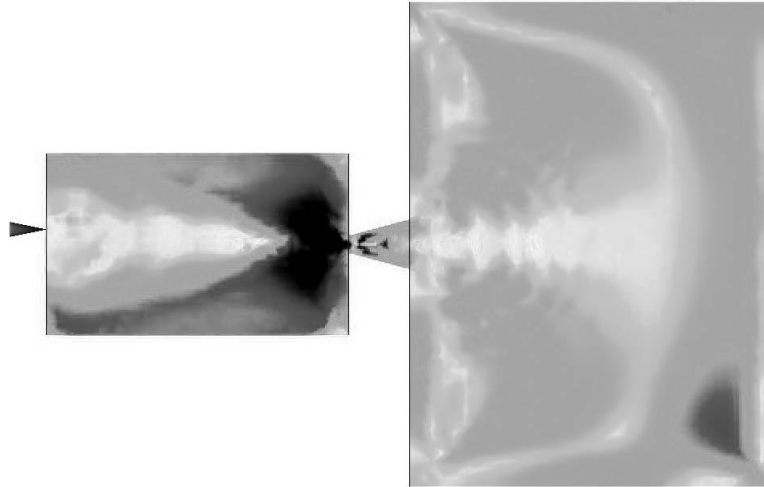
FIGURE 4.8: Characteristic divergent die color map (at 20 vol.% and lbh5).

Prior to the die, fibers are shown to close align with respect to path. This is a result of the high shear in this region and the many converging flow paths. Second, immediately after entering the die, the fibers rapidly de-align with respect to path.
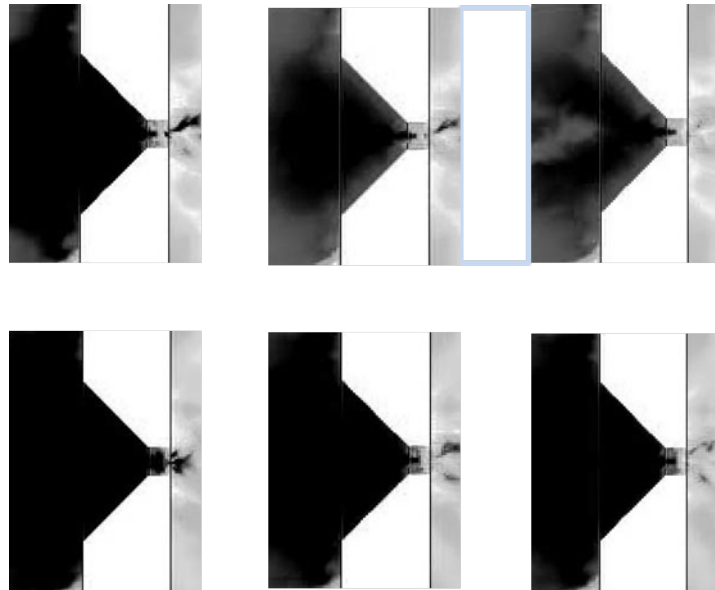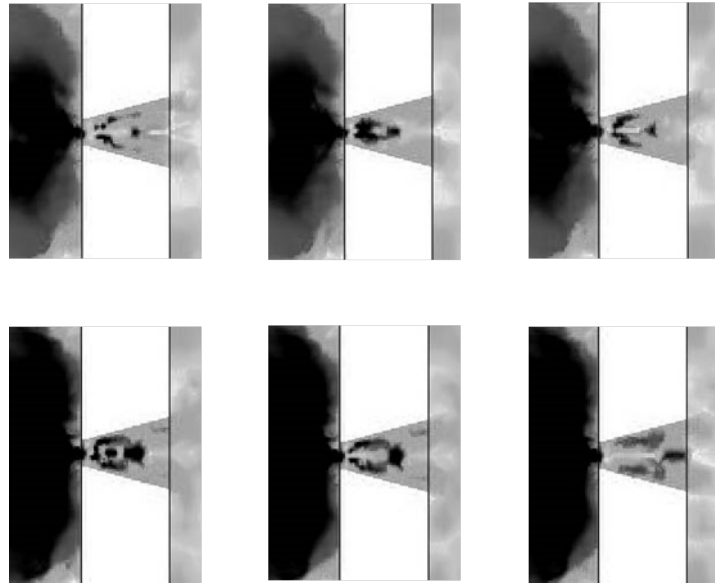
FIGURE 4.9: Divergent die conditions. Columns from left to right: lbh3, lbh4, and lbh5. Rows from top to bottom: 10 vol.% and 20 vol.%.

At 10 vol.% and 20 vol.%, increasing flow rate correlates to increasing pre-die fiber alignment. At the outlet, a core of low alignment with higher alignment near the boundary forms. With increasing flow rate, fiber alignment in the core increases. , indicating that lower flow rates result in a decreased fiber alignment. In each condition, the placement, size, and intensity of the highly aligned shell varies. This is a result of the interplay between extensional and shear flow mechanisms present in the channels as discussed in §4.1.

4.2.5 Summary

Across all geometries, fiber orientation preceding the die does not significantly effect the fiber orientation in the die. Immediately prior to the die channel, shear rate increases, leading to an increase in fiber alignment.

In the convergent die, high fiber alignment (fiber is nearly parallel with the fiber path) is observed throughout the die. Both increasing CMF concentration and increasing flow rate were found to increase alignment in-die. For higher flow rates, a banded structure was found across the die inlet, such that center alignment was slightly less aligned than near the die walls.

In the straight die, fibers were found to enter the die highly aligned, followed by rapid de-alignment between the fiber and path. As with the convergent die, a core of high alignment was observed in the center of the die. Increasing CMF concentration and flow rate resulted in increased alignment and greater down-channel penetration of high alignment into the die. Die channel length greatly affects the rate and orientation of the final fiber orientation. However, from a practical standpoint, the flow profile of the melt in a straight die would lead to increased stress over the convergent die, and thus greater fiber-fiber interactions.

In aggregate, fibers in the the divergent die were found to be nearly perpendicular to the flow path. As identified by Vincent and Agassant [86], in addition to the extensional effects that reduce fiber alignment near the center of the die the die, shear-like effects near the wall resulted in more aligned fibers. The usefulness of the diverging die lies in its ability to de-align fibers towards the die outlet, resulting in fibers aligned towards the through-thickness direction of the sheet rather than the axial direction that is currently found in CMF loaded die flow.

Chapter 5

Experiments

This chapter is divided into three sections corresponding to a progression of experiments examining multiscale composite properties. First, long CMF 6 mm multiscale composite properties $\theta = 0°$ are presented and basic trends in multiscale property behavior with respect to CMF concentration and MWNT concentration are discussed in §5.1. These results are representative of classic pumping (i.e. fibers aligned strongly in the flow orientation). Second, in §5.2, short CMF 100 µm multiscale composite properties $\theta = 0°$ and $\theta = 2.82°$ are presented and compared to long CMF properties. Basic trends between straight and diverging die composite properties are discussed. Finally in §5.3, a parametric study across CMF concentration, MWNT concentration, flow rate, and die angles is conducted. This data was analyzed using multiple regression analysis and included data from §5.2. Trends between independent parameters on physical properties are discussed.

5.1   Long CMF Multiscale Study

(a) 10 wt.% CMF.

(b) 15 wt.% CMF.

(c) 20 wt.% CMF.

(d) 25 wt.% CMF.

(e) 30 wt.% CMF.
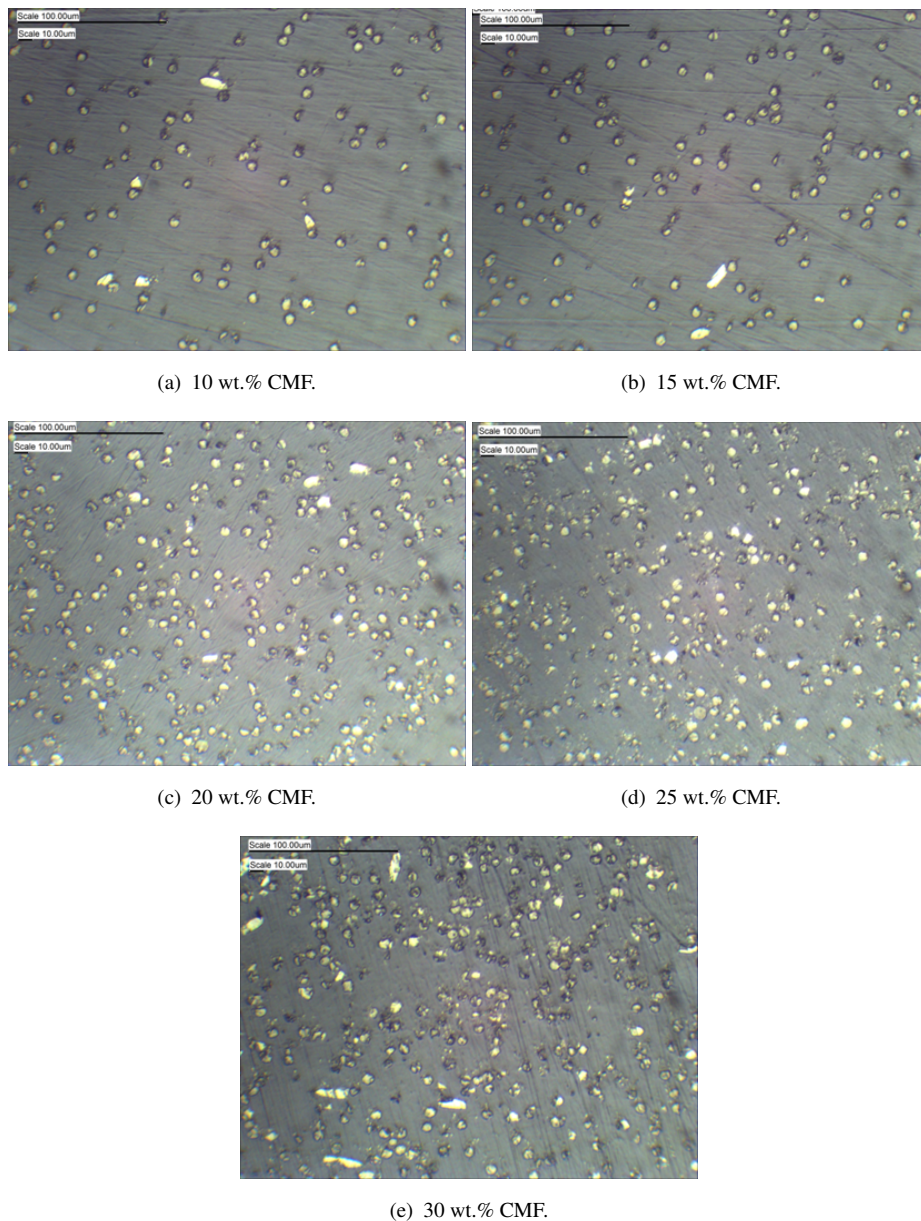
FIGURE 5.1: 6 mm CMF characteristic micrographs samples compounded at 0 wt.% MWNTs, $\theta = 0°$, 4 lb/hr, and 200 rpm. Fibers are indicated by bright circular or ellipsoidal profiles against the darker matrix. Fiber orientation was not found to be effected by MWNT concentration.

Micrographs in Figure 5.1 are characteristic of fiber orientation at different CMF concentrations. Fibers are indicated as bright circular or ellipsoidal cross sections on the darker polymer matrix background. MWNT concentration was not found to significantly effect observable microscale structure. Visual inspection of these micrographs indicates that fibers are well-aligned with the axis of extrusion (normal to the micrograph plane). Fiber orientation analysis indicates that the fibers are aligned within $10°$ of the extrusion axis. Fiber orientation was determined using the angle analysis tools discussed in §3.3.3. Sources of variance in this analysis include micrograph resolution, sample flatness during mounting, and small perturbations in flow during extrusion. At the resolution given, a single pixel of resolution error can lead to a degree or more of error in the fiber angle calculation. Visual inspection also indicates the onset fiber exfoliation and premature fracture at CMF concentrations exceeding 25 wt.% CMF. This is evidenced by the regular and circular fiber cross sections found in Figure 5.1(c) as compared to the non-uniformed and ragged fiber cross section in Figure 5.1(e). These ragged cross sections are likely a results of two mechanisms. First, due to the high CMF aspect ratio ($A_r = 600$), high CMF stiffness, and moderately aggressive screw geometry, it is very likely that CMFs are fracturing during compounding. This theory is also demonstrate in observed tensile properties later in this section. Fractures occurring at an oblique angle with respect to the fiber axis plane will create non-circular cross sections. During fracture, it is likely that small fiber fragments are released and further broken up, much as a spherical agglomerated filler is broken down into small particles by dispersive mixing, leading to the small CMF elements found in high CMF

loading micrographs.
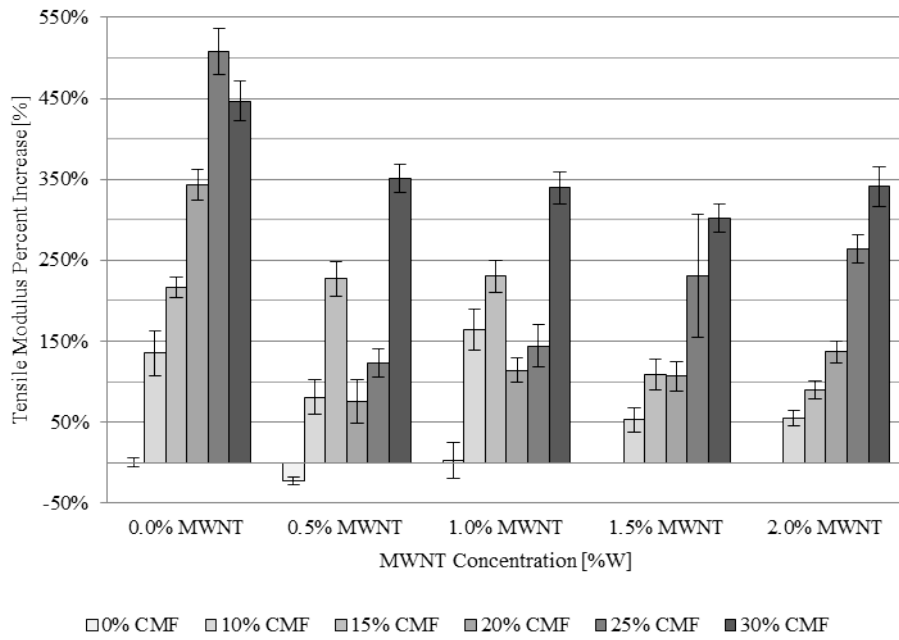
(a) Organized by MWNT concentration.
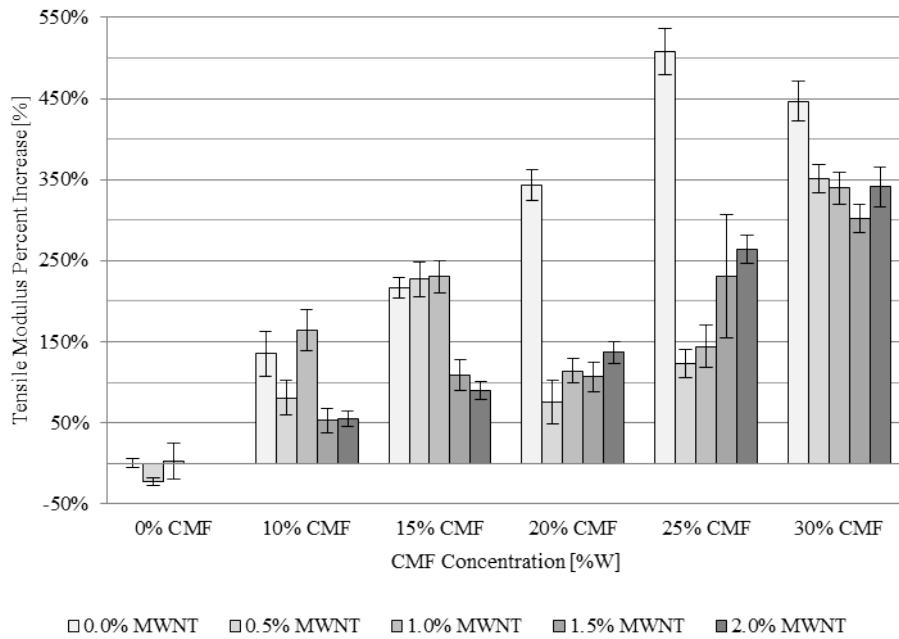
(b) Organized by CMF concentration.

FIGURE 5.2: 6 mm CMF mean tensile modulus percent increase for samples compounded at $\theta = 0°$, 1.81 kg/hr, and 200 rpm. The tensile modulus of neat PBT is 2.42 GPa. The maximum tensile modulus increase, 508% (14.66 GPa), is observed at 25 wt.% CMF and 0 wt.% MWNT. Error bars represent one standard deviation of the measured data.

Inspection of Figure 5.2(a) shows that tensile modulus generally increases linearly with respect to CMF concentration, with the exception that between 15 wt.% and 20 wt.% CMF, there is a significant drop in stiffness before the linear trend resumes. This is likely due to additional fiber damaged incurred during the pelitization and remelting of the 15% CMF/PBT batch. In general, the stiffest samples are found using only CMF. The introduction of MWNTs appears to dramatically reduce the overall stiffness of the composite by up to 100%. The stiffest material possible occurs using 25 wt.% CMF, and is nearly 500% stiffer than neat PBT. Purely CMF loaded composites also demonstrate a characteristic lack of increase in tensile modulus from 25 wt.% to 30 wt.%. It is also important to note that with a non-zero MWNT concentration, the lack of tensile modulus increase from 25 wt.% to 30 wt.% CMF is not present in any case. In the case of 0% MWNT, this is likely the second onset of process induced fiber damage, the first of which occurs between 15 wt.% CMF and 20 wt.% CMF and which was dodged by introducing the CMF/PBT batching process. In another study, a second CMF/PBT batching process was performed 25 wt.% CMF to examine the potential of incorporating up to 40 wt.% CMF. The diminishing return of tensile modulus increase was observed to cease, but no more increase was gained either. It is theorized that at this level of loading, so much fiber damage has been incurred due to the higher loading and two-run batching process that it was not possible to exceed the 30 wt.% limit without the use of a larger TSE.
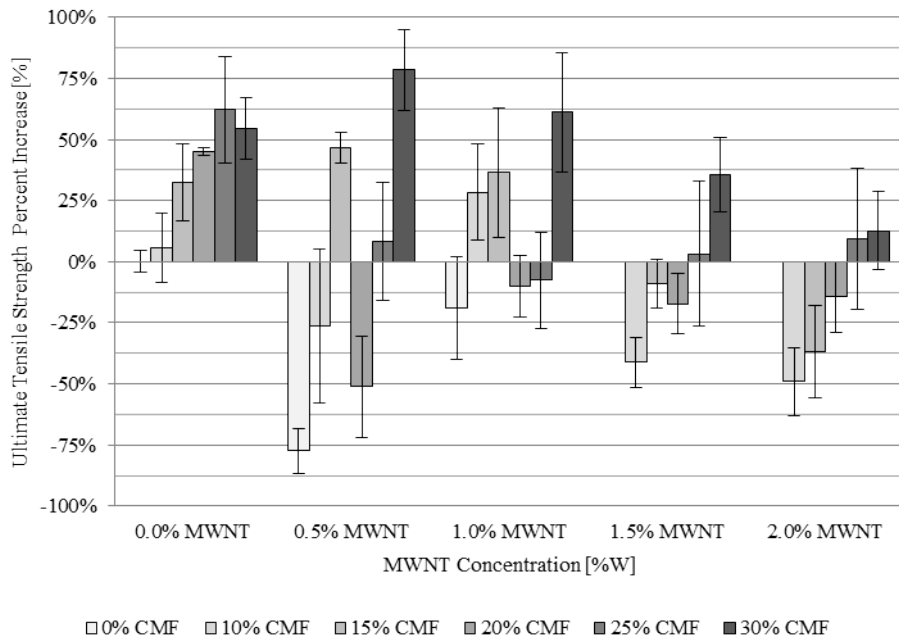
(a) Organized by MWNT concentration.
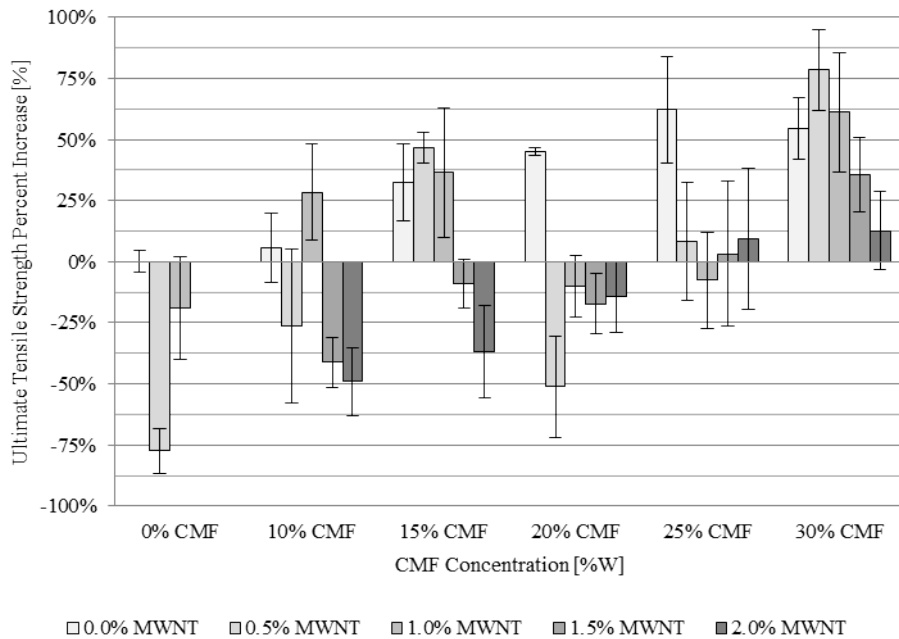
(b) Organized by CMF concentration.

FIGURE 5.3: 6 mm CMF mean ultimate tensile strength percent increase for samples compounded using $\theta = 0°$ at 1.81 kg/hr and 200 rpm. The measured ultimate tensile strength of neat PBT is 49.0 MPa. The maximum ultimate tensile strength percent increase, 78% (87.2 MPa), is observed at 30 wt.% CMF and 1.0 wt.% MWNT. Error bars represent one standard deviation of the measured data.

For ultimate tensile strength of long fiber composites shown in Figure 5.3, the maximal improvement, controlling for MWNT concentration, is found at 30 wt.% CMF. While not present in all MWNT concentration, linearly increasing trends were observed at 0.0 wt.% MWNT ($R^2 = 0.912$), 1.5 wt.% MWNT ($R^2 = 0.863$), and 2.0 wt.% MWNT ($R^2 = 0.960$). In general, it appears that in the presence of MWNTs, greater than 15 wt.% CMF is needed for the composite ultimate tensile strength to exceed the ultimate tensile strength of neat PBT. The variance in measured ultimate tensile strength, as evidenced by the significant standard deviations observed, could lie in the testing specimen preparation or in the composites themselves, in which locally non-favorable microstructures lead to premature failure.
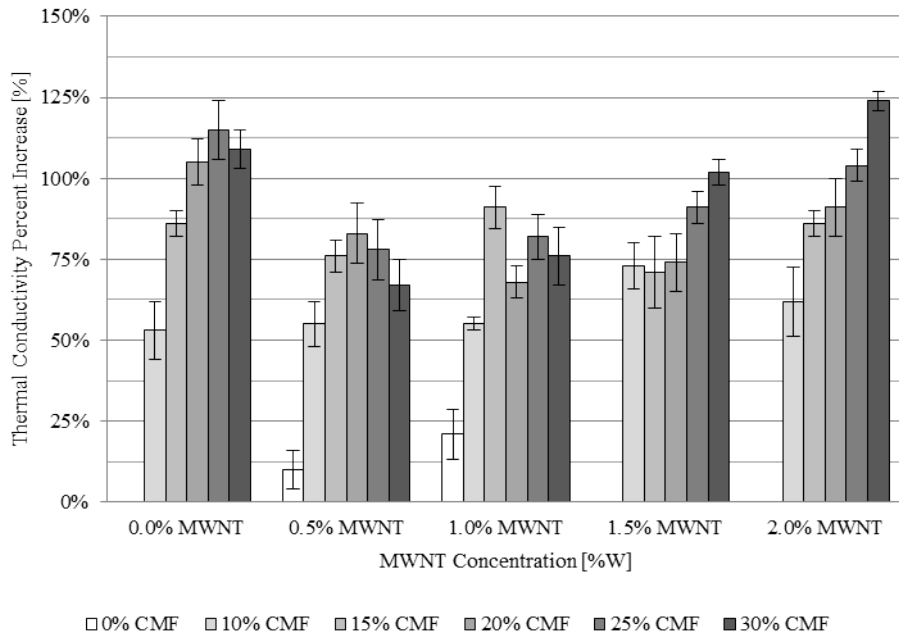
(a) Organized by MWNT concentration.
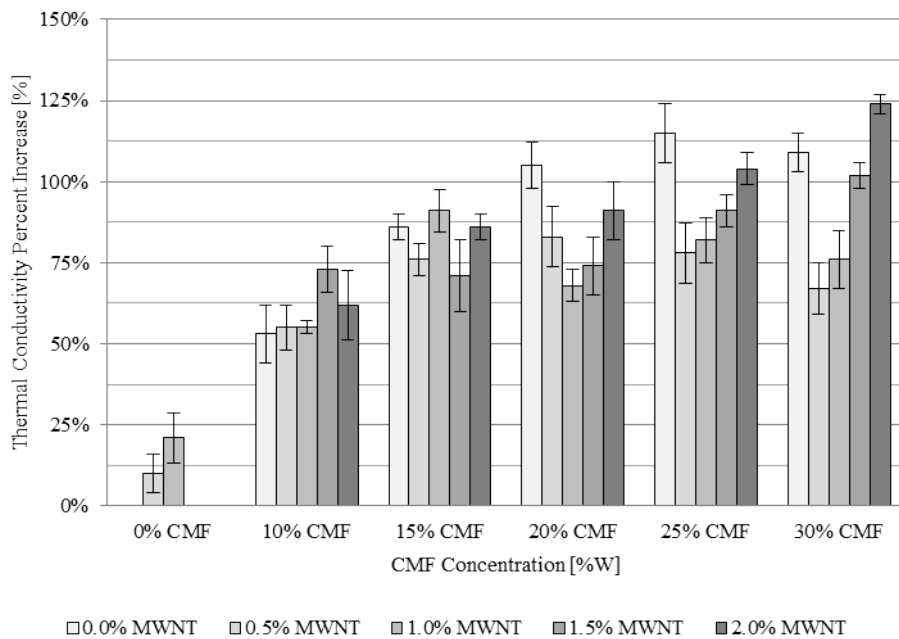
(b) Organized by CMF concentration.

FIGURE 5.4: 6 mm CMF mean thermal conductivity percent increase for samples compounded at $\theta = 0°$, 1.81 kg/hr, and 200 rpm. The measured thermal conductivity of neat PBT is 0.18 W/mK. The maximum long CMF thermal conductivity percent increase, 200% (0.54 W/mK) is observed at 25 wt.% CMF, and 30 wt.% CMF and 2.0 wt.% MWNT. Error bars represent one standard deviation of the measured data.

74

For 0 wt.% MWNT, there is a linear trend from 0 wt.% CMF to 25 wt.% CMF ($R^2 = 0.949$), followed by a drop off at 30 wt.% CMF, consistent with the attrition limit. At loadings at or below 15 wt.% CMF, the inclusion of MWNTs acts to increase the thermal conductivity at lower MWNT concentration (up to 1.0 wt.% MWNT) followed by a decrease again. At MWNT concentrations above 1.5 wt.% MWNT, it was found the inclusion of MWNTs universally acted to decrease the thermal conductivity of a composite with equivalent LCMF but no MWNT loading.

This is thought to be a result of several possible mechanisms. First, the inclusion of MWNTs into the polymer matrix acts to increase the apparent viscosity. This effect combined with increased fiber-fiber interactions at higher loadings may result in more fiber fracture during compounding, leading to shorter paths for improved thermal conduction between thermal interface barrier present between CMFs and the matrix material. Second, at higher MWNT loadings, MWNT are likely agglomerating, leading to reductions in over thermal conductivity improvement. Third, at higher MWNT loadings, there are potentially more thermal resistance barriers in the polymer matrix between the MWNTs and polymer matrix [106]. Longitudinal tensile modulus and ultimate tensile strength are universally enhanced by the presence of CMFs. In general, MWNTs appear to reduce the tensile modulus and ultimate tensile strengths, except at 15 wt.% CMF and 30 wt.% CMF, where 0.5 wt.% MWNT is found to improve the modulus and strength. These two CMF concentrations, 15 wt.% and 30 wt.% CMF are extruder loading limits related to the screw geometry, screw dimensions, and

fibers. It is possible that the onset of CMF concentration induced fiber damage and MWNT concentration are correlate to synergistic mechanical enhancement.

Transverse thermal conductivity is not enhanced significantly by the presence of MWNTs, except again at 15 wt.% CMF at 0.5 wt.%, 1.0 wt.%, and 2.0 wt.% MWNT at 30 wt.% CMF and 2 wt.% MWNT. Again, the highest improvement is found at the loadings in which the most fiber damage occurs. Therefore, it is possible that the inclusion of MWNTs may produce synergistic property enhancement with shorter fibers over longer fibers.

Due to the extreme length of long CMFs (6 mm), short CMFs will be used instead in subsequent sections. While a reduction in properties is expected due to reduced fiber length (literature indicates that for both thermal and tensile improvement, longer fibers are preferred over short fibers), the shorter length scale of fiber is needed due to geometric constrains in dies with non-zero divergence angle. Furthermore, this may capitalize on the apparent benefit of shorter CMFs and MWNT concentration observed in this section.

5.2   Short Fiber Diverging Die Study

In this section, the effect of two die angles, $\theta = 0°$ (A) and $\theta = 2.82°$ (E) was examined across the range of CMF concentrations, 10 wt.%, 15 wt.%, 20 wt.%, 25 wt.%, and 30 wt.% and MWNT concentrations, 0 wt.% and 2 wt.%. Flow rate, screw speed, and vacuum pressure were controlled at 1.81 kg/hr, 200 rpm, and 500 mmHG. A total of new 20 conditions were studied in this section. New short CMF results are compared against long CMF results in §5.1. Basic trends comparing straight and diverging dies are discussed, as well as the relationship between long CMF and short CMF properties.

New results are tabulated in Table A.2 ($\theta = 0°$) and Table A.5 ($\theta = 2.82°$) .

5.2.1   Long/Short CMF Comparison

This section compares short 100 μm CMF and long 6 mm CMF multiscale composite property results to establish the relatively small reduction in properties when reducing fiber length.

Analysis of micrographs for short CMF micrographs, which are characteristically represented in Figure 5.5 shows that, again, only a statistically insignificant portion of the fibers imaged are oriented out of the extrusion orientation. Comparison shows between 0 wt.% MWNT and 2 wt.% MWNT again shows no detectable difference. At 25 wt.% and more intensely in 30 wt.%, fiber damage is clear, matching the trend observed in long CMF micrographs shown in Figure 5.1.
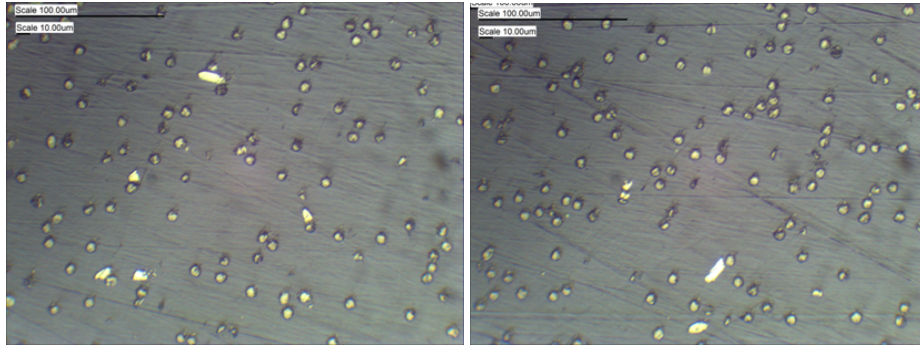
(a) 10 wt.% CMF.

(b) 15 wt.% CMF.
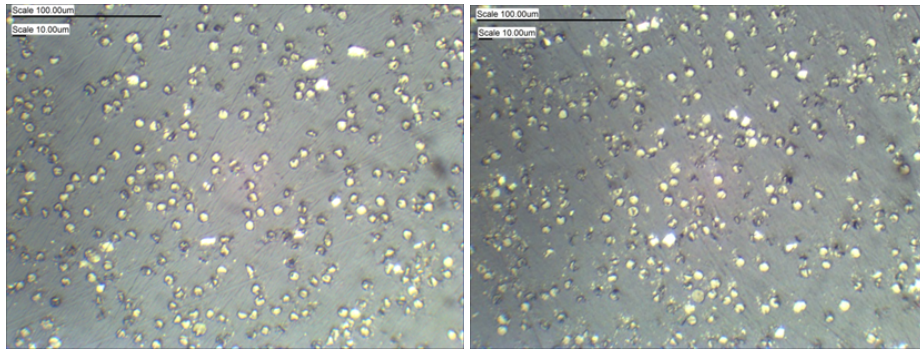
(c) 20 wt.% CMF.

(d) 25 wt.% CMF.
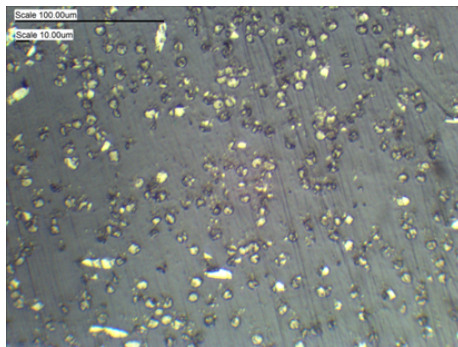
(e) 30 wt.% CMF.

FIGURE 5.5: Short CMF characteristic micrographs ($\theta = 0°$).
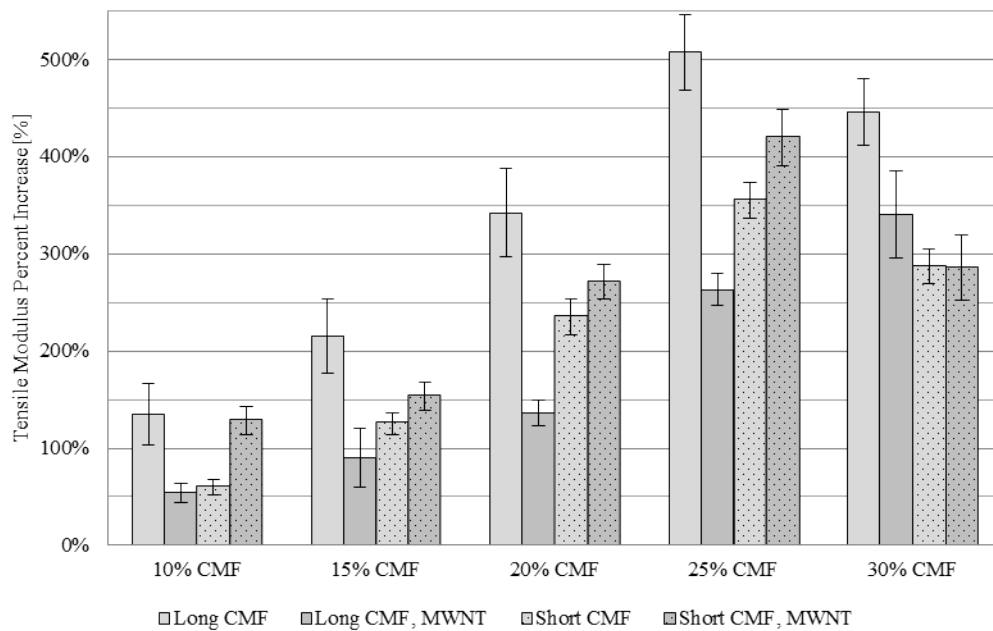
FIGURE 5.6: Comparison of 6 mm CMF and 100 μm CMF tensile modulus percent increase, compounded at $\theta = 0°$ at 1.81 kg/hr and 200 rpm. The measured tensile modulus of neat PBT is 2.42 GPa. The maximum short CMF tensile modulus increase, 420% (12.58 GPa), is observed at 25 wt.% CMF and 2 wt.% MWNT. Error bars represent one standard deviation of the measured data.

Using short CMFs, for both 0 wt.% and 2 wt.% MWNT concentrations, stiffness linearly increases with respect to CMF concentration ($R^2 = 0.908$ and $R^2 = 0.943$ respectively) from 0 wt.% to 25 wt.% CMF, From 25 wt.% to 30 wt.% CMF, and an appreciable decrease in properties in tensile modulus increase occurs. Again, this is likely related to extruder geometry and filler geometry limits that occur between 25 wt.% and 30 wt.%. The presence of short CMFs universally increases the tensile modulus of the composites. Comparison between long CMF and short CMF tensile modulus, controlling for MWNT concentration, shows that at 0 wt.% MWNTs, short CMF tensile moduli are approximately 30% lower than long CMF moduli, and at 2 wt.% SCMF moduli are approximately 45%

greater long CMF tensile moduli. By using short CMF, MWNTs increase tensile modulus rather than decreasing it.
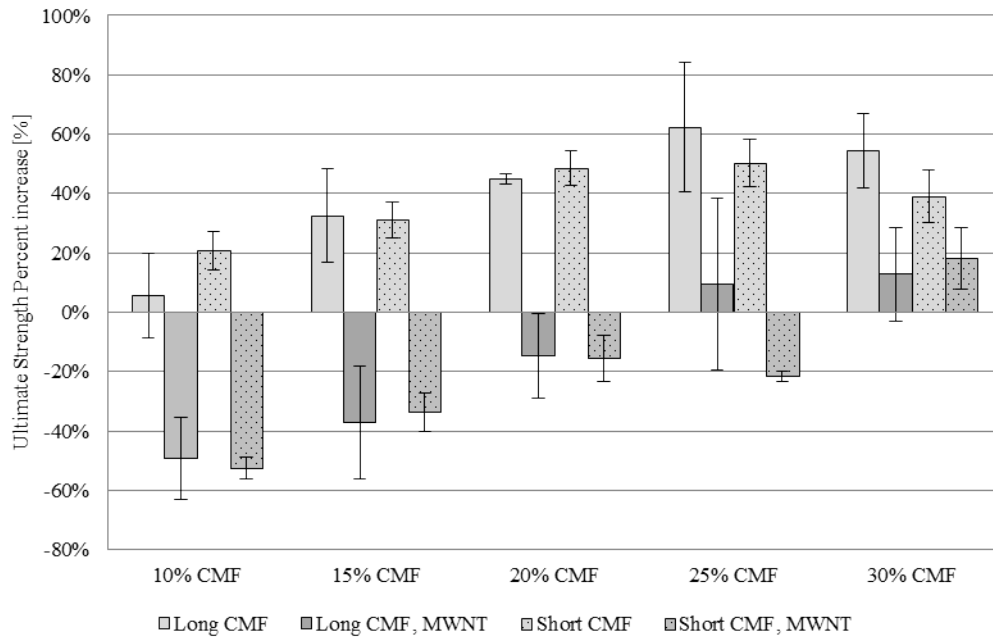
FIGURE 5.7: Comparison of 6 mm CMF and 100 µm CMF ultimate tensile strength percent increase, compounded at $\theta = 0°$ at 1.81 kg/hr and 200 rpm. The measured ultimate tensile strength of neat PBT is $\sigma_u = 49\ MPa$. The maximum short CMF ultimate tensile strength increase, 50% (75.6 MPa), is observed at 25 wt.% CMF and 0 wt.% MWNT. Error bars represent one standard deviation of the measured data.

The presence of MWNTs universally reduces the ultimate tensile strength of the composite. Linear trend is observed is observed between CMF concentration and ultimate tensile strength, although this trend is not statistically significant. At 0 wt.% MWNT and 2 wt.% MWNT concentrations, comparison between short CMF and long CMF conditions shows that ultimate tensile strength is comparable. 25 wt.% MWNT remains an exception to this trend. It is possible that this variation is related to processing variance, or potentially to the onset of fiber damage due to extruder loading with respect to fiber size.
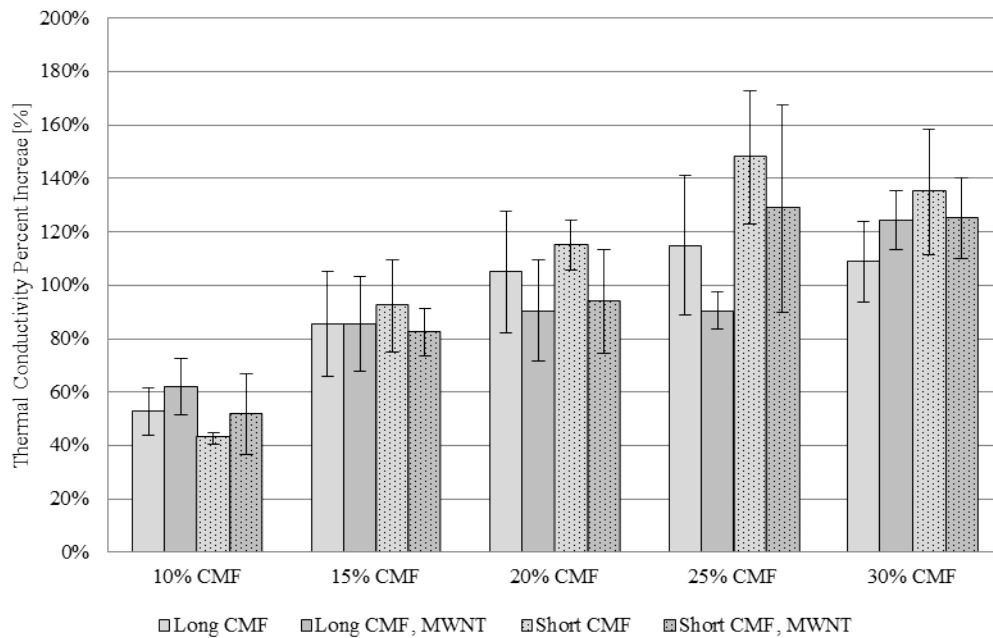
FIGURE 5.8: Comparison of 6 mm CMF and 100 μm CMF thermal conductivity percent increase, compounded at $\theta = 0°$ at 1.81 kg/hr and 200 rpm. The measured thermal conductivity of neat PBT is 0.180 W/mK. The maximum short CMF thermal conductivity increase, 148% (0.466 W/mK), is observed at 25 wt.% CMF and 0 wt.% MWNT. Error bars represent one standard deviation of the measured data.

Figure 5.8 shows that the thermal conductivity of both 0 wt.% and 2 wt.% samples have a relatively linear increase in thermal conductivity from 0 wt.% to 25 wt.%: ($R^2 = 0.927$) and ($R^2 = 0.959$) respectively, followed by a decrease from 25 wt.% to 30 wt.%. The greatest increase in thermal conductivity is found at 25 wt.%: 94% for 0 wt.% and 79% for 2 wt.%. For any SCMF concentration, thermal conductivity was found to be lower with the presence of nanotubes than without.

Comparison of thermal conductivity between short CMF and long CMF conditions, controlling for MWNT concentration, shows that trend wise that at 10 wt.%, thermal conductivity's are not different, but from 15 wt.% to 30 wt.%,

PBT-SCMF samples posses greater conductivity than long CMF samples. The difference between SCMF and LCMF increases with increasing CMF concentration. In general, samples with MWNTs tend to under-perform samples with not MWNT concentration.

For short CMF and long CMF composites at 0 wt.% MWNT concentration, it has been shown, and is theoretically consistent, that the tensile modulus and strengths are reduced in short CMF composites when compared to long CMF conditions [28, 107]. Structural reinforcement in highly aligned fibrous fillers requires long load-carrying paths for reinforcement (assuming high quality fiber surface finish, sufficient polymer-fiber adhesion, equal distribution of load within the fiber, ideal fiber morphology, etc.). Short paths results in more loading being carried in the matrix as well as more fiber-matrix-fiber load transitions. Furthermore, stress imbalance at the fiber tips, which is normally diminished over long fiber lengths, is more prominent in short CMF conditions. as well as stress imbalance near the fiber tips. Over longer lengths, this imbalance diminishes over the length of the fiber. For shorter fibers, this imbalance can play significant effects in the reinforcement of the composites. Similarly, for thermal properties, longer fibers reduces the number of polymer-fiber interface interference's that must be overcome, leading to improved thermal conduction. However, the effect of CMF length in the presence of MWNTs has not been previously studied. It is interesting that MWNT reinforcement actual increases stiffness when comparing short CMF to long CMF, and helps to reduce the difference in ultimate

tensile strength. However, it should also be noted that there is a significant re-

duction in ultimate tensile strength at 2 wt.% MWNT across all CMF loadings.

5.2.2 Straight/Divergent Die Comparison

(a) 10 wt.% CMF.

(b) 15 wt.% CMF.

(c) 20 wt.% CMF.

(d) 25 wt.% CMF.

(e) 30 wt.% CMF.
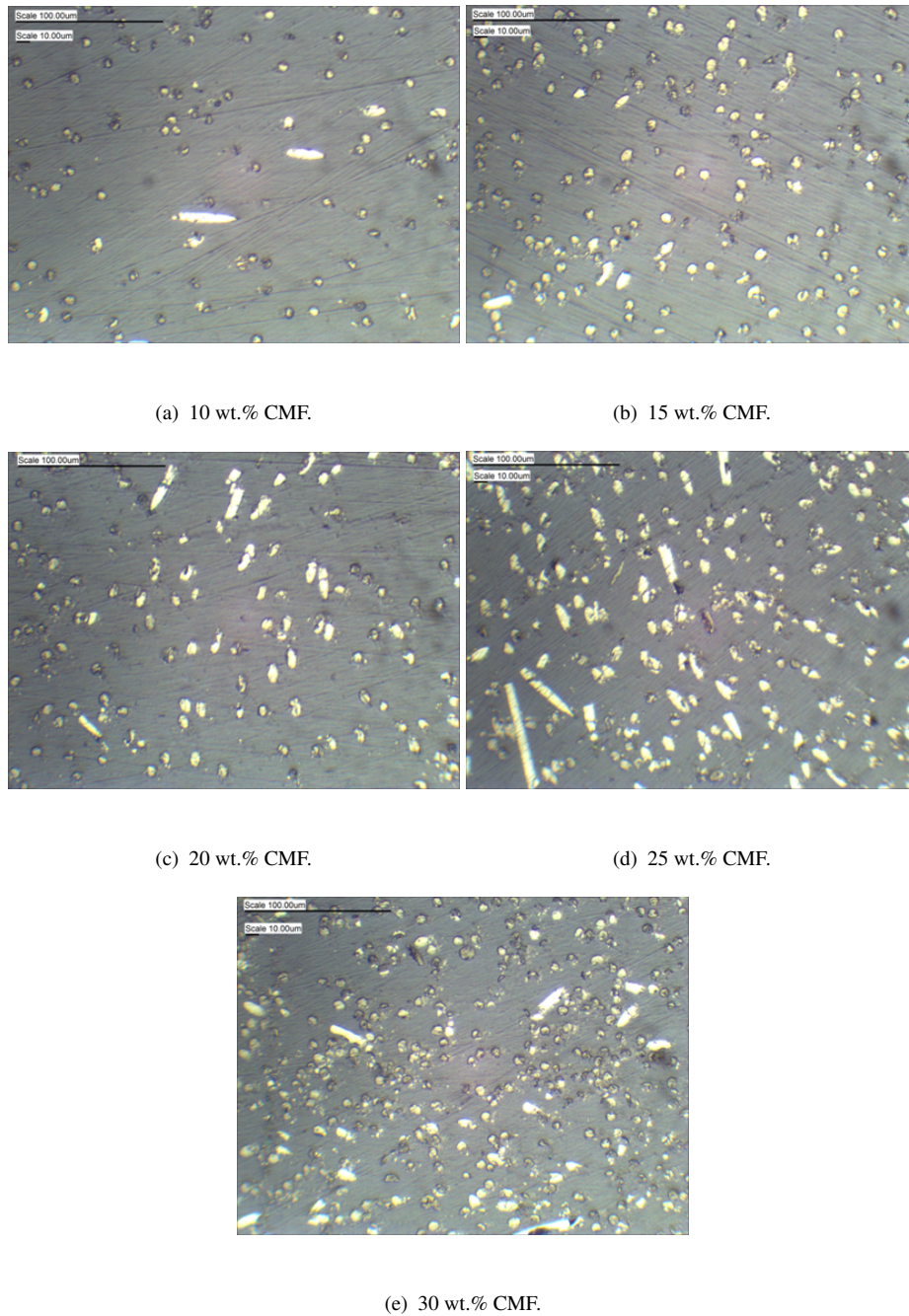
FIGURE 5.9: Short CMF characteristic micrographs ($\theta = 2.82°$).

In all micrographs, fiber reorientation from the extrusion orientation to some oblique alignment is evidenced by the ellipsoidal cross section of the fiber faces. While some property increase depreciation when switching from long CMFs to

short CMFs were seen in §5.2.1, the move from short to long CMFs was necessary in order to maximize the reorientability of CMFs, which was limited geometrically by CMF length and die height. However, as will be discussed in more detail later, these short CMF orientation demonstrates a banded structure in the sample, such, when examining the transverse cross section, the bottom third and top third of fibers tended towards a flow axis alignment while the middle third of fibers tended towards an oblique orientation. Furthermore, a source of variance which could not be accounted for were small amounts of drawing during sample collection which could effect the short fibers more dramatically than long fibers. Again, no apparent difference was observed between 0 wt.% MWNT and 2 wt.% MWNT concentrations. From these micrographs, it appears that the number of fibers oriented out of plane increases from 10 wt.% to 25 wt.% CMF. However, at 30 wt.% CMF, the number of reoriented fibers appears to decrease. This could be indicative of the onset of an interaction mechanism preventing fibers from freely reorienting.
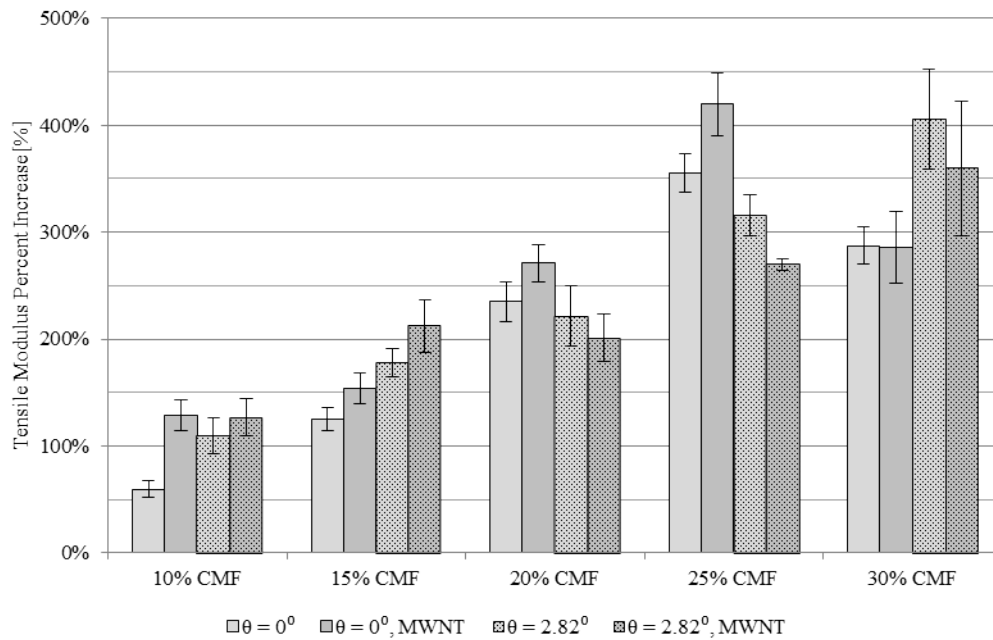
FIGURE 5.10: Comparison of tensile modulus percent increase at $\theta = 0°$ and $\theta = 2.82°$, compounded at 1.81 kg/hr and 200 rpm using 100 μm CMFs. Error bars represent one standard deviation of the measured data.

Tensile modulus at $\theta = 2.82°$, as graphed in Figure 5.10 with short CMF $\theta = 0°$, controlling for MWNT concentration, is approximately linear from 0 wt.% to 30 wt.% CMF ($R^2 = 0.926$ at 0 wt.% MWNTs and $R^2 = 0.797$ at 2 wt.% MWNTs). Across the CMF range, there is no statistically significant difference between tensile modulus with 0 wt.% MWNTs and 2 wt.% MWNTs. The maximum increase in tensile modulus was observed at 30 wt.% CMF of 410%. Interestingly, no loading limit between 25 wt.% and 30 wt.% CMF, as seen in §5.1 and §5.2.1, was observed for $\theta = 2.82°$ conditions. At concentrations at and below 20 wt.%, there is a small but statistically significant difference between the tensile modulus $\theta = 0°$ and $\theta = 2.82°$ conditions, without or with MWNTs. From 10 wt.% to 25 wt.% CMF, $\theta = 0°$ conditions still tend to have greater tensile modulus

than $\theta = 2.82°$ conditions. This result is consistent with the theory that fibers are being reoriented away from the extrusion axis (which is parallel to the axis of tensile loading), and that fibers which are oriented off the loading axis contribute less to the measured tensile modulus. At 30 wt.%, once the loading limit is reached, $\theta = 2.82°$ conditions dramatically out perform $\theta = 0°$ conditions, and nearly reach the maximum tensile modulus properties measured for $\theta = 0°$ conditions at 25 wt.% CMF.
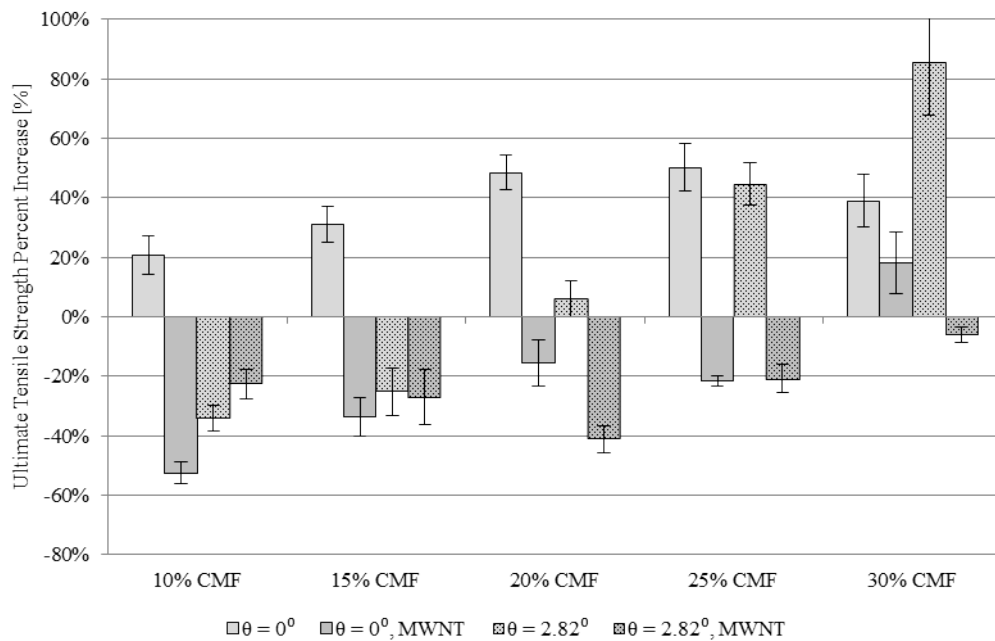
FIGURE 5.11: Comparison of ultimate tensile strength percent increase at $\theta = 0°$ and $\theta = 2.82°$, compounded at 1.81 kg/hr and 200 rpm using 100 μm CMFs. Error bars represent one standard deviation of the measured data.

The ultimate tensile strength of $\theta = 2.82°$, graphed against equivalent $\theta = 0°$ conditions, is presented in Figure 5.11. At $\theta = 2.82°$, ultimate tensile strength is shown to follow an linear trend from across CMF concentration for 0 wt.% MWNT. Ultimate tensile strength does not vary significantly across CMF concentration for 2 wt.% MWNT. At 0 wt.% MWNT, ultimate tensile strength is

adversely affected the diverging die at low CMF concentrations, but converges

linearly ($R^2 = 0.959$) to $\theta = 0°$ properties at higher CMF concentrations. For

2 wt.% MWNT conditions, little improvement in ultimate tensile strength was

observed for any CMF loading. This poor performance is attributed to both CMF

reorientation and the adverse effect of MWNTs on polymer matrix ultimate

tensile strength. Interestingly, the highest ultimate tensile strength occurs at

30 wt.% CMF for $\theta = 2.82°$, performing 30 wt.% better than 25 wt.% CMF for

$\theta = 0°$. Again, no loading limit is observed for ultimate tensile strength between

25 wt.% and 30 wt.% CMF. It is worth nothing that the degree of fiber reorien-

tation may not be consistent across specimens, thus the variation in $\theta = 2.82°$

conditions may in part be due to this variations in pumping and collection.
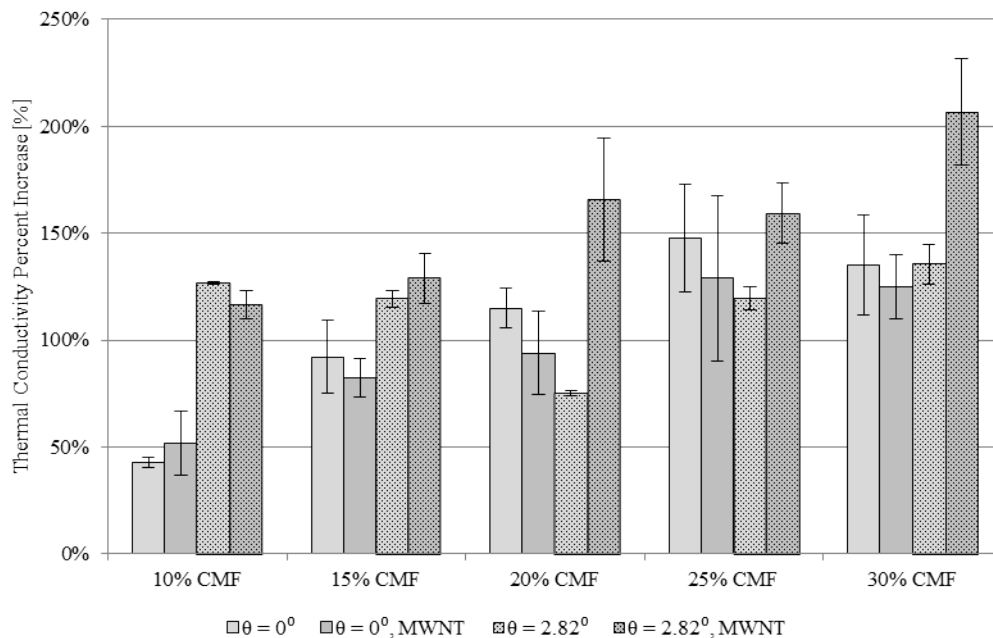
FIGURE 5.12: Comparison of thermal conductivity percent increase at $\theta = 0°$ and $\theta = 2.82°$, compounded at 1.81 kg/hr and 200 rpm using 100 μm CMFs. Error bars represent one standard deviation of the measured data.

Comparison between 0 wt.% and 2 wt.% MWNT shows that from 10 wt.% to

15 wt.% CMF, thermal conductivity is approximately equivalent between conditions. However, beyond 15 wt.% CMF, thermal conductivity of 0 wt.% MWNT thermal conductivity drops significantly while the thermal conductivity of 2 wt.% MWNT conditions continues to rise linearly ($R^2 = 0.945$). Unlike $\theta = 0°$ conditions,the presence of MWCNTs acts to improve thermal conductivity. In both MWCNT loading conditions, no loading limit is found between 25 wt.% and 30 wt.%. The largest increase in thermal conductivity of 121% is found at 30 wt.% and 2 wt.%. This serves to indicate that MWNT concentration is enhancing thermal conductivity by, in a rough analogue to CMF concentration, MWNT reorientation.

Comparison of $\theta = 0°$ and $\theta = 2.82°$ conditions indicates that tensile modulus is marginally diminished with increasing die angle. Ultimate tensile strength demonstrates different trends in the absence of presence of MWNTs. With 0 wt.% MWNT, ultimate tensile is decreased with increasing die angle at lower CMF concentrations, but come to near equality at higher CMF concentrators. At 2 wt.% MWNTs, ultimate tensile strength remains universally low and does not follow a clear trend. At 0 wt.% MWNT, thermal conductivity demonstrates a decreasing trend with increasing CMF concentration, and demonstrates an increasing trend with respect to CMF concentration at 2 wt.% MWNT. These trends indicate, and are verified by optical microscopy, that reorientation of CMFs acts to marginally decrease longitudinal tensile properties while increasing transverses thermal properties. This prompts a further study into the effects of flow rate and a further investigation of die angle on the properties of reoriented multiscale

composites, which is performed in the next section.

5.3 Parametric Study

A parametric study was conducted using three new die geometries across a range of flow rates, CMF concentrations, and MWNT concentrations. Statistical analysis was performed, including both new results as well as results from §5.2. This analysis generated statistical predictive models and highlighted significant trends between independent parameters and measured properties. A description of the linear regression analysis methodology is in §3.3.4.

Three new die angles are used: $\theta = 1.41°$ (B), $\theta = 2.26°$ (D), and $\theta = 4.52°$ (F). Results for $\theta = 0°$ (A) and $\theta = 2.82°$ (E) are included in statistical analysis. Again, five CMF concentrations, 10 wt.%, 15 wt.%, 20 wt.%, 25 wt.%, 30 wt.%. and two MWNT concentrations, 0 wt.% and 2 wt.%, were used. Three flow rates were used, 1.36 kg/hr, 1.81 kg/hr, and 2.26 kg/hr. This new parametric axis was introduced to examine the effect of varying shear rate on measured properties. Previously, results were obtained only using 1.81 kg/hr. Excluding previous results, this introduces 90 new conditions, for a total of 110 conditions including previous results. Screw speed and vacuum pressure were controlled at 200 rpm and 25 inHG. New results are tabulated in Table A.3 ($\theta = 1.41°$), Table A.4 ($\theta = 2.26°$), and Table A.6 ($\theta = 4.52°$).

5.3.1 Effect on Fiber Orientation

Qualitative analysis of did not yield significant insight into the relationship between CMF concentration, MWNT concentration, flow rate, and die angle or

any obvious interacting effects. Main effects, as well as individual interactions were examined using a multiple linear regression model. All interaction effects with the exception of CMF concentration with MWNT concentration $V_\mu V_n$ were found to be non-significant. Furthermore, a systematic study conducted including and not including flow rate indicated that flow rate plays no significant role in fiber orientation. The remaining multiple linear regression model is shown in Equation 5.1, and the coefficients and P-values of these parameters is tabulated in Table 5.1.

$$\hat{\alpha}\left(V_\mu, V_n, \theta\right) = \beta_0 + \beta_1 V_\mu + \beta_2 V_n + \beta_3 \theta + \beta_4 V_\mu V_n \qquad (5.1)$$

TABLE 5.1: Fiber orientation regression model parameters.

Effect	Coefficient	P-Value
Intercept	54.30	0.0000
V_μ	4.93E−5	0.9899
V_n	-0.8300	0.1573
θ	0.7334	0.0000
$V_\mu V_n$	0.0671	0.0165

The main effect of die angle θ and the interaction between CMF concentration and MWNT concentration were the only statistically significant effects identified. Both CMF and MWNT concentration were found to be conditional upon the interaction effect. The adjusted correlation coefficient of this data was be $R^2 = 0.3222$. This model is based on the average median fiber distribution of multiple images per condition, so additional power could be gained from including the median value of individual images. However, this introduces non-uniformity in the median variance at lower CMF concentrations because of the

relative sparsity of fibers per image when compared to the high CMF concentrations, where fibers are sufficiently densely packed to allow for more accurate measurement within a single image. Overall, the adjusted regression coefficient $R^2 = 0.3222$ indicates that the inferential model does not explain much of the fiber orientation variance. While the source of variance could lie in physical phenomenon, it more likely lies in the measurement of fiber analysis. The analysis of a two-dimensional micrograph does not yield significant information about the three-dimensional structure of a characteristic space.

5.3.2   Tensile Modulus

One statistically significant two-way interaction effect, MWNT concentration on flow rate ($P = 0.0002$), and one significant three way interaction effect, the effect of MWNT concentration on the CMF concentration and flow rate interaction ($P = 0.0047$), were found with an adjusted correlation coefficient of $R^2 = 0.670$. The regression model is defined in Equation 5.2 and Table 5.2.

$$
\begin{aligned}
\hat{E}\left(V_\mu, V_n, Q, \theta\right) = &\beta_0 + \beta_1 V_\mu + \beta_2 V_n + \beta_3 Q + \beta_4 \theta + \beta_5 V_\mu V_n \\
&+ \beta_6 V_\mu \theta + \beta_7 V_n \theta + \beta_8 V_n Q + \beta_9 V_\mu V_n \theta
\end{aligned}
\tag{5.2}
$$

TABLE 5.2: Tensile modulus regression model parameters.

Effect	Coefficients	P-value
Intercept	-0.3231	0.5463
V_μ	0.1118	0.0000
V_n	1.5367	0.0000
Q	0.1190	0.1939
θ	0.3472	0.0130
$V_\mu V_n$	-0.0520	0.0001
$V_\mu \theta$	-0.0150	0.0042
$V_n \theta$	-0.2842	0.0042
$V_n Q$	-0.2452	0.0002
$V_\mu V_n \theta$	0.0132	0.0047
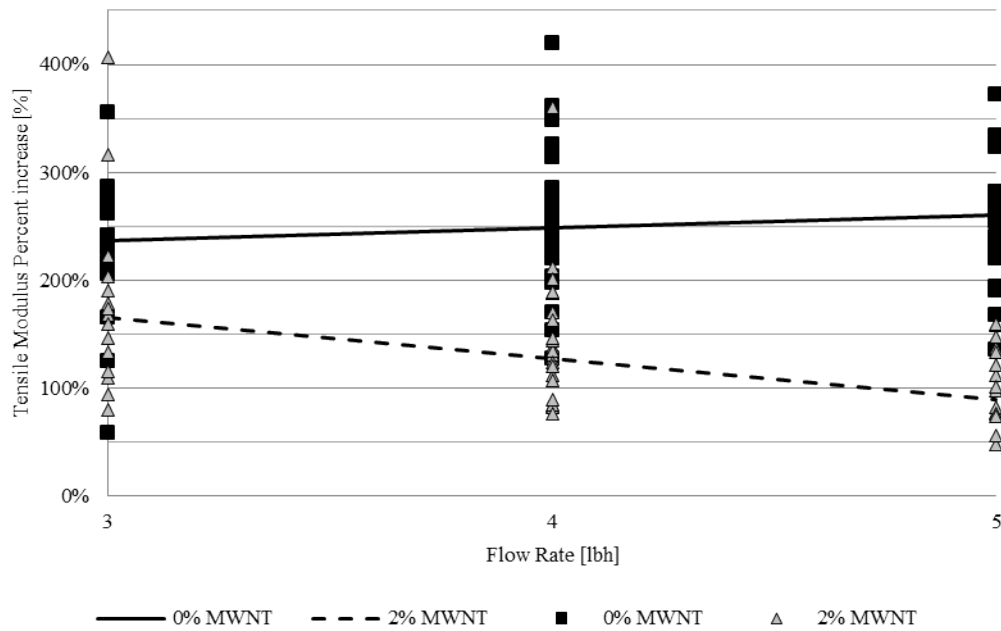
FIGURE 5.13: Predicted tensile modulus (line) using Equation 5.2 plotted against observed values (markers) demonstrating the two-way interaction between MWNT concentration and flow rate. Flow rate is controlled (1.81 kg/hr).

The effect of MWNT concentration with respect to flow rate, shown in Figure 5.13, on tensile modulus is complex. At 0 wt.% MWNT concentration, increasing flow rate acts to marginally increase composite stiffness. This appears to indicate that while the fibers are being reoriented out of plane with respect to

95

the load bearing direction, the effect is on stiffness is marginal. However in the presence of MWNTs, fibers are reoriented dramatically out of plane because of the increased shear rate from the presence of MWNTs, it appears that the fibers are oriented more out of plane, leading to reduced stiffness.

At 0 wt.% MWNTs, increasing die angle at low CMF concentrations ($V_\mu \leq 20$ wt.%) leads to an increase in tensile modulus with respect to die angle. At higher CMF concentration ($V_\mu \geq 25$ wt.%), increasing die angle leads to a decrease in tensile modulus. At all CMF concentrations , increasing CMF concentration leads to a greater tensile modulus at $\theta = 0°$. By visual inspection, while these trends are apparent, observed data is still very loosely distributed about the predicted trend. At 2 wt.% MWNT, the mean stiffness at $\theta = 0°$ is nearly 100% lower than with 0 wt.% MWNT. At 2 wt.% MWNT, CMF conditions which are increasing at 0 wt.% MWNT are now decreasing. Physically, this could be mechanistically attributed to, in the case of 2 wt.% MWNTs, the effect of CMF concentration overcomes the effect of CMF orientation (which is proportional to die angle), while at 0 wt.% MWNTs, the effect of CMFs concentration is overcome by the effect of CMF orientation.
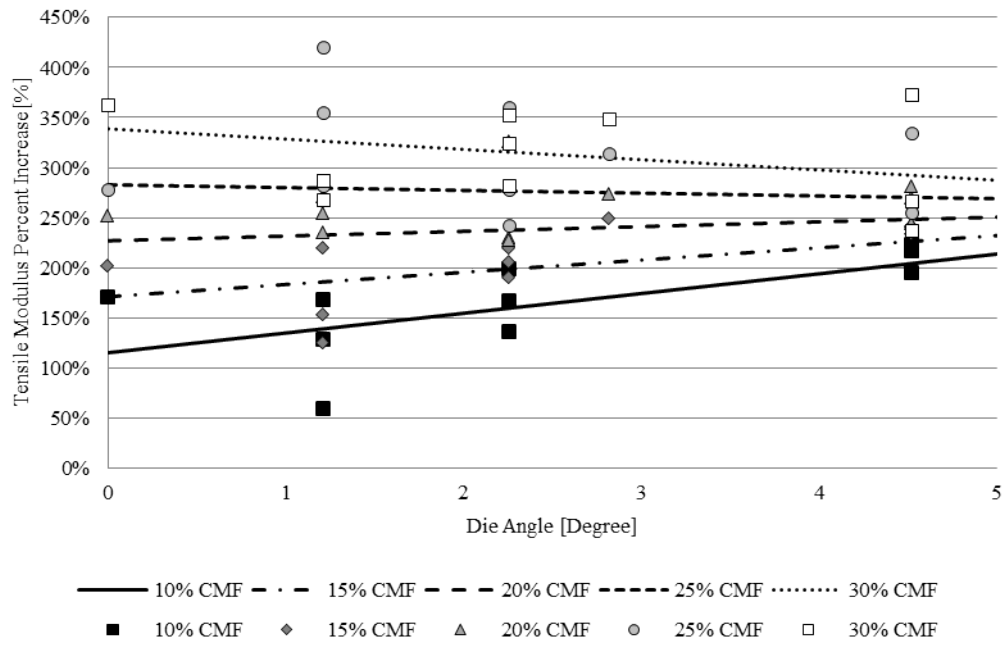
(a) MWNT Concentration: 0 wt.%.
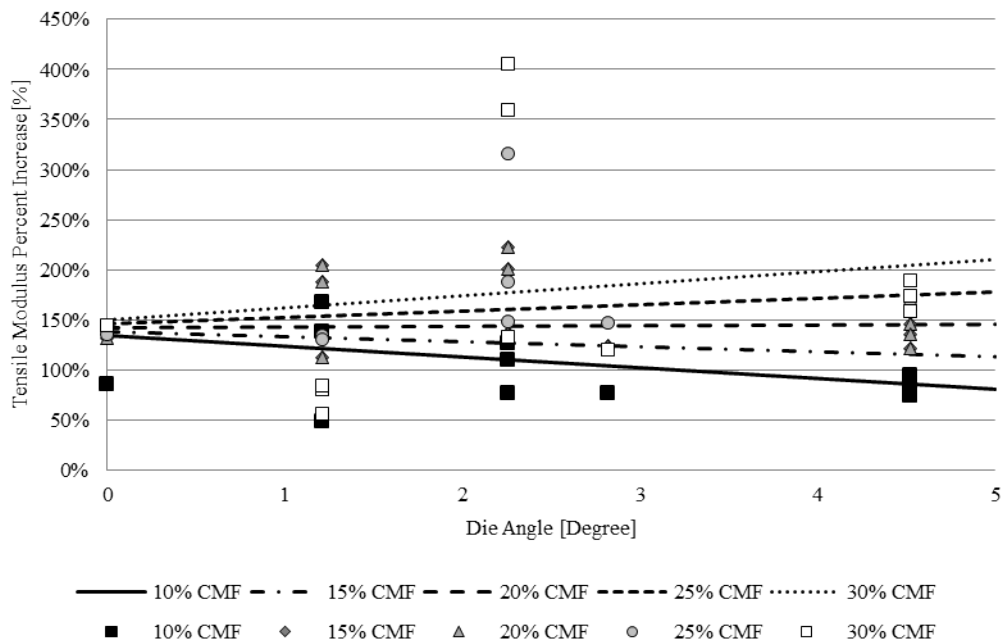
(b) MWNT Concentration: 2 wt.%.

FIGURE 5.14: Predicted tensile modulus (line) using Equation 5.2 plotted against observed values (markers) demonstrating the three-way interaction between CMF concentration, MWNT concentration, and die angle. Flow rate is controlled (1.81 kg/hr).

5.3.3 Ultimate Tensile Strength

One statistically significant two-way interaction effect between MWNT concentration and flow rate P = 0.0217, and one main effect of die angle P = 0.0000 were found for ultimate tensile strength. CMF concentration was not found to be statistically significant, but was found to be trending towards significant P = 0.0921. The regression model for ultimate tensile strength is defined in Equation 5.3 and Table 5.3. Note that the value of the intercept, i.e. the neat ultimate tensile strength percent increase, is approximately zero. This model has an adjusted correlation coefficient of $R^2 = 0.8632$, indicating that a significant amount of measured ultimate tensile strength variance is explained by the regression model. Remaining variance could be a result of processing variance and sample preparation before testing.

$$\hat{\sigma}_u\left(V_\mu, V_n, Q, \theta\right) = \beta_0 + \beta_1 V_\mu + \beta_2 V_n + \beta_3 Q + \beta_4 \theta + \beta_5 V_n Q \tag{5.3}$$

TABLE 5.3: Ultimate tensile strength regression model parameters.

Effect	Coefficients	P-value
Intercept	-0.0052	0.2241
V_μ	0.0105	0.0921
V_n	-0.2151	0.4121
Q	-0.0609	0.0113
θ	-0.0807	0.0000
QV_n	-0.0072	0.0217

The only statistically main effect, die angle, is plotted in Figure 5.15. Physically, increasing die angle θ leads to increased fiber angle ξ within the central third of the extruded sample, which is the segment that thermal and tensile testing was

98

performed on. As fiber angle increases, these obliquely aligned contribute less to the ultimate tensile strength of the composite. This is true in the absence and presence of MWNTs. However, the presence of MWNTs acts to weaken the polymer matrix. This is evidenced by the relatively bi-modal distribution of ultimate tensile strength based on the presence or absence of MWNTs, which is shown in Figure 5.16.
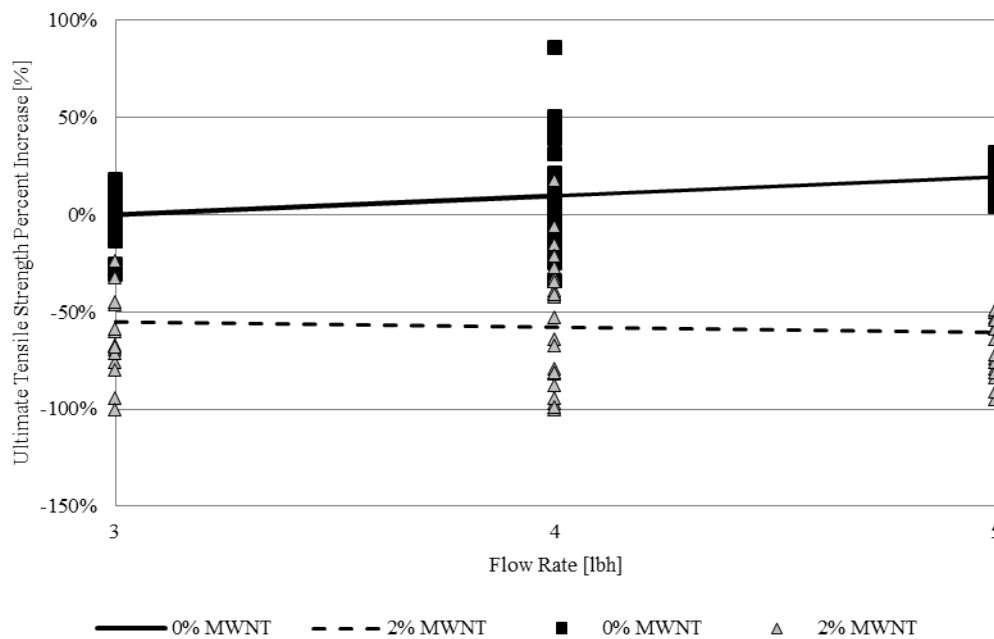
FIGURE 5.15: Predicted ultimate tensile strength (line) using Equation 5.3 plotted against observed values (markers) demonstrating the main effect of CMF concentration. CMF concentration (20 wt.%) and flow rate (1.81 kg/hr) are controlled. Note the bi-modal effect of MWNT concentration on ultimate tensile strength.

The result of MWNT concentration on flow rate is shown in Figure 5.16. In the absence of MWNTs, increasing flow rate leads to up to a 25% increase in ultimate strength at 2.27 kg/hr from 1.36 kg/hr. However, 2 wt.% MWNTs, the origin of the predicted ultimate tensile strength reduced by approximately 40% from 0 wt.% MWNT as well as demonstrates a decreasing trend with respect

to increasing flow rate rather than an increasing trend as is for 0 wt.% MWNT.
This is a likely indication, fibers are taken more out of plane with increasing
flow rate in at 2 wt.% MWNT. This result follows closely with the results shown
in Figure 5.13 for tensile modulus. This is highly evidenced by the nearly bi-
modal distribution of measured ultimate strength in Figure 5.16. This a result of
the weakening of the polymer matrix by the inclusion of MWNTs.
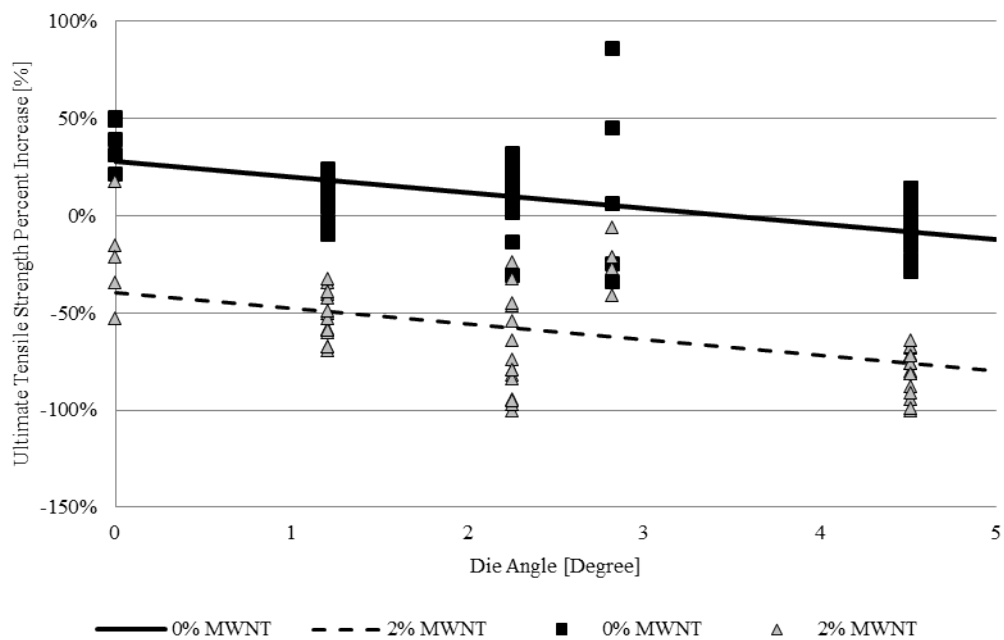
FIGURE 5.16: Predicted ultimate tensile strength (line) using Equation 5.3
plotted against observed values (markers) demonstrating the two way interac-
tion effect between MWNT concentration and flow rate. CMF concentration
(20 wt.%) is controlled.

5.3.4   Thermal Conductivity

One statistically significant main effect, CMF concentration (P = 0.0000), and
one three way interaction effect, the effect of MWNT concentration on the in-
teraction between flow rate and die angle (P = 0.0120), were found with an

adjusted correlation coefficient of $R^2 = 0.834$. The remaining three indepen-dent independent parameters and three interaction effects were marginal. The regression model, including statistically significant effects and marginal effects, is defined in Equation 5.4.

$$
\begin{aligned}
\hat{k}\left(V_\mu, V_n, Q, \theta\right) =& \beta_0 + \beta_1 V_\mu + \beta_2 V_n + \beta_3 Q + \beta_4 \theta + \beta_5 V_n Q \\
& + \beta_6 V_n \theta + \beta_7 Q \theta + \beta_8 V_n Q \theta
\end{aligned}
\tag{5.4}
$$

TABLE 5.4: Thermal conductivity regression model parameters.

| Effect	Coefficient	P-value
Intercept	0.7800	0.0078
V_μ	0.0388	0.0000
V_f	-0.3761	0.0632
Q	-0.0785	0.2635
θ	-0.3710	0.0002
$V_n Q$	0.0845	0.0899
$V_n \theta$	0.2673	0.0001
$Q\theta$	0.0829	0.0006
$V_n Q \theta$	-0.0421	0.0120
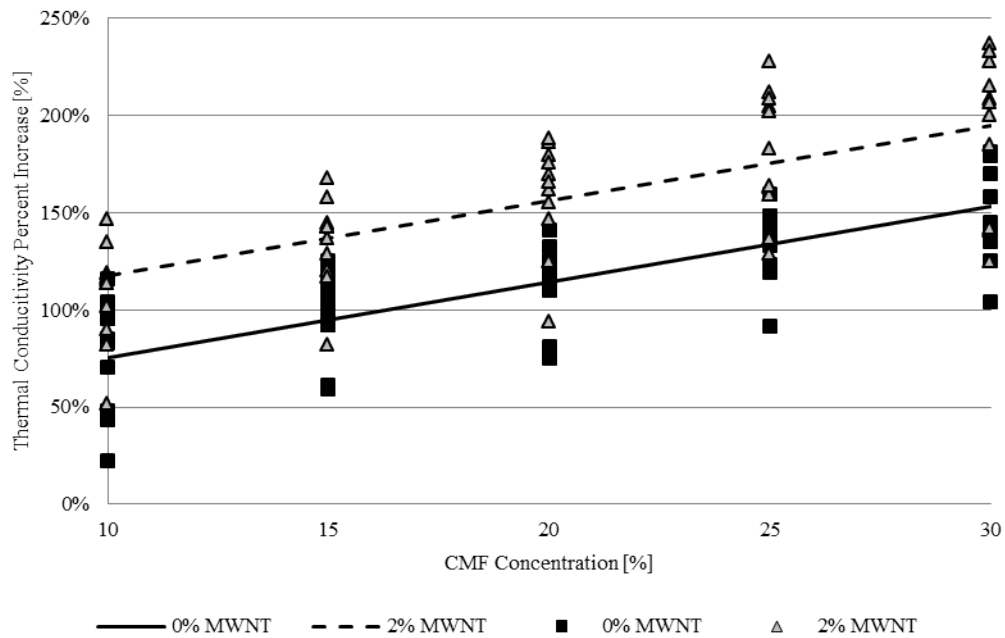
FIGURE 5.17: Predicted thermal conductivity (line) using Equation 5.4 plotted against observed values (markers) demonstrating the interaction between CMF concentration and MWNT concentration. Flow rate (1.81 kg/hr) and die angle (2.25°) are controlled.

Physically, the action of CMF concentration is clear. As CMF concentration is increased, there are more fibers available to transfer heat. However, while not indicated as statistically significant, there is a clear effect of MWNT concentration on thermal conductivity. At 2 wt.% MWNTs, there is up to an 50% increase in thermal conductivity while controlling for all other parameters. This indicates that either the CMFs have been reoriented to a more favorable orientation, or that the MWNTs, or morphological changes brought on by the presence of MWNTs, are now carrying a portion of the heat load. While not examined, it is likely that MWNTs orientation is also effected during flow, and by the equations given by Vincent and Agassant [86], MWNTs should be much more effected than the

CMFs due to aspect ratio. It is likely that this is the source of thermal conduc-

tivity between 0 wt.% MWNT and 2 wt.% MWNT concentration.
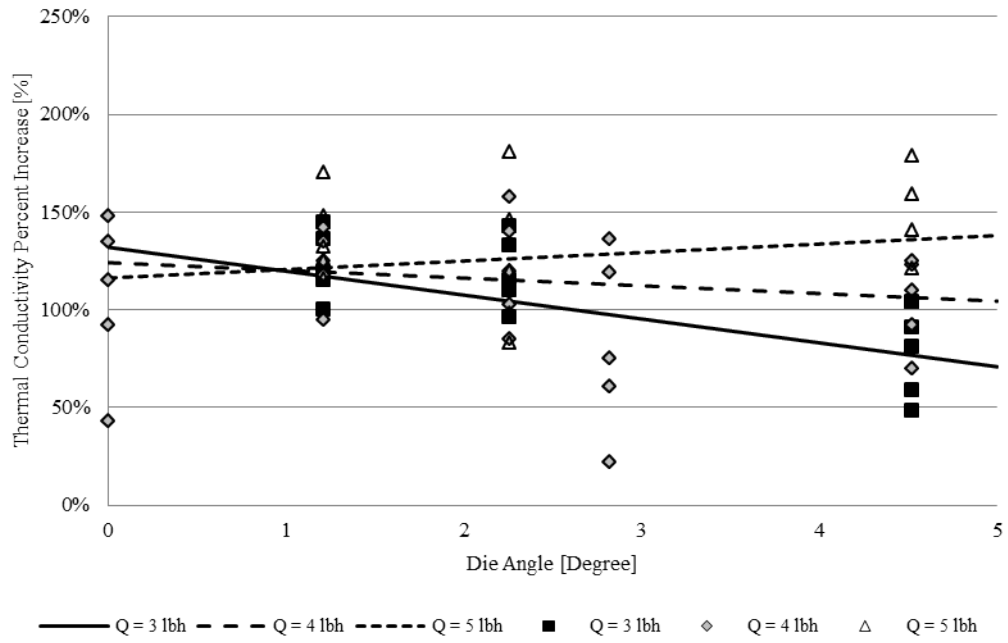
(a) MWNT Concentration: 0 wt.%.
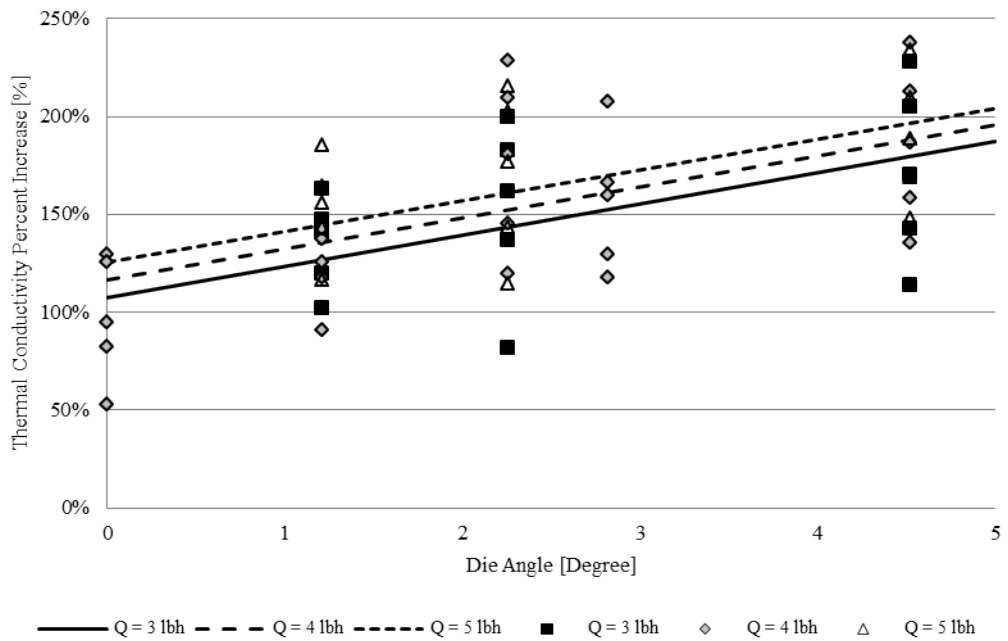
(b) MWNT Concentration: 2 wt.%.

FIGURE 5.18: Predicted thermal conductivity (line), using Equation 5.4, plotted against observed values (markers) demonstrating the three-way interaction effect of MWNT concentration, flow rate, and die angle. CMF concentration (20 wt.%) is controlled. Comparison of Figure 5.18(b) (0 wt.% MWNT) and Figure 5.18(a) (2 wt.% MWNT) indicate that MWNT concentration changes the interaction between flow rate and die angle.

The differing interaction between flow rate and die angle as a function of MWNT concentration shown in Figure 5.18 could be the result of two potential mechanisms. In the absence of MWNTs, increasing flow rate improves thermal conductivity increase, such that increasing die angle at 2.27 kg/hr increases thermal conductivity, but increasing die angle decreases thermal conductivity at 1.36 kg/hr and 1.81 kg/hr. However, in the presence of MWNTs, all three flow rates demonstrate increasing thermal conductivity with increasing die angle. First, it is possible that MWNTs themselves are carrying a portion of the thermal load. Second, it is possible that the MWNTs influence the matrix rheology and therefore the flow of CMFs in the die as well as assisting to damp out secondary flows which act to reorient fibers during collection. In the absence of MWNTs, it is likely that the increasing flow rate, while decreasing the die residence time, (see §3.2.1.1, Pg. 31), increases the magnitude of velocity gradients acting on the fibers.

5.3.5 Rheological Argument

The effect of MWNT concentration on thermal conductivity, or more loosely to tensile modulus or ultimate tensile strength, can be attributed to several mechanisms. First, the presence of MWNT concentration increases the apparent viscosity of the melt. Second, by this increased viscosity, fiber damage during processing is more likely, which in turn results in shorter fibers which may be easier to reorient, or alternatively more difficult to orient from the random state in the die zone. However, this would be balanced by reduced carrying capacity

of the fibers due to lower fiber lengths. Third, CNTs alter the matrix morphology, leading to increased conductivity through the matrix.

A number of authors have conducted rheological and dynamic mechanical properties of nanocomposites. Valendtino et al. [108] examined viscosity, loss modulus, and the loss tangent as a function of MWNT concentration in LDPE and HDPE up to 5 wt.% MWNTs. They found that the viscosity of neat HDPE was on the order of $5 \cdot 10^3$ Pa·s at low frequencies and demonstrated shear thinning behavior starting at 10 rad/s. At 0.5 wt.% and 1.0 wt.% MWNTs, little difference in viscosity was observed except for a slight increase. However, at 2.5 wt.% MWNTs, a significant increase in viscosity, almost one and a half orders of magnitude at low frequencies, as well as a change in the shear thinning behavior over the full range of frequencies was observed. At frequencies above 100 rad/s, the viscosity's of neat and loaded melts were observed to converge. Yet more increase in viscosity and change in shear thinning behavior were observed at 5.0 wt.%. For reference, these composites were prepared by micro-twin-screw-extrusion. Potschke et al. [109] also observed similar increased in viscosity as well as the MWCNT dependence of viscosity increase. Ahmad et al. [110] investigated the effect of surface treatment on viscosity increase and found that pristine CNTs demonstrated the greatest viscosity, which treated CNTs still demonstrated viscosity increase over neat polymer, but not as much as pristine CNTs.

Valendtino et al. and Potschke et al. [111] theorized that, because of the approximately comparable length scale between polymer chains and MWNTs, the

network of polymer chains interacts with that of the MWNT network (or partial networks), leading to increased viscosity. Potschke et al. also observed an onset in dramatically increased rheological properties at some certain threshold MWNT concentration, which was identified as the 'percolation threshold concentration,' at which extensive MWNT networks formed. This relationship was found to be strongly related to temperature, as Potschke et al. observed the onset of percolation at 5.0 wt.% at 170°C and 0.5 wt.% at 280°C, which they theorized related to the network density as a function of temperature during compounding. McNally et al. [112] explored similar structures in PE and found that the percolation onset was much higher, at 7.5 wt.%. McNally et al. identified three mechanisms for this increase: (1) PE coats the MWNTs, this reducing the effectiveness of electrical transmission; (2) twin screw extrusion may improve the coating of MWNTs over other preparation tools; and (3) the geometry of the extruder die induces alignment of the MWNTs during extrusion, thus reducing the number of contact points. Extending this rationale, it is possible that the flow induced orientation produces an anisotropically percolated networks. This could support the thermal conductivity results in §5.3.6 when comparing straight die to increasing divergences with and without MWNTs.

As stated previously, the effect of MWNT concentration on viscosity could lead to several effects during pumping through a die. First, because the viscosity is increased and the shear thinning profile is changed, the apparent viscosity in the melt is likely to be increased. This would could lead to a reduction in the reorientability of the fibers during extrusion. However, the theory presented by

[Vincent and Agassant](#) would seem to imply that this is not the case. From observation during extrusion, it is clear that the melt is more viscous during extrusion, and therefore more resistant to minute reorientation's induced by pulling on the extrudate after pumping through the die. By this mechanism, reorientation that occurred during extrusion would be less likely to be undone during collection than extrudate without MWNTs. However, by the same mechanism, the fibers would likely be more difficult to reorient during extrusion.

Finally, during compounding, the amount of stress encountered in the extruder is related to the shear rate and the viscosity of the melt. By changing the apparent viscosity of the melt by the inclusion of MWNTs (given that during compounding any flow induced alignment would be constantly agitated by the mixing section), it is possible that the fibers fracture during mixing, leading to a reduced aspect ratio.

5.3.6 Summary of Statistical Analysis

Multiple regression analysis was conducted on measured fiber orientation $\hat{\xi}$, mean tensile modulus $\hat{E}$, mean ultimate tensile strength $\hat{\sigma}_u$, and mean thermal conductivity $\hat{K}_e$ of composite samples produced using die angles of $\theta = 0°$ (A), $\theta = 1.21°$ (B), $\theta = 2.26°$ (D), $\theta = 2.82°$ (E), and $\theta = 4.52°$ (F). Four independent input variables were used, CMF concentration V_μ, MWNT concentration V_n, flow rate Q, and die angle θ. In §[5.3](#), regression models were generated,

and statistically significant effects and interactions were discussed. In this section, the statistically significant main and interactions effects for tensile modulus, Equation 5.5, ultimate tensile strength, Equation 5.6, thermal conductivity, Equation 5.7, and are summarized.

$$\hat{E} = \beta_8 V_n Q + \beta_9 V_\mu V_n \theta + \hat{E}_{marginal} \tag{5.5}$$

$$\hat{\sigma}_u = \beta_4 \theta + \beta_5 V_n Q + \hat{\sigma}_{u,marginal} \tag{5.6}$$

$$\hat{k} = \beta_1 V_\mu + \beta_8 V_n Q \theta + \hat{k}_{marginal} \tag{5.7}$$

Two interactions were observed for tensile modulus. Without MWNTs, increasing flow rate has little effect on stiffness, with a mean tensile modulus increase of approximately 250% controlling for all other parameters. However, with MWNTs, controlling for all parameters, stiffness is reduced from 50% up to 100% as compared to no MWNTs and demonstrates a decreasing trend with increasing flow rate. This is indicative of increase fiber reorientation in the presence of MWNTs with increasing flow rate. The second interaction, the relationship of MWNT concentration on the interaction between die angle and CMF concentration is complex. In the absence of MWNTs, increasing die angle at low CMF concentrations ($V_\mu \leq 20$ wt.%) leads to an increase in tensile modulus with respect to die angle, while the inverse is true at higher CMF concentrations. At 2 wt.% MWNT, the inverse of 0 wt.% MWNT trends are true. This behavior is likely due to the effect of fiber-fiber interaction on reorientation as die angle increases.

Increasing die angle leads to an decreased ultimate tensile strength. This is consistent with fibers being reoriented more out of plane as fiber angle increases due to a greater die angle, leading to less CMFs contributing to the strength of the composite. MWNTs significantly reduce the overall strength of the composite. At 0 wt.% MWNT concentration, increasing flow rate marginally increases ultimate tensile strength. At 2 wt.% MWNT, increasing flow rate decreases ultimate tensile strength. This is again consisted with the theory, in the presence of MWNTs, increasing flow rate takes more fibers out of plane, leading to reduced ultimate tensile strength.

For thermal conductivity, two significant effects were observed. First, TC increases with increase CMF concentration. Furthermore, the presence of MWNTs acts to increase thermal conductivity nearly 50% more than without. The second effect is the differing interaction between flow rate and die angle as a function of MWNT concentration. In the absence of MWNTs, increasing flow rate improves thermal conductivity increase, such that increasing die angle at 5 lb/hr increases thermal conductivity, but increasing die angle decreases thermal conductivity at 3 lb/hr and 4 lb/hr. However, in the presence of MWNTs, all three flow rates demonstrate increasing thermal conductivity with increasing die angle. These effects in composite appear to indicate that MWNTs again improve the reorientation of CMFs which may be related to the increase in apparent viscosity of the melt, leading to improved transverse thermal conductivity, and that MWNTs may be acting to improve the matrix thermal conductivity as well.

Chapter 6

Predictive Model

6.1 Background

The prediction of thermal conductivity in composite materials is a complex subject. A review of the fundamental prediction models is provided by Progelhof et al. [113], Tavman and Akinci [114], Shen et al. [115], and tangentially by Zimmer et al. [116]. An ideal model must incorporate discrete phase morphology, discrete phase structure embedded in the continuous phase, local and global distributions of the discrete phase, and discrete phase volumetric fraction for number of distinct discrete phases. Examining each of these characteristics more closely allows us to examine the parametric space that is necessary to cover for these models.

Discrete phase morphology presents a difficult challenge in that 0-D phases (i.e. powders), 1-D phases (i.e. fibers), and higher dimensional discrete phases (i.e.

sheets, weaves, etc.) each interact differently within the continuous phase as well as with each other. Furthermore, the scale of the filler can introduce additional interactions. For example, MWNTs have proven to be very useful for creating electrically conductive networks without a polymer due to the higher number of connections in a well dispersed composite, whereas CMFs have been shown to be better for mechanical enhancement due to their load bearing capacity.

The structure of the discrete phase or phases also plays a significant role in property enhancement. Uniaxially aligned cylindrical fillers have been shown to produce great enhancement in the longitudinal direction, but little to negative enhancement in the transverse orientation. Likewise, thermal conductivity was found to be enhanced, but electrical conductivity was not found to significantly improve due to few interconnects within the discrete phase. Discrete phase structure has been found to be more dominant in erode-able 0-D materials as well as 1-D and greater materials. Furthermore, with even 1-D structures, uni-axially aligned, planar-aligned, and randomly aligned structures are possible, each with different property anisotropy in different orientations.

In the following sections, a review of well-known and seminal predictive models will be discussed beginning with the rule of mixtures and leading into more commonly used models like the Lewis-Nielsen and Halpin-Tsai models. Each of these models, a two phase system is considered with matrix conductivity K_m and filler conductivity K_f. The ratio of K_f to K_m is denoted as K_r. At the end of this section, a review of the asymptotic behavior will be discussed.

6.1.1   Rule of Mixtures

The parallel model and series models (also known as the rule-of-mixtures and the inverse rule-of-mixtures respectively) describes the transference of a heat in layers parallel and in series to heat flow. These models give the effective upper (parallel) and lower (series) bounds of the effective thermal conductivity K_e. For an N-phase system, the general effective thermal conductivity equation is given by the following equation:

$$K_e^n = \sum_{i=1}^{N} k_i^n V_i \tag{6.1}$$

where $n = 1$ produces the parallel conduction model and $n = -1$ produces the serial conduction model. The geometric mean model effective thermal conductivity is given by:

$$K_e = \prod_{i=1}^{N} k_i^{V_i} \tag{6.2}$$

6.1.2   Halpin-Tsai Model

The Halpin-Tsai model, presented in Halpin and Kardos [117], utilizes an analogy between in plane heat flow (defined in Equation 6.1) where $n = 1$ and boundary conditions to the transverse transport of heat. The Halpin-Tsai model assumes fibers of uniform cross section arranged in parallel. The effective transverse heat flow coefficient is given by:

$$K_e = K_m \left[\frac{1 + \zeta \eta V_f}{1 - \eta V_f} \right] \qquad \eta = \frac{K_r + 1}{K_r - \zeta} \qquad \zeta = 1 \tag{6.3}$$

The geometry reinforcement parameter ζ varies according to filler morphology and structure. The Halpin-Tsai model can also be applied to properties other than thermal conductivity, for which other values of ζ are appropriate. A value of $\zeta = 1$ was chosen because of the analogous relationship between transverse thermal conductivity and longitudinal shear modulus and because of an assumed circular fiber cross section. Alternative choices of the geometry reinforcement parameter can be found in Halpin and Kardos [117]. Aside from the geometry reinforcement parameter, The Halpin-Tsai model is a function of only the matrix conductivity K_m, filler conductivity K_f, and matrix volume fraction V_f.

6.1.3 Nielsen Model

The Lewis-Nielsen model, [118, 119, 120], is a modification of the Halpin-Tsai model (see §6.1.2) to incorporate to filler shape and structure (i.e. orientation).

$$k_c = K_m \left(\frac{1 + ABV_{max}}{1 - B\psi V_{max}} \right) \tag{6.4}$$

$$B = \frac{K_r - 1}{K_r + A} \qquad \psi = 1 + V_f \left(\frac{1 - V_{max}}{V_{max}^2} \right)$$

where $A = K_e - 1$, K_e is the Einstein coefficient, and V_{max} is the maximum packing factor. A list of Einstein coefficients is list in Table 6.2, and a list of maximum packing fractions is tabulated in Table 6.1. The maximum packing fraction was determined from the geometric solution to a packing problem. For

the Lewis-Nielsen model, the packing fraction limit is explicitly defined, V_f :

$0 \leq V_f \leq V_{max}$.

It is clear that the Nielsen model incorporates many of the parameters one would wish to see in a predictive model (maximum packing, filler morphology, filler structure, etc.), it has been shown in some studies to accurately predict thermal conductivity [94, 106, 115] and in others to under predict thermal conductivity [59, 121]. In studies that matched well, divergence was still found at relative higher loadings.

TABLE 6.1: Lewis-Nielsen model values for V_{max}.

Shape	Type of packing	V_{max}
Spheres	Hexagonal close	0.7405
Spheres	Face centered cubic	0.7045
Spheres	Body centered cubic	0.6000
Spheres	Simple cubic	0.5240
Spheres	Random close	0.6370
Spheres	Random loose	0.6010
Fibers	Uniaxial hexagonal close	0.9070
Fibers	Uniaxial simple cubic	0.7850
Fibers	Uniaxial random	0.8200
Fibers	Three-dimensional random	0.5200

TABLE 6.2: Lewis-Nielsen model values for A.

Shape	Heat Flow	A
Cubes	Any	2.00
Spheres	Any	1.50
Spherical aggregates	Any	-
Random rods ($A_r = 2$)	Any	1.58
Random rods ($A_r = 4$)	Any	2.08
Random rods ($A_r = 6$)	Any	2.80
Random rods ($A_r = 10$)	Any	4.93
Random rods ($A_r = 15$)	Any	8.38
Uniaxial fibers	Parallel	$2A_r$
Uniaxial fibers	Perpendicular	0.5

6.1.4 Cheng-Vachon Model

The model proposed by Cheng and Vachon [122] is probabilistic approximation of a discontinuous phase in a unit cell. This model was developed for particle-filled and fiber-filled composites, but is insensitive to the morphology and structure of the filler. The transverse conductivity of the composite is given by:

$$\frac{1}{K_e} = \frac{1}{\sqrt{ACD^2}} \ln \left(\frac{D + E}{D - E} \right) + \frac{1 - B}{K_m} \qquad (6.5)$$

$$A = K_m - K_f \qquad B = \sqrt{\frac{3V_f}{2}} \qquad C = -4\sqrt{\frac{2}{3V_f}}$$

$$D = \sqrt{K_m - AB} \qquad E = \frac{B\sqrt{AC}}{2}$$

Note that this model is only valid from $V_f \leq 66.6$ vol.%. When $K_r > 100$, the effective thermal conductivity can be approximated by the second term of Equation 6.5; that is $K_e \approx K_m / (1 - B)$.

6.1.5   Agari-Uno

Agari and Uno [123] derived a semi-empirical model based on the generalization of parallel and serial conduction mechanisms (see Equation 6.1) which capture the effects of filler-filler contact and the fillers effect on the matrix state.

$$\ln (K_e) = V_f C_f \ln (K_f) + (1 - V_f) \ln (C_m K_m) \qquad (6.6)$$

C_m and C_f are experimentally determined constants of order unity. C_m is a measure of the effect of the filler on the morphology of the polymer (i.e. increased crystallinity, crystal size, thermal interference, etc.). Values of $C_m \approx 1$ indicate that the matrix is not significantly effected by the fillers, which is the case of CMFs. C_f measures the ease of the filler to form conductive networks.

6.1.6   Filler Limitations

All predictive models, with the exception of the rule of mixtures, asymptotically convergences to a constant effective thermal conductivity as the ratio of the filler thermal conductivity to the matrix thermal conductivity is $K_r > 50$. Figure 6.1 plots the behavior some of the models listed above at a 20 vol.% CMF and . It should be noted that the convergence behavior to the asymptote varies for

each model. Furthermore, the asymptotic value of thermal conductivity varies greatly, ranging from $K_e = 1.25K_m$ up to nearly $K_e = 3.65K_m$. Physically, this limitation arises from heat transfer capacity of the matrix. Regardless of the fiber heat conduction, the interference between the matrix and fiber, as well as the neat conductivity of the matrix, becomes the limiting factor in heat transfer. This demonstrates the need for an improved matrix material, given that the fiber conductivity is somewhat arbitrary beyond $K_r > 50$.
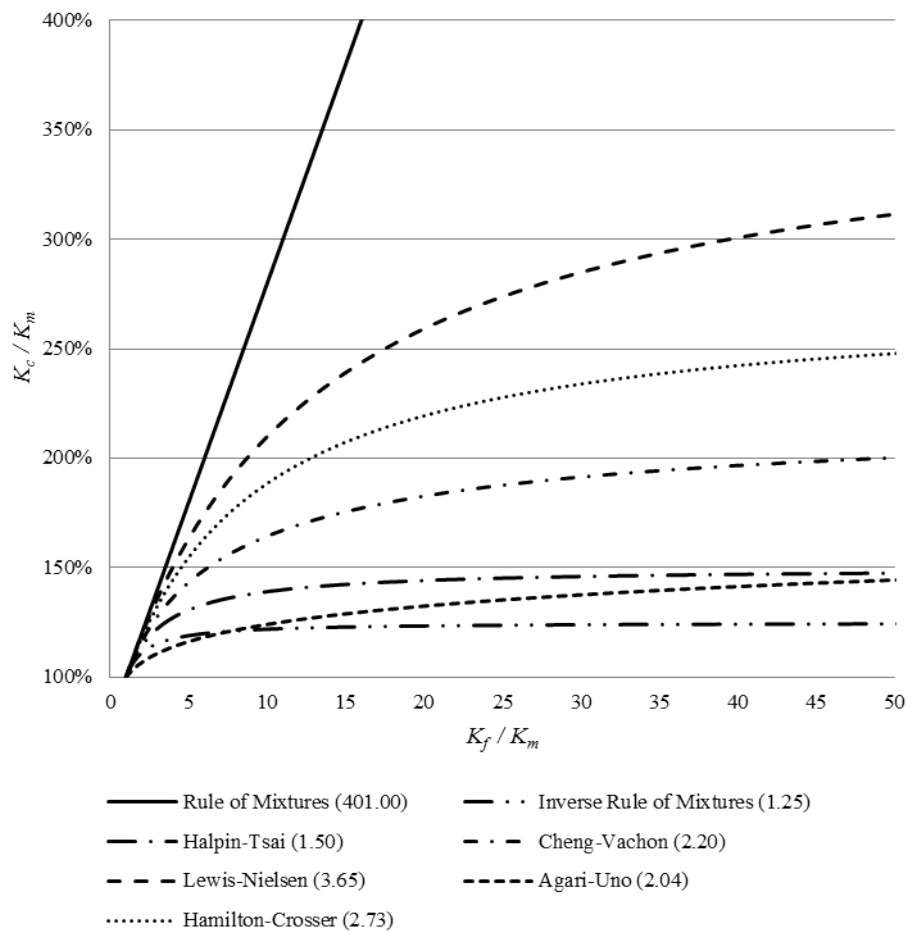
FIGURE 6.1: A selection of the predictive models listed in §6.1 are plotted against the filler/matrix thermal conductivity ratio at a fixed volumetric concentration of 20 vol.% CMF. With the exception of the rule of mixtures, all models converge to some asymptotic value of effective thermal conductivity around approximately $K_r = 50$. The ratio of effective conductivity to matrix conductivity (K_e/K_m) for $K_r = 2000$ is listed beside the model name in the plot legend.

6.2 Proposed Model

The newly developed model combines fiber orientation predictions made by Vincent and Agassant [86] with the semi-empirical predictive model proposed by Agari and Uno [123]. A thorough discussion of those equations is performed in §4.1 and §6.1.5. A brief summary of the relevant formulas from Vincent and Agassant's work are presented in this section, followed by new contributions combining these works and fitting them to experimental data from §5.3.

The Agari-Uno model well captures the physical effects of MWNT and CMF concentration rather than probabilistic models which tend to average out the effect of fillers into a continuum approximation and do not accurately capture fiber orientation. However, by introducing the Agassant and Vincent fiber orientation model, we gain a more accurate representation of the effects of CMF orientation on effective CMF thermal conductivity and the effects of MWNT concentration on the effective thermal conductivity which is not seen in previously discussed models.

An illustration of the die flow system is shown in Figure 6.2.

The shear rate $\dot{\gamma}$ and extensional rate $\dot{\alpha}$ are defined by Equation 6.7.

$$\dot{\gamma} = -\frac{A\left(\cos\left(2\beta\right) + \sin\left(2\theta\right)\right)}{\rho^2} \qquad \dot{\alpha} = -\frac{A\sin\left(2\beta\right)}{\rho^2} \tag{6.7}$$

$$A = \frac{Q}{h\left(\sin\left(2\theta\right) - 2\theta\cos\left(2\theta\right)\right)}$$
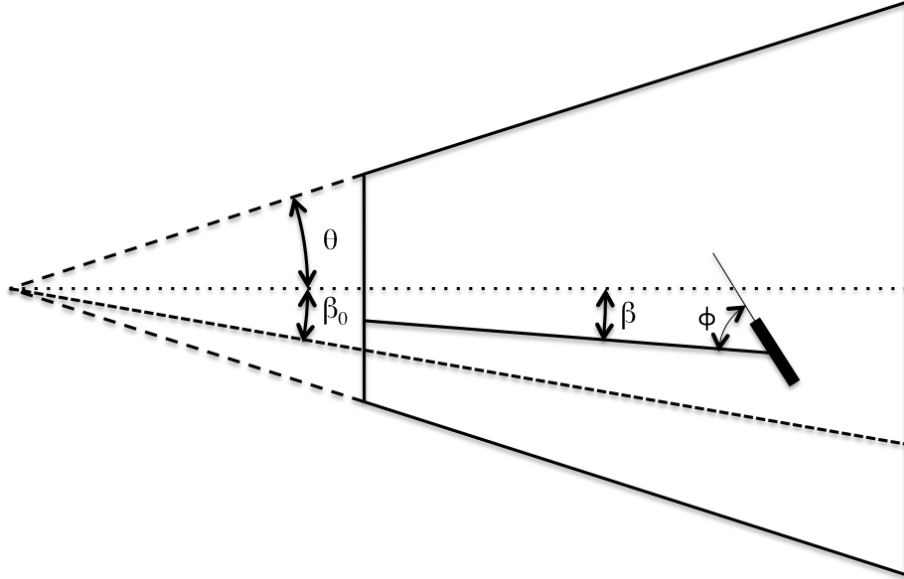
FIGURE 6.2: Illustration the die and relevant angles for the Vincent and Agas-
sant die flow.

The time rate of change of the fiber angle is defined as:

$$\frac{d\phi}{dt} = r\left(\dot{\alpha}\sin\left(2\phi\right) + \dot{\gamma}\cos\left(2\phi\right)\right) + \dot{\gamma} \tag{6.8}$$

$$r = \frac{l_f^2 - r_f^2}{l_f^2 + r_f^2}$$

For the 100 μm fibers used in this dissertation, $r = 0.9902$. As stated previously,
the behavior of a fiber depends on the path angle β. When $\beta < \beta_0$, fibers
asymptotically converge to an equilibrium position that is approximately normal
to the fiber path orientation. When $\beta > \beta_0$, the fiber will behave like a fiber in
shear and asymptotically converge to an orientation tangential to the fiber path.
The value of the critical angle in the unperturbed flow is defined by Equation 6.9.

$$\beta_0 = r^2\cos\left(2\theta\right) + \sqrt{\left(1 - r^2\right)\left(1 - r^2\cos^2\left(2\theta\right)\right)} \tag{6.9}$$

The critical angle β_0, calculated using Equation 4.7, as well as the fraction of the die height that is within the critical angle, for each die angle is tabulated in Table 6.3.

TABLE 6.3: Die critical angle.

Die	θ	β_0	β_0/θ
A	0.00°	-	-
B	1.42°	0.24	16.9%
D	2.27°	0.59	26.0%
E	2.82°	0.89	31.6%
F	4.52°	2.02	44.9%

Vincent and Agassant provide three solutions to the Stokes flow problem based on the fiber path angle β: $\beta = 0$, $\beta < \beta_0$, and $\beta > \beta_0$.

$$\beta = 0: \qquad \phi = \tan^{-1}\left(C\rho^{-2r}\right) - \frac{\tau}{2} \tag{6.10}$$

$$\beta < \beta_0: \qquad \phi = \frac{X + Y + (X - Y)C\rho^{-2Y/\dot{\alpha}}}{\dot{\gamma}\left(1 + C\rho\rho^{-2Y/\dot{\alpha}}\right)} - \frac{\tau}{2} \tag{6.11}$$

$$\beta > \beta_0: \qquad \phi = \tan^{-1}\left(\frac{X}{\dot{\gamma}} - \frac{Y'}{\dot{\gamma}}\tan\left(\frac{Y'\log(\rho)}{\dot{\alpha}} + C\right)\right) - \frac{\tau}{2} \tag{6.12}$$

where τ, X, Y, and Y' are defined by:

$$\tau = \cos^{-1}\left(\frac{\dot{\alpha}}{\sqrt{\dot{\alpha}^2 + \dot{\gamma}^2}}\right) \qquad \text{or} \qquad \tau = \sin^{-1}\left(\frac{\dot{\gamma}}{\sqrt{\dot{\alpha}^2 + \dot{\gamma}^2}}\right) \tag{6.13}$$

$$X = r\sqrt{\dot{\alpha}^2 + \dot{\gamma}^2} \tag{6.14}$$

$$Y = \sqrt{\rho^2\dot{\alpha}^2 + \left(r^2 - 1\right)\dot{\gamma}^2} \tag{6.15}$$

$$Y' = \sqrt{\left(1 - r^2\right)\dot{\gamma}^2 - r^2\dot{\alpha}} \tag{6.16}$$

C is an integration constant based on the fiber orientation at the inlet of the die channel. Using the fiber path angle β, the fiber path orientation ϕ can be transformed into the fiber planar orientation by $\xi = \phi + \beta$. One consequence of using this model is that, while flow rate does appear in the shear and extension rate calculation, the form of the flow solutions is such that flow rate cancels. Therefore, the propose predictive model to be developed will not capture the effect of flow-rate on the solution. Because the fiber orientation is given over the entire channel width, we will assume that the mean of the fiber orientation $\bar{\xi}$ is representative of the effective fiber orientation across the thickness. The average fiber orientation is calculated using Equation 6.17.

$$\bar{\xi} = \frac{1}{2\theta} \int_{-\theta}^{\theta} \xi \left(\beta\right) d\beta \tag{6.17}$$

It should be noted that using the orientation model by Vincent and Agassant has several limitations. First, the calculation by Vincent and Agassant does not take into account shear dependency on viscosity, and so while it is likely that the viscosity across the channel does vary, this effect is not captured. Secondly, the effect of fiber-fiber interaction is not accounted for, so the results that come from this orientation prediction more than likely highly optimistic.

Now that the orientation of fibers across the thickness of a sample has been identified, we now want to connect this orientation model with a predictive model. For this, we choose the Agari-Uno model discussed in §6.1.5. MWNT concentration is handled within the properties of the matrix.
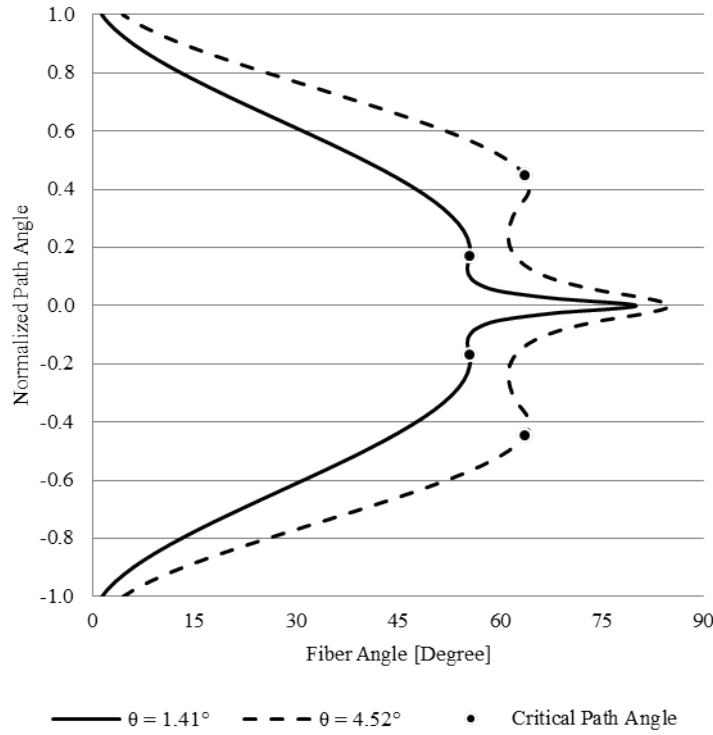
FIGURE 6.3: Fiber angle α plotted against normalized fiber path angle β/θ.

We now propose the modified Agari-Uno model, which will incorporate information about the MWNT concentration, CMF concentration, and the fiber orientation profile across the die. Again, the classic Agari-Uno model is defined as:

$$\ln\left(K_e\right) = V_f C_f \ln\left(K_f\right) + \left(1 - V_f\right)\ln\left(C_m K_m\right) \qquad (6.18)$$

In this formulation, the coefficient C_m captures the MWNT concentration, C_f captures the CMF orientation which is functionally dependent on die angle, flow rate, and fiber shape, and V_f captures the effect of increasing CMF concentration. These input parameters should well capture the parametric space explored in §5.3. Due to the relative simplicity of the model, we must assumed that fibers are well distributed throughout the composite, and that local variance in fiber

123

orientation is averaged out over the bulk of the composite.

To begin, we make two assumptions. First, that the effective CMF thermal conductivity is dependent on the average fiber orientation.

$$K_f = K_{f,0} + K_{f,\xi} \left(1 + \sin \left(\bar{\xi} - 90° \right) \right) \tag{6.19}$$

This assumption presents us with both a benefit and a challenge. First, this relationship more accurately takes into account that while CMFs have a measured conductivity, that conductivity is fully utilized by the composite due to finite length and interface resistance. By taking this assumption into account, we can reasonably show that the effective conductivity K_f of the CMF with respect to the composite is dependent on the mean fiber orientation $\bar{\xi}$, the initial effective conductivity of longitudinally aligned CMFs $K_{f,0}$, and the additional conductivity benefit for fibers aligned in the transverse orientation $K_{f,\xi}$. Note that $K_{f,\xi}$ is functionally dependent on interfacial resistance and fiber length, and since these were not directly accounted for in this study will be assumed to be some constant.

Next, we make the assumption that C_m is also dependent on the mean fiber orientation $\bar{\xi}$ and will take the form shown in Equation 6.20.

$$C_m = C_{m,0} + C_{m,\xi} \left(1 + \sin \left(\bar{\xi} - 90° \right) \right) \tag{6.20}$$

where $C_{m,0}$ is calculated at a die angle of $\theta = 0°$ and $C_{m,\xi}$ is some constant

representing MWNT concentration. It should be noted again that this model does not capture the effect of flow rate. While flow rate does appear in the rate calculations performed by Vincent and Agassant, these rates are treated as ratios in later reorientation calculations and are lost. In the following examination of the applicability of this model, we will then treat data as if flow rate was not a factor.

During fitting, $C_f = 1$ was found in all cases. The K_f was determined to be of the form $K_f = 3 + 7\left(1 + \sin\left(\bar{\xi} - 90°\right)\right)$. By this result, if CMFs are in a fully transverse orientation ($\xi = 90°$), the effective CMF thermal conductivity is 10 W/mK, which is approximately 55 times more conductive than PBT (0.18 W/mK). While this is still dramatically less than the manufacturer specified CMF thermal conductivity, it is still near the asymptotic limit after which increasing CMF thermal conductivity will provide negligible benefits. At 0 wt.% MWNT concentration, $C_m = 1.6$, and at 2 wt.% MWNT concentration, $C_m = 1.4 + 1.3\left(1 + \sin\left(\bar{\xi} - 90°\right)\right)$. This result is important so far as it is now clear that the benefit of MWNT concentration increasing with increasing die angle, which was not seen for the $\theta = 0°$ for either short CMFs or long CMFs. The fitted against the experimentally determined C_m values are plotted in Figure 6.4. Fitted values of C_m correlate very well with the experimentally identified values.

Correlation analysis was performed to examine the modified Agari-Uno model predicted thermal conductivity as compared against the measure thermal conductivity. A coefficient of determination $R^2 = 0.7358$ was found. Further
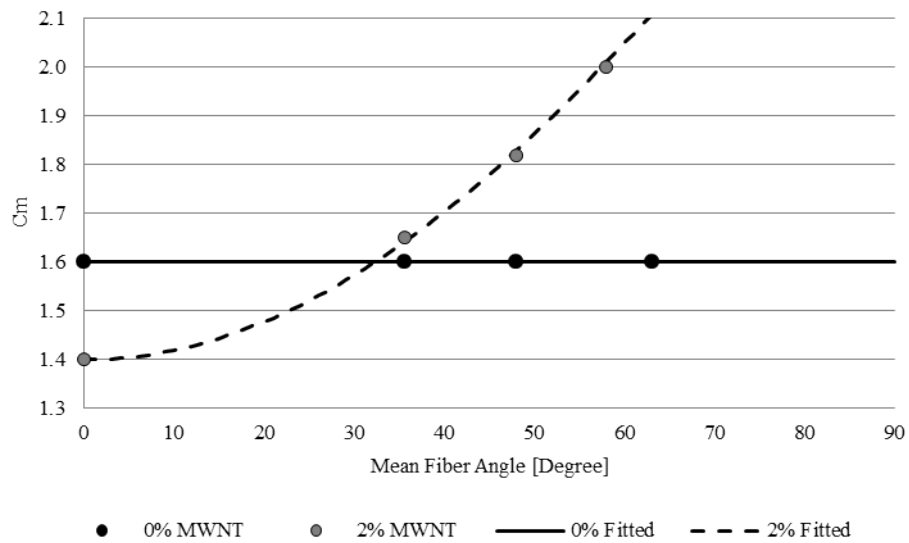
FIGURE 6.4: Experimental (marker) compared against fitted (line) C_m values. Note that at 0 wt.% MWNTs, the matrix coefficient is not effected by the die angle by means of the fiber orientation. However, at 2 wt.% MWNT, it is clear that the introduction of MWNTs has a very beneficial effect on thermal conductivity.

analysis shows that while the model captures the basic trends and is accurate to thermal conductivity which has been average across flow rates, its inability to capture the effect of flow rate is increasing the variance in the model. However, the modified Agari-Uno model sufficiently well captures the orientation dependent CMF thermal conductivity as well as the empirically the effect of MWNT concentration, and produces results which correlate well to measured thermal conductivity. It is worth noting that the $\theta = 2.82°$ condition is dramatically under predicted by the modified Agari-Uno model. However, this is unsurprising given that this was also an outlying condition in the regression analysis performed in §5.3. Finally, the procedure for calculating the modified Agari-Uno model does not accurately capture the depreciation in properties observed from 15 wt.% to 20 wt.% for one-run composites, or from 25 wt.% to 30 wt.% for

126

two-run composites.

The final procedure for generating the modified Agari-Uno model is as follows.

1. Calculate the mean fiber orientation parameter $\xi\left(\beta\right)$ from the Stokes flow solutions to a diverging channel flow using Equation 6.10, Equation 6.11, and Equation 6.12. This also requires the calculation of the shear and extension rates, as well as the critical path angle for the die.

2. Average the fiber orientation $\xi\left(\beta\right)$ across the width of the die to generate the mean fiber orientation $\bar{\bar{\xi}}$.

3. Calculate the effective thermal conductivity using Equation 6.18 and relationships for K_f and C_m (Equation 6.19 and Equation 6.20). For now, constants in these relationships must be determined from the $\theta = 0°$ condition and at least one other non-zero divergence angle.

Chapter 7

Conclusions and Future Studies

Although a significant amount of work concerning the compounding and manufacturing of multiscale PMCs has been performed including process-structure relationships and the synergistic benefits of fillers at multiple length scales, there has not been an effort to date to manipulate fiber orientation in the die of an extruder during the extrusion process and thereby select the best fiber structure for a given application. In order to address this issue, work in this dissertation focused on measuring the tensile and thermal properties of twin screw compounded PBT/CMF/MWNT multiscale composites whose fiber microstructure had been manipulated using a diverging flow in the die. A physics driven model, informed by statistical analysis and existing predictive models, was developed to predict the properties of these PMCs.

The research issues addressed in this work answered several questions related to fiber orientation in two-dimensional semi-infinite forms. The result of this

work is an advancement of microstructural and capability understanding of multiscale PMCs using CMFs and MWNTs. This work has more comprehensively explored the relationship of manipulating fiber orientation into the through-thickness orientation by fluid mechanical means, leading to enhanced heat transfer properties in the transverse orientation with some reduction of mechanical properties in the sheet planes. Furthermore, the benefit of MWNTs have now been realized for this application, which was not seen in preceding studies concerning this compounding method and constituents.

Centrally, a parametric study of short microfiber multiscale PMCs was conducted over a range of CMF concentrations, MWNT concentrations, flow rates, and die angle, the last three of which contribute to the reorientation of CMFs during pumping through the die. For each of the properties measured, tensile modulus, ultimate tensile strength, and thermal conductivity, different trends and interactions between the input parameters were measured.

For tensile modulus, without MWNTs, increasing flow rate has little effect on stiffness, with a mean tensile modulus increase of approximately 250% controlling for all other parameters. However, with MWNTs, controlling for all parameters, stiffness is reduced from 50% to 100% as compared to no MWNTs and demonstrates a decreasing trend with increasing flow rate. This is indicative of increase fiber reorientation in the presence of MWNTs with increasing flow rate. This behavior is likely due to the effect of fiber-fiber interaction on reorientation as die angle increases. It is important to note that these results did not behave in a particularly linear fashion, and the mechanical properties

for $\theta = 2.82°$ demonstrate behavior very much out of line with respect to any other die angle in the trends. This was reflected in the relatively poor correlation coefficient of $R^2 = 0.670$. In the future, it may be beneficial to explore around the $\theta = 2.82°$ region to determine if this is a type of sweet spot for property enhancement.

Ultimate tensile strength was found to follow the most obvious trends. Increasing die angle leads to an decreased ultimate tensile strength. This is consistent with fibers being reoriented more out of plane as fiber angle increases due to a greater die angle, leading to less CMFs contributing to the strength of the composite. MWNTs significantly reduce the overall strength of the composite. It would be beneficial in the future to explore the ultimate strength of these composites in order to using different lengths to improve mechanical load transfer, as well as to explore the potential for increased fiber damage with increasing viscosity due to MWNT concentration.

For thermal conductivity, two significant effects were observed. First, thermal conductivity increases with increase CMF concentration. Furthermore, the presence of MWNTs acts to increase thermal conductivity nearly 50% more than without. In the absence of MWNTs, increasing flow rate improves thermal conductivity increase. However, in the presence of MWNTs, all three flow rates demonstrate increasing thermal conductivity with increasing die angle. These effects in composite appear to indicate that MWNTs again improve the reorientation of CMFs, leading to improved transverse thermal conductivity, and that MWNTs may be acting to improve the matrix thermal conductivity as well. This

is likely related to both fiber damage due to increased viscosity as well as the increase in viscosity either aiding the reorientation of fibers or preventing the aligning fibers int he first place during pumping throught he die.

Between all parameters, it is clear that fiber reorientation leads to improved transverse properties at the cost of longitudinal tensile properties. Furthermore, these trends were used to inform a physics based model developed from the flow solutions to the Stokes flow in a diverging channel and the predictive Agari-Uno model.

7.1   Intellectual Contributions

Through this research effort, the following specific intellectual contributions were made for PBT/CMF/MWNT multiscale composite compounding and properties.

- The capability of fiber reorientation towards a semi-transverse orientation during pumping through a diverging die flow has been computationally and experimentally demonstrated systematically across a range of CMF concentration, MWNT concentrations, flow rates, and die angels.

  - The utility of MWNTs for enhanced through thickness heat transfer has been realized in multiscale composites as observed by direct transverse heat transfer improvement with MWNT presence when controlling for all other inputs.

∗ The utility of purely CMF concentration was found to be limited in a diverging die flow without the addition of MWNTs. With the addition of 2 wt.% MWNTs, heat transfer was observed to increase by up to 50% controlling for other variables.

- A parametric study investigating CMF concentration, MWNT concentration, flow rate, and die angle was performed.

  – In general, increasing CMF and MWNT concentrations improved thermal conductivity and tensile properties. For a zero-divergence die, MWNT concentration as not found to have a significant benefit to longitudinal tensile properties or transverse thermal conductivity. However, post-reorientation, increasing both CMF and MWNT concentration was beneficial.

  – The specific main and interaction effects between input parameters were statistically examined and empirical insights were gained.

- A new physics based model was developed using on the fiber reorientation model by Vincent and Agassant and the Agari-Uno predictive model.

  – This model successfully captures the effect of fiber reorientation, CMF concentration, and MWNT concentration on properties.

- Investigated and identified a processing work-around to reach up to 30 wt.% (22 vol.%) CMF concentration as well as processing limitations at these high loadings.

7.2   Future Work

During the course of work, future research avenues were identified.

1. *Confocal Microscopy.* Using an optically transparent polymer matrix, use confocal microscopy to visualize the three-dimensional fiber structure. Currently, planar optical microscopy does not sufficiently capture fiber orientation information to meaningfully correlate to measured physical properties, nor can make an accurate assessment of fiber damage at high loadings. Using a volumetric visualization approach, more insight into the effect of structure on properties can be derived.

   - *Entropic Characterization.* Continue the development of entropic characterization of fiber filled PMCs. Early in this dissertation, entropy measures for analyzing the distribution of fibers in planar micrographs were developed. However, as previously stated, planar microscopy does not sufficiently capture the 3D fiber structure, and so entropy analysis was removed. However, with a volumetric representation of the fiber structure, entropy could be employed more meaningfully to gain insight into structure-property relationships.

2. *Post-Extrusion Fiber Manipulation.* Explore the potential to apply secondary fluid mechanical manipulation using rollers or other techniques to further reorient fibers in the center and edges of the sheet. The flow solutions of Vincent and Agassant [86] show that fiber orientation near

133

the edges of the die will always demonstrate low reorientation. There-fore, investigating the capability of secondary reorientation by mechani-cal manipulation may yield yet more fiber reorientation into the through-thickness orientation.

3. *Effect of MWNTs on Viscosity.* Investigate the effect of MWNT inclusion on the viscosity of the polymer matrix. Authors have already show that the inclusion of MWNTs in a randomly aligned state both increase the vis-cosity of the polymer matrix as well as changes the shear-dependency of viscosity. However, it has also been shown that by aligning the MWNTs, this increase is somewhat diminished. Therefore, in order to understand the effects of matrix viscosity and the complex nature of the MWNT-shear dependency on CMF reorientation, it would be beneficial to conduct rhe-ological study on these melts in order to identify their contribution to the observed increase in thermal conductivity and other properties with and without the contribution of MWNTs.

4. *Effect of Matrix Morphology.* Investigate the effect of matrix properties, i.e. viscosity, on fiber manipulation. Low shear rates near the center of the dies flow may lead to reduced reorientability due to viscosity shear dependency. By examining another matrix with low viscosity or a more preferential shear rate dependency, there is potential for increased fiber reorientability.

5. *Alternative Matrix.* Reach higher total physical properties by using a ma-trix with higher neat properties. CMF/MWNT concentration effects in

different matrices are expected to be different than those determined in this body of work. However, as demonstrated in §6.1.6, beyond a filler/-matrix property ratio of 50, the utility of Filler contribution dramatically decreases. Therefore, the use of a matrix with higher neat properties is imperative to increased performance.

6. *Higher CMF concentration.*Investigate the potential for further property increases by increasing CMF and MWNT concentration. Due to fiber-fiber interaction during mixing, it is likely that a non-intermeshing twin screw extruder is necessary due to its exceedingly higher free volume as compared to an intermeshing twin screw extruder like the one used in this work.

   - Explore the effect of high CMF ($V_\mu > 19.4$ vol.%) concentration the freedom of fiber reorientation in the die.

7. *In-Situ Cross Linking.* Investigate compounding with a low molecular weight polymer matrix to reduce fiber damage during the processing. During this process, add an agent which increases the cross linking, increasing the polymer molecular weight after fillers have been sufficiently compounded in.

Appendix A

Property Summaries

The following appendix tabulates the mean μ, standard deviation σ, percent difference mean from neat $\%\mu$ calculated using Equation A.1, and percent difference standard deviation $\%\sigma$ calculated using Equation A.2 values presented in Chapter 5.

$$\%\mu = \frac{\mu - \mu_{neat}}{\mu_{neat}} \tag{A.1}$$

$$\%\sigma = \frac{\sigma}{\sigma_{neat}} \tag{A.2}$$

TABLE A.1: Physical properties for $l_f = 6$ mm, $\theta = 0°$. Each property is arranged into three columns: measured mean, standard deviation, and percent increase. Statistics were calculated using eight samples on average.

PBT	V_μ	V_n	Q	Tensile Modulus			Ultimate Strength			Thermal Conductivity		
wt.%	wt.%	wt.%	kg/hr	GPa		%	MPa		%	W/mK		%
100%	0%	0.0%	1.81	2.41	0.13	-	49.0	2.2	-	30.7	6.1	-
100%	0%	0.5%	1.81	1.87	0.13	-22%	11.0	4.6	-77%	7.2	0.1	-76%
99%	0%	1.0%	1.81	2.48	0.52	3%	39.7	10.4	-19%	28.0	0.1	-9%
99%	0%	1.5%	1.81	-	-	-	-	-	-	-	-	-
98%	0%	2.0%	1.81	-	-	-	-	-	-	-	-	-
90%	10%	0.0%	1.81	5.67	0.76	135%	51.8	6.9	6%	39.9	8.9	30%
90%	10%	0.5%	1.81	4.36	0.53	81%	36.0	15.5	-26%	30.4	7.8	-1%
89%	10%	1.0%	1.81	6.36	0.61	164%	63.0	9.6	28%	49.7	7.6	62%
89%	10%	1.5%	1.81	3.68	0.37	53%	28.8	5.0	-41%	23.7	7.1	-23%
88%	10%	2.0%	1.81	3.72	0.24	55%	24.9	6.7	-49%	22.6	6.4	-26%
85%	15%	0.0%	1.81	7.61	1.28	216%	65.0	7.7	33%	52.6	8.0	71%
85%	15%	0.5%	1.81	7.88	1.13	227%	71.9	3.1	47%	49.8	18.7	62%
84%	15%	1.0%	1.81	7.95	1.09	230%	66.9	13.1	37%	49.0	0.7	60%
84%	15%	1.5%	1.81	5.05	0.46	110%	44.6	4.9	-9%	41.5	6.1	35%
83%	15%	2.0%	1.81	4.58	0.73	90%	30.9	9.3	-37%	28.1	9.2	-9%
80%	20%	0.0%	1.81	10.67	1.11	343%	71.1	0.9	45%	51.5	13.8	68%
80%	20%	0.5%	1.81	4.22	0.64	75%	23.9	10.2	-51%	20.1	11.0	-35%
79%	20%	1.0%	1.81	5.17	0.37	114%	44.1	6.1	-10%	38.8	8.1	27%
79%	20%	1.5%	1.81	4.99	0.44	107%	40.6	6.1	-17%	38.5	6.5	25%
78%	20%	2.0%	1.81	5.70	0.32	137%	41.9	7.0	-14%	38.2	8.6	24%
75%	25%	0.0%	1.81	14.65	2.41	508%	79.5	10.7	62%	55.2	8.2	80%
75%	25%	0.5%	1.81	5.36	0.42	123%	53.0	11.9	8%	46.2	11.2	51%
74%	25%	1.0%	1.81	5.88	0.63	144%	45.3	9.6	-8%	41.7	9.4	36%
74%	25%	1.5%	1.81	7.96	1.83	231%	50.6	14.5	3%	46.1	12.2	50%
73%	25%	2.0%	1.81	8.76	0.41	264%	53.7	14.1	10%	46.0	15.9	50%
70%	30%	0.0%	1.81	13.17	0.83	447%	75.7	6.2	54%	66.0	7.0	115%
70%	30%	0.5%	1.81	10.87	1.75	351%	87.4	8.1	78%	63.9	8.8	108%
69%	30%	1.0%	1.81	10.58	1.09	339%	78.9	11.9	61%	70.7	5.3	130%
69%	30%	1.5%	1.81	9.68	1.07	302%	66.4	7.4	36%	62.8	8.0	105%
68%	30%	2.0%	1.81	10.62	1.08	341%	55.3	7.7	13%	50.6	9.6	65%

TABLE A.2: Physical properties for $l_f = 100$ μm, $\theta = 0°$. Each property is arranged into three columns: measured mean, standard deviation, and percent increase. Statistics were calculated using eight samples on average.

PBT	V_μ	V_n	Q	Tensile Modulus			Ultimate Strength			Thermal Conductivity		
wt.%	wt.%	wt.%	kg/hr	GPa		%	MPa		%	W/mK		%
90%	10%	0%	1.81	6.51	0.19	170%	59.3	3.17	21%	0.257	0.001	43%
85%	15%	0%	1.81	7.28	0.27	202%	64.2	3.06	31%	0.346	0.007	92%
80%	20%	0%	1.81	8.48	0.44	252%	73.0	2.82	49%	0.387	0.002	115%
75%	25%	0%	1.81	9.11	0.44	278%	73.5	3.90	50%	0.446	0.010	148%
70%	30%	0%	1.81	11.13	0.42	362%	68.1	4.36	39%	0.423	0.017	135%
88%	10%	2%	1.81	4.46	0.35	85%	23.0	1.81	-53%	0.274	0.027	52%
83%	15%	2%	1.81	4.99	0.35	107%	32.3	3.25	-34%	0.328	0.016	82%
78%	20%	2%	1.81	5.57	0.43	131%	41.7	3.81	-15%	0.349	0.035	94%
73%	25%	2%	1.81	5.66	0.71	135%	38.7	0.85	-21%	0.412	0.070	129%
68%	30%	2%	1.81	5.88	0.80	144%	57.8	5.05	18%	0.405	0.027	125%

TABLE A.3: Physical properties for $l_f = 100$ μm, $\theta = 1.41°$. Each property is arranged into three columns: measured mean, standard deviation, and percent increase. Statistics were calculated using eight samples on average.

PBT	V_μ	V_n	Q	Tensile Modulus			Ultimate Strength			Thermal Conductivity		
wt.%	wt.%	wt.%	kg/hr	GPa		%	MPa		%	W/mK		%
90%	10%	0%	1.36	3.83	0.18	59%	54.9	2.25	12%	0.360	0.010	100%
85%	15%	0%	1.36	5.42	0.95	125%	57.8	2.41	18%	0.387	0.025	115%
80%	20%	0%	1.36	8.07	0.51	235%	55.9	4.21	14%	0.396	0.036	120%
75%	25%	0%	1.36	10.97	0.40	355%	47.0	1.56	-4%	0.425	0.015	136%
70%	30%	0%	1.36	9.33	0.72	287%	44.1	2.40	-10%	0.441	0.011	145%
90%	10%	0%	1.81	5.49	0.07	128%	47.0	9.31	-4%	0.351	0.039	95%
85%	15%	0%	1.81	6.12	0.17	154%	51.0	7.07	4%	0.392	0.009	118%
80%	20%	0%	1.81	8.94	0.18	271%	52.4	3.70	7%	0.405	0.010	125%
75%	25%	0%	1.81	12.53	0.17	420%	53.9	5.70	10%	0.423	0.020	135%
70%	30%	0%	1.81	9.30	0.76	286%	52.9	5.69	8%	0.436	0.004	142%
90%	10%	0%	2.27	6.46	0.53	168%	52.9	0.50	8%	0.389	0.006	116%
85%	15%	0%	2.27	7.71	0.64	220%	54.9	3.43	12%	0.405	0.001	125%
80%	20%	0%	2.27	8.53	0.36	254%	59.8	6.93	22%	0.418	0.058	132%
75%	25%	0%	2.27	9.21	0.60	282%	60.8	7.59	24%	0.446	0.063	148%
70%	30%	0%	2.27	8.87	0.53	268%	51.9	4.48	6%	0.486	0.020	170%
88%	10%	2%	1.36	6.46	0.35	168%	16.2	4.43	-67%	0.364	0.025	102%
83%	15%	2%	1.36	6.99	0.78	190%	15.2	4.77	-69%	0.396	0.025	120%
78%	20%	2%	1.36	7.33	0.31	204%	16.2	4.55	-67%	0.445	0.010	147%
73%	25%	2%	1.36	5.64	0.31	134%	19.6	3.92	-60%	0.473	0.020	163%
68%	30%	2%	1.36	4.34	0.05	80%	20.1	5.39	-59%	0.434	0.019	141%
88%	10%	2%	1.81	5.74	0.78	138%	32.3	3.04	-34%	0.342	0.037	90%
83%	15%	2%	1.81	6.51	0.27	170%	29.4	1.85	-40%	0.391	0.021	117%
78%	20%	2%	1.81	6.94	0.24	188%	28.4	5.88	-42%	0.405	0.042	125%
73%	25%	2%	1.81	5.54	0.64	130%	29.9	1.96	-39%	0.427	0.034	137%
68%	30%	2%	1.81	4.43	1.21	84%	33.3	4.41	-32%	0.436	0.017	142%
88%	10%	2%	2.27	3.57	0.24	48%	24.5	1.96	-50%	0.389	0.059	116%
83%	15%	2%	2.27	4.29	0.31	78%	20.6	6.47	-58%	0.437	0.011	143%
78%	20%	2%	2.27	5.11	0.05	112%	20.1	5.88	-59%	0.459	0.008	155%
73%	25%	2%	2.27	4.39	0.36	82%	23.0	1.47	-53%	0.475	0.029	164%
68%	30%	2%	2.27	3.76	0.17	56%	25.0	4.41	-49%	0.513	0.020	185%

TABLE A.4: Physical properties for $l_f = 100$ µm, $\theta = 2.26°$. Each property is arranged into three columns: measured mean, standard deviation, and percent increase. Statistics were calculated using eight samples on average.

PBT	V_μ	V_n	Q	Tensile Modulus			Ultimate Strength			Thermal Conductivity		
wt.%	wt.%	wt.%	kg/hr	GPa		%	MPa		%	W/mK		%
90%	10%	0%	1.36	6.41	0.22	166%	33.8	5.39	-31%	0.353	0.020	96%
85%	15%	0%	1.36	7.37	0.34	206%	42.1	0.98	-14%	0.378	0.014	110%
80%	20%	0%	1.36	7.95	0.68	230%	51.0	3.92	4%	0.387	0.055	115%
75%	25%	0%	1.36	8.24	0.36	242%	54.4	3.11	11%	0.419	0.027	133%
70%	30%	0%	1.36	9.21	0.72	282%	52.4	2.26	7%	0.437	0.006	143%
90%	10%	0%	1.81	7.18	0.37	198%	49.5	9.70	1%	0.333	0.020	85%
85%	15%	0%	1.81	7.71	0.17	220%	51.5	1.71	5%	0.365	0.013	103%
80%	20%	0%	1.81	10.27	0.26	326%	52.9	7.74	8%	0.396	0.001	120%
75%	25%	0%	1.81	11.09	0.59	360%	54.4	1.06	11%	0.432	0.010	140%
70%	30%	0%	1.81	10.89	0.17	352%	55.9	3.05	14%	0.464	0.020	158%
90%	10%	0%	2.27	5.69	0.40	136%	55.9	0.99	14%	0.329	0.013	83%
85%	15%	0%	2.27	6.99	0.22	190%	57.3	0.21	17%	0.356	0.046	98%
80%	20%	0%	2.27	7.90	0.70	228%	60.8	3.39	24%	0.396	0.016	120%
75%	25%	0%	2.27	9.11	0.34	278%	64.7	6.86	32%	0.443	0.057	146%
70%	30%	0%	2.27	10.22	0.12	324%	62.2	2.94	27%	0.506	0.017	181%
88%	10%	2%	1.36	5.06	0.91	110%	26.5	7.13	-46%	0.328	0.099	82%
83%	15%	2%	1.36	6.70	0.29	178%	33.3	3.43	-32%	0.427	0.026	137%
78%	20%	2%	1.36	7.76	0.02	222%	37.2	3.92	-24%	0.472	0.046	162%
73%	25%	2%	1.36	10.03	0.51	316%	27.0	4.41	-45%	0.509	0.033	183%
68%	30%	2%	1.36	12.19	0.24	406%	2.9	0.51	-94%	0.540	0.062	200%
88%	10%	2%	1.81	5.47	0.27	127%	17.6	0.49	-64%	0.394	0.030	119%
83%	15%	2%	1.81	7.52	0.32	212%	10.3	3.43	-79%	0.441	0.017	145%
78%	20%	2%	1.81	7.25	0.02	201%	0.0	3.92	-99%	0.504	0.012	180%
73%	25%	2%	1.81	6.94	0.25	188%	1.5	4.41	-97%	0.590	0.048	228%
68%	30%	2%	1.81	11.09	0.10	360%	8.8	0.51	-82%	0.556	0.047	209%
88%	10%	2%	2.27	4.27	0.17	77%	12.7	6.86	-74%	0.385	0.025	114%
83%	15%	2%	2.27	4.77	0.29	98%	7.8	0.98	-84%	0.437	0.049	143%
78%	20%	2%	2.27	5.71	0.46	137%	2.5	4.41	-95%	0.497	0.034	176%
73%	25%	2%	2.27	5.98	0.02	148%	10.3	5.39	-79%	0.544	0.084	202%
68%	30%	2%	2.27	5.62	0.12	133%	22.5	0.49	-54%	0.567	0.040	215%

TABLE A.5: Physical properties for $l_f = 100$ μm, $\theta = 2.82°$. Each property is arranged into three columns: measured mean, standard deviation, and percent increase. Statistics were calculated using eight samples on average.

PBT	V_μ	V_n	Q	Tensile Modulus			Ultimate Strength			Thermal Conductivity		
wt.%	wt.%	wt.%	kg/hr	GPa		%	MPa		%	W/mK		%
90%	10%	0%	1.81	7.33	0.41	204%	32.3	2.05	-34%	0.220	0.001	22%
85%	15%	0%	1.81	8.44	0.31	250%	36.8	3.94	-25%	0.290	0.007	61%
80%	20%	0%	1.81	9.01	0.67	274%	51.9	2.96	6%	0.315	0.002	75%
75%	25%	0%	1.81	9.98	0.46	314%	71.1	3.46	45%	0.394	0.010	119%
70%	30%	0%	1.81	10.80	0.99	348%	91.1	8.73	86%	0.425	0.017	136%
88%	10%	2%	1.81	4.24	0.41	76%	38.2	1.81	-22%	0.391	0.012	117%
83%	15%	2%	1.81	4.55	0.60	89%	35.8	3.25	-27%	0.412	0.021	129%
78%	20%	2%	1.81	5.40	0.54	124%	28.9	3.81	-41%	0.479	0.052	166%
73%	25%	2%	1.81	5.95	0.13	147%	38.7	0.85	-21%	0.466	0.070	159%
68%	30%	2%	1.81	5.30	0.74	120%	46.1	5.05	-6%	0.553	0.027	207%

TABLE A.6: Physical properties for $l_f = 100$ μm, $\theta = 4.52°$. Each property is arranged into three columns: measured mean, standard deviation, and percent increase. Statistics were calculated using eight samples on average.

PBT	V_μ	V_n	Q	Tensile Modulus			Ultimate Strength			Thermal Conductivity		
wt.%	wt.%	wt.%	kg/hr	GPa		%	MPa		%	W/mK		%
90%	10%	0%	1.36	7.62	0.31	216%	49.0	5.52	0%	0.266	0.024	48%
85%	15%	0%	1.36	8.24	0.35	242%	48.5	4.35	-1%	0.286	0.013	59%
80%	20%	0%	1.36	8.92	0.54	270%	43.1	9.31	-12%	0.326	0.006	81%
75%	25%	0%	1.36	8.72	0.00	262%	34.8	9.80	-29%	0.344	0.042	91%
70%	30%	0%	1.36	8.10	0.68	236%	36.3	5.39	-26%	0.367	0.072	104%
90%	10%	0%	1.81	7.76	0.27	222%	55.9	4.63	14%	0.306	0.012	70%
85%	15%	0%	1.81	8.05	0.87	234%	45.6	7.74	-7%	0.346	0.043	92%
80%	20%	0%	1.81	8.29	0.31	244%	41.2	6.37	-16%	0.378	0.027	110%
75%	25%	0%	1.81	8.53	0.50	254%	37.7	0.87	-23%	0.401	0.048	123%
70%	30%	0%	1.81	8.82	0.69	266%	44.6	6.30	-9%	0.405	0.027	125%
90%	10%	0%	2.27	7.09	0.36	194%	51.0	5.43	4%	0.367	0.006	104%
85%	15%	0%	2.27	8.19	0.10	240%	52.4	3.39	7%	0.398	0.010	121%
80%	20%	0%	2.27	9.21	0.53	282%	54.4	3.48	11%	0.434	0.018	141%
75%	25%	0%	2.27	10.46	0.27	334%	53.4	5.88	9%	0.466	0.020	159%
70%	30%	0%	2.27	11.38	0.53	372%	55.9	0.49	14%	0.502	0.022	179%
88%	10%	2%	1.36	4.68	0.62	94%	11.8	9.31	-76%	0.385	0.020	114%
83%	15%	2%	1.36	5.21	0.03	116%	0.0	5.39	-99%	0.437	0.025	143%
78%	20%	2%	1.36	5.93	0.34	146%	9.8	6.49	-80%	0.486	0.030	170%
73%	25%	2%	1.36	6.24	0.39	159%	14.2	5.88	-71%	0.549	0.024	205%
68%	30%	2%	1.36	6.60	0.22	174%	15.7	1.47	-68%	0.590	0.016	228%
88%	10%	2%	1.81	4.39	0.63	82%	16.2	6.86	-67%	0.423	0.011	135%
83%	15%	2%	1.81	5.11	0.14	112%	9.3	5.49	-81%	0.464	0.020	158%
78%	20%	2%	1.81	5.66	0.10	135%	2.9	4.58	-94%	0.515	0.030	186%
73%	25%	2%	1.81	6.34	0.03	163%	0.5	8.37	-99%	0.562	0.015	212%
68%	30%	2%	1.81	6.96	0.04	189%	5.9	7.10	-88%	0.607	0.022	237%
88%	10%	2%	2.27	4.19	0.14	74%	11.8	0.98	-76%	0.445	0.015	147%
83%	15%	2%	2.27	4.84	0.05	101%	9.3	3.43	-81%	0.482	0.037	168%
78%	20%	2%	2.27	5.35	0.50	122%	4.4	5.70	-91%	0.518	0.033	188%
73%	25%	2%	2.27	6.22	0.54	158%	13.7	6.69	-72%	0.556	0.010	209%
68%	30%	2%	2.27	6.24	0.90	159%	17.6	9.54	-64%	0.599	0.072	233%

Bibliography

[1] J. Coleman, U. Khan, W. Blau, and Y. Gunko. Small but strong: A review of the mechanical properties of carbon nanotubepolymer composites. *Carbon*, 44(9):16241652, 2006.

[2] T. Villmow, P. Potschke, S. Pegel, L. Haussler, and B. Kretzchmar. Influence of twin-screw extrusion conditions on the dispersion of multi-walled carbon nanotubes in poly(lactic acid) matrix. *Polymer*, 49(16):35003509, 2008.

[3] A. Kota. *Processing-Structure-Microstructure-Property Relationships in Polymer Nanocomposites*. PhD thesis, University of Maryland, 2007.

[4] Z. Tadmor and C. G. Gogos. *Principles of Polymer Processing*. Wiley-Interscience, 2006.

[5] F. Li, H. Cheng, S. Bai, G. Su, and M. S. Dresselhaus. Tensile strength of single-walled carbon nanotubes directly measured from their macroscopic ropes. *Applied Physical Letters*, 77(20):3161–3163, 2000.

[6] D. A. Walters, L. M. Ericson, M. Casavant, J. Liu, D. T. Colbert, K. A. Smith, and R. E. Smalley. Elastic strain of freely suspended single-wall carbon nanotube ropes. *Applied Physical Letters*, 74(25):3803–3805, 1999.

[7] J. P. Salvetat, J. M. Bonnard, N.H. Thomson, A.J. Kuklik, L. Forro, W. Benoit, and L. Zuppiroli. Mechanical properties of carbon nanotubes. *Applied Physics A Materials Science and Processing*, 69(3):255–260, 1999.

[8] Y. Li. Effect of addition of carbon nanofibers and carbon nanotubes on properties of thermoplastic biopolymers. *Polymer*, 52(10):23102318, 2011.

[9] Z. Spitalsky, D. Tasis, K. Papagelis, and C. Galiotis. Carbon nanotube/polymer composites: Chemistry, processing, mechanical and electrical properties. *Progress in Polymer Science*, 35(3):357401, 2010.

[10] M. Sanchez-Garcia, J. Lagaron, and S. Hoa. Effect of addition of carbon nanofibers and carbon nanotubes on properties of thermoplastic biopolymers. *Composites Science and Technology*, 10(7):1095–1105, 2011.

[11] M. Moniruzzaman and K. Winey. Polymer nanocomposites containing carbon nanotubes. *Macromolecules*, 39(16):51945205, 2006.

[12] J. Salvetat, A. Kulik, J. Bonard, G. Briggs, T. Stockli, K. Metenier, S. Bonnamy, F. Beguin, N. Burnham, and L. Forro. Elastic modulus of ordered and disordered multi-walled carbon nanotubes. *Advanced Materials*, 11(2):161–165, 1999.

[13] O. Breuer and U. T. Sundararaj. Big returns from small fibers: a review of polymer/carbon nanotube composites. *Polymer Composites*, 25(6):630–645, 2004.

[14] P. Potschke, T. D. Fornes, and D. R. Paul. Rheological behavior of multiwalled carbon nanotube/polycarbonate composites. *Polymer*, 43(11): 3247–3255, 2002.

[15] W. Ding, A. Eitan, F. T. Fischer, X. Chen, D. A. Dikin, and R. Andrews. Direct observation of polymer sheathing in carbon nanotube polycarbonate composites. *Nano Letters*, 3(11):1593–1596, 2003.

[16] E. Assouline, A. Lustiger, A. H. Barber, C. A. Cooper, E. Klein, E. Watchel, and H. D. Wagner. Nucleation ability of multiwall carbon nanotubes in polypropylene composites. *Journal of Polymer Science: Part B*, 41:520–527, 2003.

[17] X. L. Xie, K. Aloys, X. P. Zhou, and F. D. Zeng. Ultrahigh molecular mass polyethylene/carbon nanotube composites - crystallization and melting properties. *Journal of Thermal Analysis and Calorimetry*, 74: 317–323, 2003.

[18] J. Sandler, G. Broza, M. Nolte, K. Schulte, Y.-M. Lam, and M. S. P. Shaffer. Crystallization of carbon nanotube and nanofiber polypropylene composites. *Journal of Macromolecular Science: Part B*, 42(3-4):479–488, 2003.

[19] B. P. Grady, F. Pompeo, R. L. Shambaugh, and D. E. Resasco. Nucleation of polypropylene crystallization by single-walled carbon nanotubes. *Journal of Physical Chemisty: Part B*, 106:106, 2002.

[20] R. Islam and A. Pramila. Thermal conductivity of fiber reinforced composites by the fem. *Journal of Composite Materials*, 33(18):1699–1715, 1999.

[21] C.-W. Nan, R. Berringer, D. R. Clarke, and H. Gleiter. Effective thermal conductivity of particulate composites with interfacial thermal resistance. *Journal of Applied Physics*, 82:6692–6699, 1997.

[22] A. Kothari, K. Jian, J. Rankin, and B. Sheldon. Comparison between carbon nanotube and carbon nanofiber reinforcements in amorphous silicon nitride coatings. *Journal of the American Ceramic Society*, 91(8): 27432746, 2008.

[23] R. Andrews, D. Jacques, M. Minot, and T. Rantell. Fabrication of carbon multi-wall nanotube/polymer composites by shear mixing. *Macromolecular Materials and Engineering*, 287(6):395403, 2002.

[24] M. A. Lopez Machando, V. Valenti, J. Biagiotti, and J. M. Kenny. Thermal and mechanical properties of single-walled carbon nanotube-spolypropylene composites prepared by melt processing. *Carbon*, 43: 1499–1505, 2005.

[25] R. Andrews, D. Jacques D. L. Qian, and T. Rantell. Multi-wall carbon nanotubes: synthesis and application. *Accounts of Chemical Research*, 35(12):1008–1017, 2002.

[26] S. Wang, R. Liang, B. Wang, and C. Zhang. Dispersion and thermal conductivity of carbon nanotube composites. *Carbon*, 47:53–57, 2009.

[27] S. Frusteri, V. Leonardi, S. Vasta, and G. Restuccia. Thermal conductivity measurement of a pcm based storage system containing carbon fibers. *Applied Thermal Engineering*, 25(11):16231633, 2005.

[28] J. L. Thomason and M. A. Vlug. Influence of fiber length and concentration on the properties of glass fibre-reinforced polypropylene: 1. tensile and flexural modulus. *Composites: Part A*, 27A:477–484, 1996.

[29] X.-L. Xie, Y.-W. Mai, and X.-P. Zhou. Dispersion and alignment of carbon nanotubes in polymer matrix: A review. *Material Science and Technology*, 49:89–112, 2005.

[30] P.-C. Ma, N. A. Siddiqui, G. Marom, and J.-K. Kim. Dispersion and functionalization of carbon nanotubes for polymer-based nanocomposites: A review. *Composites: Part A*, 41:1345–1376, 2010.

[31] D. Tasis, N. Tagmatarchis, V. G eorgakilas, and M. Prato. Soluble carbon nanotubes. *Chemistry-A European Journal*, 9(17):4000–4008, 2003.

[32] D. Tasis, N. Tagmatarchis, A. Bianco, and M. Prato. Chemistry of carbon nanotube. *Chemical Reviews*, 106:1105–1136, 2006.

[33] M. Sharma, S. Gao, E. Madar, H. Sharma, L. Y. Wei, and J. Bijwe. Carbon fiber surfaces and composite interphases. *Composites Science and Technology*, 102:35–50, 2014.

[34] S. Tiwari and J. Bijwe. Surface treatment of carbon fibers: a review. *Procedia Technology*, 14:505–512, 2014.

[35] X. Gong, J. Liu, S. Baskaran, R. D. Voise, and J. S. Young. Surfactant-assisted processing of carbon nanotube/polymer composites. *Chemistry of Materials*, 12(4):1049–1052, 2000.

[36] S. Wang, Z. Liang, B. Wang, C. Zhang, and Z. Raman. Precise cutting of single walled carbon nanotubes. *Nanotechnology*, 17:055301–055306, 2007.

[37] H. Y. Kordkheili, M. Farsi, and Z. Rezazadeh. Physical, mechanical and morphological properties of polymer composites manufactured from carbon nanotubes and wood flour. *Composites: Part B*, 44:750–755, 2013.

[38] C. Unterwger, J. Duchoslav, D. Sifter, and C. Furst. Characterization of carbon fiber surfaces and their impact on the mechanical properties of short carbon fiber reinforced polypropylene composites. *Composites Science and Technology*, 108:41–47, 2015.

[39] J. Sandler, P. Werner, M. Shaffer, V. Demchuck, V. Altsadt, and A. Windle. Carbon-nanofibre-reinforced poly(ether ether ketone) composites. *Composites: Part A*, 33(8):1033–1039, 2002.

[40] T. Kashiwagi, E. Grulke, J. Hilding, R. Harris, W. Awad, and J. Douglas. Thermal degradation and flammability properties of poly(propylene)/carbon nanotube composites. *Macromolecular Rapid Communication*, 23(13):761–765, 2002.

[41] J. Cho and D. Paul. Nylon 6 nanocomposites by melt mixing. *Polymer*, 42(3):1083–1094, 2001.

[42] O. Carneiro, J. Covas, C. Bernardo, G. Caldeira, D. Hattum, J. Ting, R. Alig, and M. Lake. Production and assessment of polycarbonate composites reinforced with vapour-grown carbon fibres. *Composites Science and Technology*, 58(3-4):401–407, 1998.

[43] E. Bekyarova, E. Thostenson, A. Yu, H. Kim, J. Gao, J. Tang, H. Hahn, T. Chou, M. Itkis, and R. Haddon. Multiscale carbon nanotube-carbon

fiber reinforcement for advanced epoxy composites. *Langmuir*, 23(7): 39703974, 2007.

[44] K. Lozano and E. V. Barrera. Nanofiber-reinforced thermoplastic composites. i. thermoanalytical and mechanical analyses. *Journal of Applied Polymer Science*, 79(1):125–133, 2001.

[45] S. Lee, O. Choi, W. Lee, J. Yi, B. Kim, J. Byun, M. Yoon, H. Fong, E. Thostenson, and T. Chou. Processing and characterization of multiscale hybrid composites reinforced with nanoscale carbon reinforcements and carbon fibers. *Composites: Part A*, 45(4):337–344, 2011.

[46] G. Broza, M. Kwiatkowska, Z. Roslaniec, and K. Schulte. rocessing and assessment of poly(butylene terephthalate) nanocomposites reinforced with oxidized single wall carbon nanotubes. *Polymer*, 46(16):58605867, 2005.

[47] J. Zeng, B. Saltysiak, W. Johnson, D. Schiraldi, and S. Kumar. Processing and properties of poly(methyl methacrylate)/carbon nano fiber composites. *Composites: Part B*, 32(2):173–178, 2004.

[48] S. Yesil, O. Koysuren, and G. Bayram. Effect of microfiber reinforcement on the morphology, electrical, and mechanical properties of the polyethylene/poly(ethylene terephthalate)/carbon nanotube composites. *Polymer Engineering and Science*, 50(11):20932105, 2010.

[49] F. Incropera, D. Dewitt, T. Bergman, and A. Lavine. *Fundamentals of Heat and Mass Transfer*. John Wiley Sons, Inc., 2007.

[50] M. Bryning, D. Milkie, M. Islam, J. Kikkawa, and A. Yodh. Thermal conductivity and interfacial resistance in single-wall carbon nanotube epoxy composites. *Applied Physics Letters*, 87(16909):1–3, 2003.

[51] J. Hone, M. C. Llaguno, A. T. Johnson, B. Batlogg, Z. Benes, and J.E. Fischer. Thermal properties of carbon nanotubes and nanotube-based materials. *Applied Physics A Materials Science and Processing*, 74(3):339–343, 2002.

[52] S. Berber, Y. Kwon, and D. Tomanek. Unusually high thermal conductivity of carbon nanotubes. *Physical Review Letters*, 84(20):4613–4616, 2000.

[53] J. Che, T. Cagin, and W. Goddard. Thermal conductivity of carbon nanotubes. *Nanotechnology*, 11(2):65–69, 2000.

[54] Z. Han and A. Fina. Thermal conductivity of carbon nanotubes and their polymer nanocomposites: a review. *Progress in Polymer Science*, 36: 914–944, 2011.

[55] J. Hone, M. Whitney, C. Piskoti, and A. Zettl. Thermal conductivity of single-walled carbon nanotubes. *Physical Review B*, 59(4):25142516, 1999.

[56] P. Kim, L. Shi, A. Majumdar, and P. L. McEuen. Thermal transport measurements of individual multiwalled nanotubes. *Physical Review Letters*, 87(21):215502/1–4, 2001.

[57] C. Yu, L. Shi, Z. Yao, D. Li, , and A. Majumdar. Thermal conductance and thermopower of an individual single-wall carbon nanotube. *Nano Letters*, 5:1842–1846, 2005.

[58] S. Sinha, S. Barjami, G. Iannacchione, A. Schwab, and G. Muench. Off-axis thermal properties of carbon nanotube films. *Journal of Nanoparticle Research*, 7:651–657, 2005.

[59] S. Agarwal, M. Masud, K. Khan, and R. Gupta. Thermal conductivity of polymer nanocomposites made with carbon nanofibers. *Polymer Engineering and Science*, 48(12):24742481, 2008.

[60] R. S. Prasher, X. J. Hu, Y. Chalopin, N. Mingo, K. Lofgreen, S. Volz, F. Cleri, and P. Keblinski. Turning carbon nanotubes from exceptional heat conductors into insulators. *Physical Review Letters*, 102(105901): 1–4, 2009.

[61] M. Zimmer, Q. Cheng, S. Li, J. Brooks, R. Liang, B. Wang, and C. Zhang. Comparative characterization of multi-scale carbon fiber composites with long and short mwcnts at higher weight fractions. *Journal of Nanomaterials*, 2012(532080):1–9, 2012.

[62] T. Zhou, X. Wang, G. Mingyuan, and X. Liu. Study of the thermal conduction mechanism of nano-sic/dgeba/emi-2,4 composites. *Polymer*, 49 (21):46664672, 2008.

[63] Y.-P. Sun, K. Fu, Y. Lin, and W. Huang. Functionalized carbon nanotubes: properties and applications. *Accounts of Chemical Research*, 35 (12):1096–1104, 2002.

[64] S. Shenogin, A. Bodapati, L. Xue, R. Ozisik, and P. Keblinski. Effect of chemical functionalization on thermal transport of carbon nanotube composites. *Applied Physics Letters*, 85(12):2229–2231, 2004.

[65] F. Gojny, M. Wichmann, B. Fiedler, I. Kinloch, A. Windle W. Bauhofer, and K. Schulte. Evaluation and identification of electrical and thermal conduction mechanisms in carbon nanotube/epoxy composites. *Polymer*, 47(6):20362045, 2006.

[66] G. Chen, Y. Li, and H. Shimizu. Ultrahigh-shear processing for the preparation of polymer/carbon nanotube composites. *Carbon*, 45(12):2334–2340, 2007.

[67] T. Villmow, P. Potschke, S. Pegel, L. Haussler, and B. Kretzchmar. Influence of twin-screw extrusion conditions on the dispersion of multi-walled carbon nanotubes in poly(lactic acid) matrix. *Polymer*, 49(16):35003509, 2008.

[68] J. Vera-Agullo, A. Gloria-Pereira, H. Varela-Rizo, J. Gonzalez, and I. Martin-Gullon. Comparative study of the dispersion and functional properties of multiwall carbon nanotubes and helical-ribbon carbon nanofibers in polyester nanocomposites. *Composites Science and Technology*, 69(10):1521–1532, 2009.

[69] A. Scurati, D. L. Feke, and I. Manas-Zloczower. Analysis of the kinetics of agglomerate erosion in simple shear flows. *Chemical Engineering Science*, 60(23):6564–6573, 2005.

[70] J. Gao, G. Walsh, D. Bigio, R. Briber, and M. Wetzel. Residence time distributions model for twin-screw extruders. *AIChE Journal*, 45(12): 2541–2549, 1999.

[71] J. Gao, G. Walsh, D. Bigio, R. Briber, and M. Wetzel. Mean residence time analysis for twin screw extrusion. *Polymer Engineering and Science*, 40(1):227–237, 2000.

[72] W. Pappas. Characterization and comparison of stress history in various sized twin-screw extruders using residence stress distributions. Master's thesis, University of Maryland, 2011.

[73] G. Fukuda. A new scale-up approach through the evaluation of stress history within a twin-screw extruder. Master's thesis, University of Maryland, 2014.

[74] D. Acierno, P. Scarfato, E. Amendola, G. Nocerino, and G. Costa. Preparation and characterization of pbt nanocomposites compounded with different montmorillonites. *Polymer Engineering and Science*, 44(6):1012–1018, 2004.

[75] R. Kuriger, M. Alam, D. Anderson, and R. Jacobsen. Processing and characterization of aligned vapor grown carbon fiber reinforced polypropylene. *Composites: Park A*, 33(1):53–62, 2002.

[76] R. S. Ruoff and D. C. Lorents. Mechanical and thermal properties of carbon nanotubes. *Carbon*, 33(7):925–930, 1995.

[77] E. T. Thostenson and T.-W. Chou. Aligned multi-walled carbon nanotube-reinforced composites: processing and mechanical characterization. *Journal of Physics D: Applied Physics*, 35(16):77–80, 2002.

[78] F. Du, J. E. Fischer, and K. I. Winey. Coagulation method for preparing single-walled carbon nanotube/poly(methyl methacrylate) composites and their modulus, electrical conductivity, and thermal stability. *Journal of Polymer Science: Part B*, 41(24):3333–3338, 2003.

[79] V. K. Rangari, M. Yousuf, S. Jeelani, M. X. Pulikkanthara, and V. N. Khabashesku. Alignment of carbon nanotubes and reinforcing effects in nylon-6 polymer composite fibers. *Nanotechnology*, 19(145703):1–9, 2008.

[80] L. Jin, C. Bower, and O. Zhou. Alignment of carbon nanotubes in a polymer matrix by mechanical stretching. *Applied Physics Letters*, 73: 1197, 1998.

[81] R. Haggenmueller, H. H. Gommans, A. G¿ Rinzler, J. E. Fischer, and K. I. Winey. Aligned single-wall carbon nanotubes in composites by melt processing methods. *Chemical Physics Letters*, 330:219–225, 2000.

[82] T. Kimura, H. Ago, M. Tobita, S. Ohshima, M. Kyotani, and M. Yumura. Polymer composites of carbon nanotubes aligned by a magnetic field. *Advanced Materials*, 14(19):1380–1383, 2002.

[83] E. S. Choi, J. S. Brooks, D. L. Eaton, M. S. Al-Haik, M. Y. Hussaini, H. Garmestani, D. Li, and K. Dahmen4. Enhancement of thermal and electrical properties of carbon nanotube polymer composites by magnetic field processing. *Journal of Applied Physics*, 94(9):6034, 2003.

[84] T. Takahashi, K. Yonetake, K. Koyama, and T. Kikuchi. Polycarbonate crystallization by vapor-grown carbon fiber with and without magnetic field. *Macromolecular Rapid Communications*, 24(13):763–767, 2003.

[85] P. Potschke, A. Bhattacharyya, and A. Janke. Carbon nanotube-filled polycarbonate composites produced by melt mixing and their use in blends with polyethylene. *Carbon*, 45(5-6):965–969, 2004.

[86] M. Vincent and J. F. Agassant. Experimental and theoretical study of short-fibre orientation in diverging flows. *Rheological Acta*, 24(6):603–610, 1985.

[87] J. C. Halpin and J. L. Kardos. Strength of discontinuous reinforced composites 1. fiber reinforced composites. *Polymer Engineering and Science*, 18(6):496–504, 1978.

[88] A. C. Lederer. Characterization of physical properties of multi-scale polymer composites under various processing conditions. Master's thesis, University of Maryland, 2012.

[89] J. Nie, Y. Jia, P. Qu, and Q. Shi. Carbon nanotube/carbon fiber multi-scale composite: influence of interfacial strength on mechanical properties. *ournal of Inorganic and Organometallic Polymers and Materials*, 21:937–940, 2011.

[90] E. T. Thostenson, W. Z. Li, D. Z. Wang, Z. F. Ren, and T. W. Chou. Carbon nanotube/carbon fiber hybrid multi-scale composites. *Journal of Applied Physics*, 91(9):6034–6066, 2002.

[91] S.-B. Lee, O. Choi, W. Lee, J.W Yi, B.-S. Kim, J.-H. Byun, M.-K., H. Fong, E. T. Thostenson, and T.-W. Chou. Processing and characterization of multi-scale hybrid composites reinforced with nanoscale carbon reinforcements and carbon fibers. *Composites: Part A*, 42:337–344, 2011.

[92] H. Qian, A. Bismarck, E. S. Greenhalgh, G Kalinka, and M. S. P. Shaffer. Hierarchical composites reinforced with carbon nanotube grafted fibers: The potential assessed at the single fiber level. *Chemical Materials*, 20: 1862–1869, 2008.

[93] Y. Xu, D. D. L. Chung, and C. Mroz. Thermally conducting aluminum nitride polymer-matrix composites. *Composites: Part A*, 32:1749–1757, 2001.

[94] G.-W. Lee, M. Park, J. Kim, J. I. Lee, and H. G. Yoon. Enhanced thermal conductivity of polymer composites with hybrid fillers. *Composites: Part A*, 37:727.734, 2006.

[95] S. Zhang, S. Yin, C. Rong, P. Huo, Z. Jiang, and G. Wang. Synergistic effects of functionalized graphene and functionalized multi-walled carbon nanotubes on the electrical and mechanical properties of poly(ether sulfone) composites. *Macromolecular Nanotechnology*, 49:31253134, 2013.

[96] Z. Zheng, Z. Wang, Q. Feng, F. Zhang, Y. Du, and C. Wang. Preparation of surface-silvered graphene-cnts/polyimide hybrid films: Processing, morphology and properties. *Materials Chemistry and Physics*, 138: 350–357, 2013.

[97] W. Li, A. Dichiara, and J. Bai. Carbon nanotubegraphene nanoplatelet hybrids as high-performance multifunctional reinforcements in epoxy composites. *Composites Science and Technology*, 74:221–227, 2013.

[98] A. Arostegui and J. Nazabal. Compatibilization of a polybutylene terephthalate/polyethylene octene copolymer blends with different amounts of an epoxy resin. *Journal of Applied Polymer Science*, 91(1):260–269, 2004.

[99] *ASTM D638-10*. ASTM Internationals, 2010.

[100] M. Gupta and K. Wang. Fiber orientation and mechanical properties of short-fiber-reinforced injection-molded composites: simulated and experimental results. *Polymer Composites*, 14(5):367–382, 1993.

[101] M. L. Shofner, K. Lozano, F. J. Rodriguez-Macias, and E. V. Barrera. Nanofiber-reinforced polymers prepared by fused deposition modeling. *Journal of Applied Polymer Science*, 89(11):3081–3090, 2003.

[102] A. Bagsik and V. Schoppner. Mechanical properties of fused deposition modeling parts manufactured with ultem9085. In *Society of Plastic Engineers Annual Technical Conference 2011*, 2011.

[103] S. G. Advani and C. L. Tucker III. The use of tensors to describe and predict fiber orientation in short fiber composites. *Journal of Rheology*, 31(8):751–784, 1987.

[104] S. G. Advani and C. L. Tucker III. Closure approximations for three-dimensional structure tensors. *Journal of Rheology*, 34(4):367–386, 1990.

[105] H. L. Tekinalp, V. Kunc, G. M. Vlez-Garca, C. E. Duty, L. J. Love, A. K. Naskar, C. A. Blue, and S. Ozcan. Highly oriented carbon fiberpolymer composites via additive manufacturing. *Composites Science and Technology*, 105:144–150, 2014.

[106] C. Guthy, F. Du, S. Brand, K. Winey, and J. Fischer. Thermal conductivity of single-walled carbon nanotube/pmma nanocomposites. *Journal of Heat Transfer*, 129(8):10961099, 2007.

[107] S.-Y. Fu and B. lauke. Effects of fiber length and fiber orientation distributions on the tensile strength of short-fiber-reinforced polymers. *Composites Science and Technology*, 56:1179–1190, 1996.

[108] O. Valendtino, M. Sarno, N. G. Rainone, M. R. Nobile, P. Ciambelli, H. C. Neizert, and G. P. Simon. Influence on the polymer structure and

nanotube concentration on the conductivity and rheological properties of polyethylene/cnt composites. *Physica E*, 40:2440–2445, 2008.

[109] P. Potschke, T. D. Fornes, and D. R. Paul. Rheological behavior of multiwalled carbon nanotube/polycarbonate composites. *Polymer*, 43:3247–3255, 2002.

[110] A. A. Ahmad, A. A. Al-Juhani, S. Thomas, S. K. De, and M. A. Atieh. Effect of modified and unmodified carbon nanotubes on the rheological behavior of high density polyethylene nanocomposites. *Journal of Nanomaterials*, 2013:1–12, 2013.

[111] P. Potschke, M. Abdel-Goad, I. Alig, S. Dudkin, and D. Lellinger. Rheological and dielectrical characterization of melt mixed polycarbonate-multi-walled carbon nanotube composites. *Polymer*, 45:8863–8870, 2004.

[112] T. McNally, P. Potschke, P. Halley, M. Murphy, D. Martin, S. E. J. Bell, G. P. Brennan, D. Bein, P. Lemoine, and J. P. Quinn. Polyethylene multi-walled carbon nanotube composites. *Polymer*, 46:8222–7232, 2005.

[113] R. C. Progelhof, J. L. Throne, and R. R. Ruetsch. Methods for prediction the thermal conductivity of composite systems: a review. *Polymer Engineering and Science*, 16(9):615–625, 1976.

[114] I. H. Tavman and H. Akinci. Transverse thermal conductivity of fiber reinforced polymer composites. *International Communication of Heat and Mass Transfer*, 27(2):253–261, 2000.

[115] M.-X. Shen, Y.-X. Cui, J. He, and Y.-M. Zhang. Thermal conductivity model of filled polymer composites. *International Journal of Minerals, Metallurgy and Materials*, 18(5):623–631, 2011.

[116] M. Zimmer, X. Fan, J. Bao, B. Wang, C. Zhang, and J. Brooks. Through-thickness thermal conductivity prediction study on nanocomposites and

multiscale composites. *Materials Sciences and Applications*, 3:131–138, 2012.

[117] J. C. Halpin and J. L. Kardos. The halpin-tsai equations: a review. *Polymer Engineering and Science*, 16(5):344–352, 1976.

[118] L. Nielsen. Thermal conductivity of particulate-filled polymers. *Journal of Applied Polymer Science*, 17:3819–3820, 1973.

[119] T. Lewis and L. Nielsen. Dynamic mechanical properties of particulate-filled polymers. *Journal of Applied Polymer Science*, 14:1449, 1970.

[120] L. Nielsen. The thermal and electrical conductivity of two-phase systems. *Industrial Engineering and Chemistry Fundamentals*, 13:17–20, 1974.

[121] S. Wang and J. Qui. Enhancing thermal conductivity of glass fiber/polymer composites through carbon nanotubes incorporation. *Composite: Part B*, 41:533–536, 2010.

[122] S. C. Cheng and R. I. Vachon. The prediction of the thermal conductivity of two and three phase solid heterogeneous mixtures. *International Journal of Heat and Mass Transfer*, 12:249–264, 1969.

[123] Y. Agari and T. Uno. Estimation of thermal conductivities of filled polymers. *Journal of Applied Polymer Science*, 32:5705–5712, 1986.